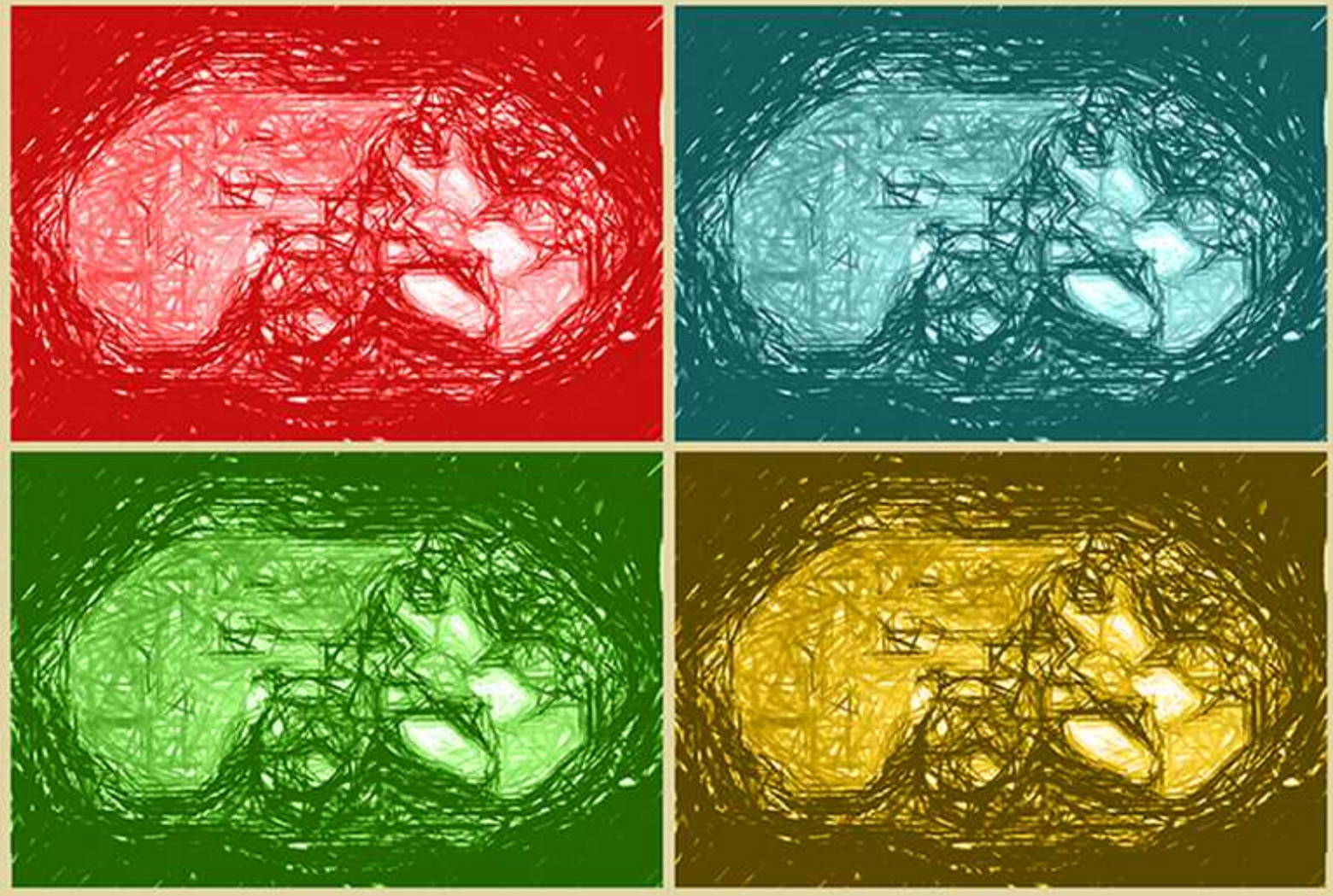

Helena Cristina Gil Cardeira dos Santos Leitão

NOVEL NONINVASIVE IMAGING BIOMARKERS FOR LIVER STEATOSIS, INFLAMMATION AND FIBROSIS

Março 2013

· U C ·

Universidade de Coimbra

Universidade de Coimbra

Faculdade de Ciências e Tecnologia

Departamento de Ciências da Vida

Novel Noninvasive Imaging Biomarkers for Liver Steatosis, Inflammation and Fibrosis

Dissertation presented to obtain a Ph.D. degree in Biosciences, Specialization in Biotechnology, at the Faculty of Sciences and Technology of the University of Coimbra

Helena S. Leitão

2013

Supervised by: Carlos F.G.C. Geraldes, Ph.D. and Filipe Caseiro Alves, M.D., Ph.D.

Professor Bernard Van Beers M.D., Ph.D. co-supervised Dr. Helena S. Leitão's work, and is a co-supervisor acknowledged by the Portuguese Foundation for Science and Technology and the Doctoral Programme in Experimental Biology and Biomedicine.

This work was performed at:

Universitary Clinic of Radiology, Coimbra University Hospitals – Coimbra, Portugal (Head of Department: Professor Filipe Caseiro Alves);

Athinoula A. Martinos Center – Boston, United States of America (Head of Laboratory Division: Professor Peter Caravan);

INSERM Unit 773 – Clichy, France (Head of Laboratory Division: Professor Bernard Van Beers)

Department of Radiology, Beaujon Hospital – Clichy, France (Head of Department: Professor Valérie Vilgrain).

Helena S. Leitão received a Ph.D. fellowship (SFRH / BD / 33893 / 2009) from the Portuguese Foundation for Science and Technology.

The Universitary Clinic of Radiology, Athinoula A. Martinos Center and INSERM Unit 773 financed the presented research.

Cover design: Helena S. Leitão and Vítor Almeida de Almeida

Governo da República Portuguesa
Projeto PEst-C/SAU/LA0001/2013-2014

To Luís, Manuel, João, …..

The difference between the impossible and the possible is merely a measure of a man's determination.

Captain James Thain

And to all the patients affected by
Chronic Liver Disease

Success is not final, failure is not fatal: it is the courage to continue that counts.

Winston Churchill

Acknowledgements

I thank the jury at the Center for Neuroscience and Cell Biology of Coimbra for accepting me in the Doctoral Programme.

I wish to thank the Portuguese Foundation for Science and Technology for my fellowship.

I owe my sincere gratitude to my supervisor Professor Carlos Geraldes. You have given me a starting point. I will never forget how you so kindly accepted to receive me for the first time at 10 pm, after a phone call, without even knowing me.

I am extremely grateful to my co-supervisor Professor Caseiro Alves. Your knowledge and experience were enlightening and always gave me the strength to continue. Thank you for all the scientific discussions. No words can express my gratitude for “opening the door and letting me spread my wings”.

I was very fortunate and I had the privilege of working directly with Professors Bernard Van Beers and Valérie Vilgrain. Thank you for believing in me and for the opportunities you gave me. Your door was always open for my questions or problems. You are my role models! To my co-supervisor Professor Bernard Van Beers I am forever grateful…!

I would like to thank Dr. Cristina Marques for all the patience, belief and Friendship. I learn so much with you….

I thank the almost Professor Alexandra Borges for being my “partner in crime” in the Ph.D. life.

I wish to thank Dr. Cláudia Paulino for helping me with the work in Coimbra.

I thank Professor Margarida Castro for our diversified discussions. I consider you a Friend.

I also thank Dr. Augusta Cipriano and Dr. Luísa Teixeira for their support and Friendship.

I also would like to aknowledge Emílio Leal, Alda Pinto, Paulo Carvalho e Paula Marques, for performing the MRI and MRS examinations at the Universitary Clinic of Radiology. We did it!

Thank you to Isabel Saldanha for your Friendship and amazing bibliography sources.

I thank Marta Klose from Siemens, for helping with the implementation of the MRS sequence.

I wish to thank my co-workers and friends at the imaging research in France. Ralph Sinkus, Gaspard d’Assignies, Sabrina Doblas, Mathilde Wagner, Philippe Garteiser, Simon Lambert, Sara di Renzo, Feryel Mouri, Matthieu Lagadec (o francês mais brasileiro de França), Lauriane Juge (Australian open and baby shower in january

2014?) and Jean-Luc Daire.

I also want to thank all the people I worked with at the Department of Radiology of Beaujon Hospital. I won't say any names as I might forget someone…you were so many and I was so well taken care of….Thank you!

Thank you to Professors Valérie Paradis and Pierre Bedossa for reviewing liver slices and answering all my questions.

I also wish to thank Nathalie Colnot for helping me with morfometry readings.

I thank Professors Peter Caravan and Alex Guimaraes for my "US experience". All things considered we still did a very good work….

Thanks to Ana Carolina Santos, Ronald Borra, Kate Ciesienski, Milos Polasek, John Stanko, Daniel Schuehle and Marytheresa Ifediba for making my life in the US so enjoyable. When is the next chicken wings' session?

Above all I wish to thank my husband and sons for their understanding and belief in me. Now that I am finally home I won't miss the timeless hours we shared on computers and telephones. I will never leave you again and that is a promise!

This thesis is based on the following original publications, which are referred to as chapters in roman numerals IV-VI. Additional unpublished data is also presented in chapter VII.

Chapter IV:

Helena S. Leitão, Cláudia Paulino, Dírcea Rodrigues, Sónia I. Gonçalves, Cristina Marques, Manuela Carvalheiro, Carlos F.G.C. Geraldes, Filipe Caseiro-Alves: MR fat fraction mapping: a simple biomarker for liver steatosis quantification in nonalcoholic fatty liver disease patients. Accepted in Academic Radiology in May 2013. DOI: 10.1016/j.acra.2013.05.004

Chapter V:

Helena S Leitão, Sabrina Doblas, Gaspard d'Assignies, Philippe Garteiser, Jean-Luc Daire, Valérie Paradis, Carlos FGC Geraldes, Valérie Vilgrain, Bernard E Van Beers: Fat deposition decreases diffusion parameters at MRI: a study in phantoms and patients with liver steatosis. Eur Radiol 2013;23:461-467.

Chapter VI:

Helena S Leitão, Gaspard d'Assignies, Sabrina Doblas, Philippe Garteiser, Feryel Mouri, Jean-Luc Daire, Valérie Paradis, Carlos FGC Geraldes, Valérie Vilgrain, Bernard E Van Beers. The influence of liver fibrosis, inflammation and steatosis on MR diffusion and viscoelastic parameters: a prospective study in patients with chronic liver disease**.** Manuscript submitted to Hepatology.

Other original publications to which I contributed but that were not directly related to my personal work can also be consulted in Original Publications.

Philippe Garteiser, Sabrina Doblas, Jean-Luc Daire, Mathilde Wagner, **Helena S Leitão**, Valérie Vilgrain, Sinkus R, Bernard E Van Beers: MR elastography of liver tumors: increased viscosity suggests malignancy. Eur Radiol 2012;22(10):2169-2177.

Mathilde Wagner, Sabrina Doblas, Jean-Luc Daire, Nathalie Haddad**, Helena S Leitão**, Philippe Garteiser, Valérie Vilgrain, Ralph Sinkus, Bernard E Van Beers: Diffusion-weighted MR imaging for the regional characterization of liver tumors. Radiology 2012;264(2):464-472.

Sabrina Doblas, Mathilde Wagner, **Helena S Leitão**, Jean-Luc Daire, Ralph Sinkus, Valérie Vilgrain, Bernard E Van Beers: Determination of malignancy and characterization of hepatic tumor type with diffusion-weighted MR imaging: comparison of apparent diffusion coefficient and IVIM-derived measurements. Accepted in Investigative Radiology in 2013. DOI: 10.1097/RLI.0b013e3182915912.

Sabrina Doblas, Mathilde Wagner, **Helena S Leitão**, Jean-Luc Daire, Ralph Sinkus, Valérie Vilgrain, Bernard E Van Beers: Reproducibility of intravoxel incoherent motion diffusion-weighted imaging parameters. Manuscript submitted to Radiology.

Table of Contents

Abbreviations

α, Attenuation coefficient

ADC, Apparent diffusion coefficient

ALT, Alanine transaminase

ARFI, Accoustic radiation force impulse

AUROC, Area under receiver operating characteristic

β, Propagation coefficient

$B_{0,}$ Magnetic field

BMI, Body mass index

CNR, Clinical research network

CNR, Contrast-to-noise ratio

CT, Computed tomography

D, True diffusion coefficient

D*, Perfusion-related diffusion coefficient

DEN, Diethylnitrosamine

DWI, Diffusion-weighted imaging

E, Young´s modulus

EPI, Echo-planar imaging

ESR, European Society of Radiology

f, Perfusion fraction

FDA, Food and Drug Administration

FF, Fat fraction

FFM, Fat fraction mapping

FID, Free induction decay

FOV, Field of view

Υ, Wave frequency

γ_H, Gyromagnetic ratio

Υ_λ, Wavelength exponent

G*, Complex shear modulus

G´, Storage modulus

G´´, Loss modulus

Gd, Gadolinium

Gd-DOTA, Gadolinium 1,4,7,10-tetraazacyclododecane-1,4,7,10-tetraacetic acid

Gd-EOB-DTPA, Gadolinium ethoxybenzyl diethylenetriamine pentaacetic acid

GRE, Gradient echo

HCC, Hepatocellular carcinoma

HU, Hounsfield units

IP, In-phase

IQR, Interquartile range

IVC, Inferior vena cava

IVIM, Intravoxel incoherent motion

k, Wave number

kPa, kiloPascal

λ, Wavelength

MHz, Megahertz

MRE, Magnetic resonance elastography

MRI, Magnetic resonance imaging

MRP, Multidrug resistance protein

MRS, Magnetic resonance spectroscopy

NAFL, Nonalcoholic fatty liver

NAFLD, Nonalcoholic fatty liver disease

NAS, NAFLD activity score

NASH, Nonalcoholic steatohepatitis

NIH, National Institutes of Health

NMV, Net magnetization vector

ω, Circular frequency

ω_0, Larmor frequency

OATP, Organic anion transport polypeptide

OP, Opposed-phase

PBS, Phosphate buffered saline

PD, Proton density

PPM, Parts-per-million

PRESS, Point-resolved spectroscopy

ρ, Density

r, Spearman correlation coefficient

RC, Multivariate regression correlations

RF, Radiofrequency

ROI, Region of interest

σ, Poisson´s ratio

SE, Spin echo

SNR, Signal-to-noise ratio

STEAM, Stimulated-echo acquisition mode

SWE, Shearwave elastography

T1, Longitudinal relaxation time

T2, Transverse relaxation time

T, Tesla

TE, Echo time

TE, Transient elastography

TR, Repetition time

Sumário

As hepatites virais e a doença hepática gorda não alcoólica são actualmente as causas mais frequentes de doença hepática crónica. Qualquer uma destas patologias é caracterizada pela presença no parênquima hepático de esteatose, inflamação e fibrose, que podem agravar-se e levar a uma situação clínica de insuficiência hepática, causando não só considerável morbilidade mas também mortalidade, e igualmente um real incremento nos custos nacionais com a saúde. A capacidade de deteção precoce, por rotina, de estádios ligeiros/moderados de inflamação e fibrose e a quantificação da esteatose através de meios de imagem não invasivos, poderá trazer vantagens clínicas importantes para estes doentes e para a sociedade.

No presente estudo aqui desenvolvido, a fibrose, inflamação e a esteatose hepáticas foram avaliadas de forma não invasiva por ressonância magnética, com sequências de eco de gradiente e sequências ponderadas em difusão, elastografia por ressonância magnética e imagem molecular em ressonância magnética. Foi igualmente utilizada a ecografia com elastografia supersónica por onda de cisalhamento. Do conjunto de estudos aqui apresentados foi possível observar:

- A esteatose hepática pode ser quantificada de forma precisa e simples, utilizando um mapeamento total da gordura hepática por ressonância magnética. Assim, será possível diagnosticar precocemente os doentes com fígado gordo não alcoólico;
- Os parâmetros viscoelásticos são mais precisos que os parâmetros de difusão no estadiamento da fibrose hepática. Determinar precocemente quais os doentes com estádios de fibrose F2 é fundamental para o início da terapêutica antiviral;
- Os parâmetros viscoelásticos independentes da frequência de excitação são

potenciais biomarcadores de inflamação hepática. Até hoje ainda não existia nenhum biomarcador por imagem focado apenas para a inflamação hepática, mas a deteção precisa desta evitaria, por exemplo, que os doentes com fígado gordo não alcoólico progredissem para um quadro de esteatohepatite não alcoólica e uma melhor avaliação do parênquima hepático nos doentes com hepatites virais;

- A ecografia com elastografia supersónica por onda de cisalhamento é proposta como uma técnica adequada para o rastreio de doentes com fibrose hepática;
- Finalmente, uma abordagem experimental em imagem molecular utilizando um contraste de ressonância magnética vectorizado especificamente para a fibrina, permitiu a deteção de fibrose no prênquima hepático em ratos injectados com dietilnitrosamina.

Summary

Viral hepatitis and nonalcoholic fatty liver disease are nowadays the most common causes of chronic liver disease. These disorders, which are characterized by parenchymal steatosis, inflammation and fibrosis can progress to liver failure and are a substantial source of morbidity, mortality and increased healthcare costs. The early detection of fibrosis and inflammation and the routinely quantification of steatosis by noninvasive methods have important clinical implications in these patients.

In the current study liver fibrosis, inflammation and steatosis, were noninvasively assessed by magnetic resonance gradient echo imaging, intravoxel incoherent motion diffusion-weighted imaging, magnetic resonance elastography, ultrasound-based shear wave elastography and molecular imaging. Liver fat content was accurately quantified by a simple and fast mapping technique using magnetic resonance imaging, which can allow the early detection of patients with nonalcoholic fatty liver. In addition, magnetic resonance viscoelastic parameters were found to be more accurate than diffusion parameters to stage patients with liver fibrosis. Determining when a patient reaches an F2 fibrosis stage is crucial to start antiviral treatment. Moreover, a frequency-independent viscoelastic parameter is proposed as a potential biomarker for liver inflammation. The early detection of increased liver inflammation can prevent patients with nonalcoholic fatty liver from progressing to nonalcoholic steatohepatitis and enables an adequate follow up of patients with viral hepatitis. Furthermore, the ultrasound-based shearwave elastography is proposed for the routine clinical screening of patients with liver fibrosis. Finally, in an experimental rat study, a novel vectorized fibrin-binding magnetic resonance contrast agent was found to accurately detect liver fibrosis.

Palavras-Chave: Imagem por Ressonância Magnética, Imagem Ponderada em Difusão, Elastografia por Ressonância Magnética, Elastografia Supersónica por Onda de Cisalhamento, Fígado, Hepatites Virais, Doença Hepática Gorda Não Alcoólica, Quantificação de Gordura Hepática, Imagem Molecular.

Key words: Magnetic Resonance Imaging, Diffusion-Weighted Imaging, Magnetic Resonance Elastography, Supersonic ShearWave Elastography, Liver, Viral Hepatitis, Nonalcoholic Fatty Liver Disease, Liver Fat Quantification, Molecular Imaging.

Chapter I

Introduction

1.1. Introduction

Chronic liver diseases, such as viral hepatitis and nonalcoholic fatty liver disease (NAFLD) are a major cause of morbidity and mortality worldwide and their prevalence has been rising in the last two decades (1, 2). Although NAFLD was mostly unrecognized before the 1980's, the rising epidemics of obesity and type 2 diabetes have brought awareness to this disease, which is currently considered the most common cause of chronic liver disease in the adult and paediatric population (1, 3). NAFLD includes a spectrum of liver damage ranging from bland steatosis to steatohepatitis, cirrhosis and ultimately liver failure and hepatocellular carcinoma (3).

Liver biopsy, with histopathological scoring of the obtained specimen, is until now the reference standard to evaluate fibrosis, inflammation and steatosis (3). However, it's an invasive technique and it's also prone to sampling errors in diffuse and heterogeneous liver diseases such as viral hepatitis and NAFLD (4). Moreover, from a patient's perspective the prospect of undergoing repeated liver biopsies for follow-up is intimidating and highly inconvenient.

Noninvasive biomarkers are currently under demand and are of the utmost importance to assess liver fibrosis, inflammation and steatosis. Several noninvasive serum biomarkers, such as the FibroMax panel (FibroTest + SteatoTest + NASHTest), the plasma Pentraxin-3 and Cytokeratin-18 are being studied, but their accuracy and clinical usefulness is yet to be determined and their utility in the follow-up is unknown (3). Diagnostic Radiology is a dynamic specialty that continues to undergo rapid changes with ongoing advancements in technology and has revolutionized several fields of medicine. Currently, imaging is as important, albeit complementary, as a detailed physical exam and anamnesis. The prospect of using noninvasive and radiation-free methods, like magnetic resonance imaging and

ultrasound, in the screening and follow-up of patients with liver fibrosis, inflammation and/or steatosis is particularly attractive. Thus, the purpose of this project was to determine which imaging biomarkers could be used in the noninvasive assessment and follow-up of fibrosis, inflammation and steatosis in patients with chronic liver diseases.

Chapter II

Review of the Literature and State of the Art

2.1. The Liver

2.1.1. History

The art of hepatoscopy started at Mesopotamia, approximately at the year 2000 BC, when the inspection of the liver was the most important method of foretelling events. The sacrificial priests acquired precise knowledge of the animal liver, especially that of the sheep, and assigned specific names to the different parts of the liver and gallbladder or their respective variations (5). The reading of the liver received an enormous acceptance from the Greeks and Etruscans. Several Etruscan liver models have survived until our days in which the gallbladder, the pyramidal and papillary processes and the left and right lobes (pars hostilis and pars familiaris, respectively) are well differentiated (Fig.1) (5).

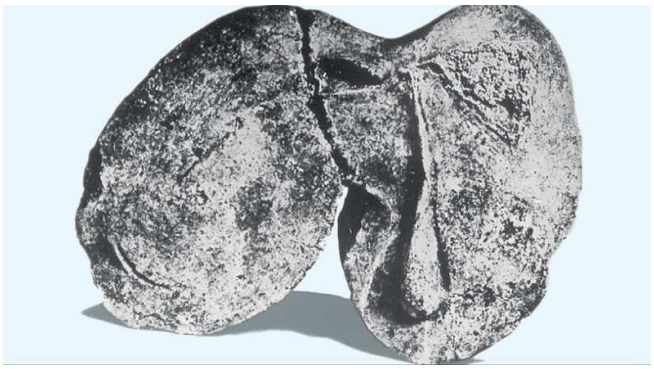

Figure 1. Etruscan clay model of a liver (200 BC). Reproduced from [5].

The Etruscan fortunetellers were particularly notorious in the Roman Empire and prophecies were related to specific features in the sacrificial liver or gallbladder (Fig. 2) (5, 6). For example, predictions pertaining to the inquirer were mostly derived from the appearance of the pars familiaris and gallbladder and those of the rival from the pars hostilis. Moreover, numerous predictions were of historical interest such as the presence of

an enlarged and double gallbladder that foresaw the victory of Octavian against the forces of Marcus Antonius and Cleopatra in the battle of Actium (31 BC) (5, 6). At the time of the fall of the Roman Empire, hepatoscopy was already well established in the human belief and it was used to influence major personal and political decisions.

Figure 2. Etruscan hand mirror in bronze, 500–400 BC. KALCHAS, the most famous of the sacrificial priests, inspects the animal liver a with large caudate process. Reproduced from [5].

In the 5th and 6th centuries BC, the profound effect of mythology was replaced by rational research of anatomy and physiology. Aristoteles of Stagira was the first to distinguish between hepatic arteries and veins and to describe the portal vein within the venous system (5). Four hundred years later Galenos of Pergamon described the anatomy of the liver in greater detail than before, as he explained the ramifications of the intrahepatic vessels and sinusoids. It was only in 1654 that Francis Glisson published the first monography on the liver and discussed intrahepatic vessels and the surrounding connective tissue (Fig. 3) (5, 7). Even today we refer to the Glisson's capsule that surrounds the liver and to the portal triad as Glisson's triangle.

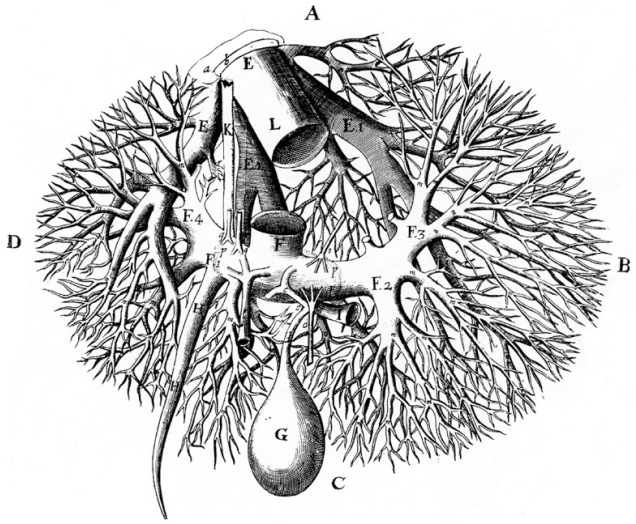

Figure 3. Illustration of the blood and bile vessels of the liver by F. GLISSON, 1654 (A: dorsal region, B: right aspect, C: ventral region, D: left aspect, E: hepatic veins, H: umbilical vein, K: duct of ARANTIUS, G: gall bladder, I: bile duct, F: portal vein). Reproduced from [5].

Johan Jacob Wepfer first described the term lobule, in the liver parenchyma, in 1664, but it was with Marie François Xavier Bichat, the father of modern Histology, at the beginning of the 19th century that the hepatic parenchyma was considered to be a special tissue in terms of function and morphology (5). The French Physiologist Henri Dutrochet described hepatocytes twenty years later. In the following years, the development of the research methods brought greater insight into liver metabolism and physiology with such names as Claude Bernard and Friedrich Theodor Frerichs, the fathers of modern Liver Physiology and Pathology, respectively (5).

2.1.2. General Liver Anatomy

The liver is the largest solid organ in the human body and its volume ranges from 1,500-1,600 cm^3 in men and 1,400-1,500 cm^3 in women (5). Its surface is smooth with a red

brownish color and the liver is located intraperitoneally, with the exception of its bare area. The separation between right and left liver is not macroscopically visible, however, the left (smaller) and right (larger) lobes can be easily discriminated at the level of the falciform ligament (Fig. 4). This double layer of peritoneum binds the liver to the anterior abdominal wall, and on its free edge we can find the round ligament, which is a remnant of the umbilical vein that carries the oxygenated blood to the foetus (8, 9).

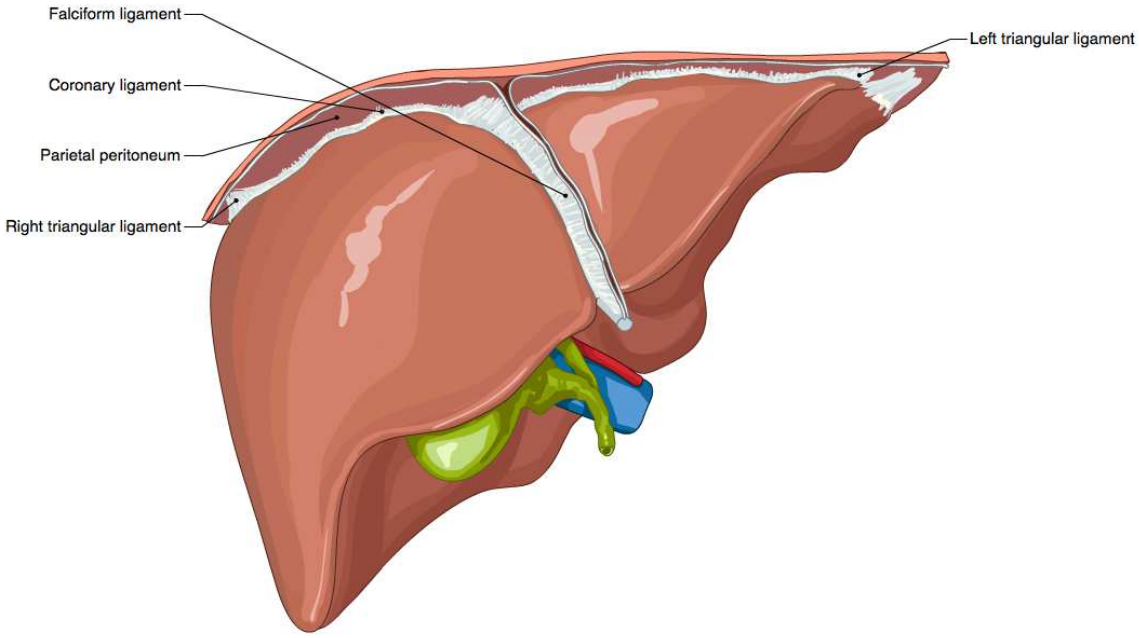

Figure 4. Normal liver. The falciform ligament separates the left and right lobes. Reproduced from IMAIOS.

The liver has a dual blood supply from the portal vein and common hepatic artery. The portal vein is responsible for approximately 70 % and the hepatic artery for 30 % of the blood flow (9, 10). In the liver parenchyma, a fibrous sheath (Glisson's capsule) surrounds arteries, portal veins, and bile ducts. However, hepatic veins lack such protection.

The common hepatic artery takes origin most often from the celiac trunk (86 %); other sources are the superior mesenteric artery, aorta or left gastric artery. The common hepatic

artery then runs horizontally along the upper border of the head of the pancreas (9). When the gastroduodenal artery branches off the common hepatic artery, it continues as the proper hepatic artery and turns upward to ascend in the lesser omentum, enveloped by the hepatoduodenal ligament (9, 11). Within this ligament, the proper hepatic artery that lies to the left of the common bile duct and anterior to the portal vein, divides into right and left branches (Fig. 5) (10).

The portal vein is formed by the confluence of the superior mesenteric vein and the splenic vein behind the neck of the pancreas (9, 10). At the liver hilum, the portal vein bifurcates into right and left branches before entering the liver. The right branch is short and rapidly divides into anterior and posterior branches for the anterior and posterior right sectors. In general, portal veins are found posterior to the hepatic arteries in their lobar and segmental distribution (10).

Three major veins that open into the Inferior Vena Cava (IVC) drain the liver (Fig. 5). The right, median and left hepatic veins are found intrahepatically within planes separating lobes and sectors (8 - 10).

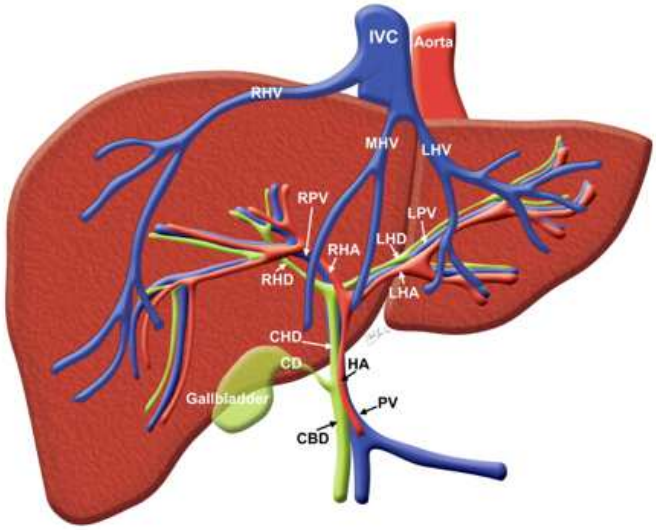

Figure 5. Normal anatomy of the liver. *CBD:* common bile duct, *CD:* cystic duct, *CHD:* common hepatic duct, *HA:* hepatic artery, *IVC:* inferior vena cava, *LHA:* left branch hepatic artery, *LHD:* left hepatic duct, *LHV:* left hepatic vein, *LPV:* left portal vein, *MHV:* middle hepatic vein, *PV*: portal vein, *RHA:* right branch hepatic artery, *RHD:* right hepatic duct, *RHV:* right hepatic vein, *RPV:* right portal vein. Adapted and reproduced from [9].

Bile canaliculi are formed by parts of the membrane of adjacent parenchymal cells, and they are isolated from the perisinusoidal space by junctions. Bile flows from the canaliculi through ductules (canals of Hering) into the interlobular bile ducts found in portal triads. Biliary segmentation is identical to portal vein segmentation (8 - 10).

The hepatic lymphatic network, superficial and deep, does not follow the functional vasculobiliary organization (Fig. 6). The superficial lymphatic system, located within the Glisson's capsule, travels toward the thorax and the abdominal regional lymph nodes. Lymph vessels pass the diaphragm mainly in the bare area or through Morgagni's foramen to reach anterior or lateral phrenic nodes. The deep system is the system of greater lymphatic outflow. It drains toward the lateral phrenic nerve nodes through the caval hiatus following hepatic veins or to nodes of the liver hilum following portal vein branches (12).

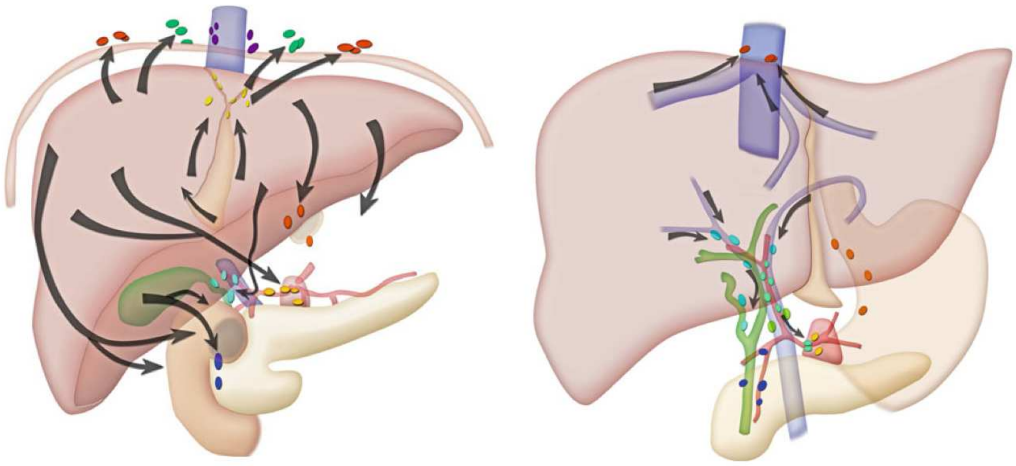

Figure 6. Left: Superficial pathways of lymphatic drainage for the liver. The anterior diaphragmatic nodes consist of the lateral anterior diaphragmatic group and the medial group, which includes the pericardiac nodes and the subxiphoid nodes behind the xiphoid cartilage. The nodes in the falciform ligament drain into the anterior abdominal wall along the superficial epigastric and deep epigastric lymph nodes. The epigastric and the subxiphoid nodes drain into the internal mammary nodes. **Right: Deep pathways of lymphatic drainage for the liver.** The deep pathways follow the hepatic veins to the inferior vena cava nodes and the juxtaphrenic nodes that follow along the phrenic nerve. The pathways that follow the portal vein drain into the hepatic hilar nodes and the nodes in the hepatoduodenal ligament, which then drain into the celiac node and the cisterna chili. Reproduced from [12].

2.1.3. Segmentation of the Liver

Functional anatomy refers to the description of hepatic segmentation, which is the genuine anatomical basis for modern hepatic surgery. Liver resection still remains the only potential curative treatment for primary and metastatic liver tumors, and it is also indicated in some benign liver conditions, such as symptomatic hemangiomas or adenomas. It was the constantly enhanced knowledge of hepatic anatomy that enabled improvements in the techniques of liver resection. The resection of the liver started at the beginning of the 18th century when, in 1716, Berta performed the first partial liver excision. However, the unstoppable bleeding and high mortality rates, made surgeons dread to operate on this organ, and the first successful liver resection was only performed at the end of the 19th century (7). The segmental and vascular anatomy that defines the surgical approach to lesion resection is the most important anatomy to liver imaging. Couinaud, developed a

numbering system in 1957 and was an innovator in this field, by showing two major advances (8, 13). First, liver can be subdivided in hemilivers, sectors and segments using venous landmarks: portal branches and hepatic veins. Second, each segment has its own hepatic artery, portal vein and biliary drainage and therefore can be removed or safely preserved. The eight Couinaud segments have separate vascular inflow, outflow, and biliary drainage and therefore can be resected without damaging the remaining segments. It was the work of Goldsmith and Woodburn (1957), Couinaud (1957) and Bismuth (1982) that led to the nomenclature used today (Table 1) (7, 14). From a practical and axial imaging perspective, division of the liver into segments is based on a very important concept of three longitudinal planes and two transverse planes (Fig. 7) (13). A longitudinal plane through the middle hepatic vein, IVC, and gallbladder fossa divides the liver into right and left hemilivers (Fig. 8). A longitudinal plane through the right hepatic vein divides the right liver into anterior (VIII and V) and posterior (VII and VI) sectors. A longitudinal plane through the left hepatic vein divides the left liver into medial (IVa and IVb) and lateral (II and III) sectors. The branches of the portal vein divide the liver into segments. A transverse plane through the left portal vein divides the left liver into superior (IVa and II) and inferior (IVb and III) segments. An oblique transverse plane through the right portal vein divides the right liver into superior (VIII and VII) and inferior (V and VI) segments (14, 15). Segment I is called the caudate (Spiegel's) lobe and extends between the fissure of the ligamentum venosum and the IVC. In its inferior surface we can find the pyramidal (right) and papillary (left) processes. The hepatic venous drainage from the caudate lobe goes directly into the IVC via small veins. The ligamentum venosum or Arantius ligamentum that limits the caudate lobe is secondary to the obliteration of the ductus venosus that, during foetal development, connected the umbilical portion of the portal vein to the inferior vena cava, shunting away from the liver the oxygenated

umbilical cord blood. The right lobe includes all the segments in the right liver (VIII, VII, VI, V) and the segment IV. The left lobe corresponds to the left liver minus the segment IV, which means: segments II and III (Fig. 9) (7, 14, 15).

Table 1. Anatomic segments of the liver

Anatomic Subsegment	Nomenclature		
	Couinaud	Bismuth	Goldsmith and Woodburne
Caudate lobe	I	I	Caudate lobe
Left lateral superior subsegment	II	II	Left lateral segment
Left lateral inferior subsegment	III	III	
Left medial subsegment	IV	IV_a, IV_b	Left medial segment
Right anterior inferior subsegment	V	V	Right anterior segment
Right anterior superior subsegment	VIII	VIII	
Right posterior inferior subsegment	VI	VI	Right posterior segment
Right posterior superior subsegment	VII	VII	

Reproduced and adapted from [14].

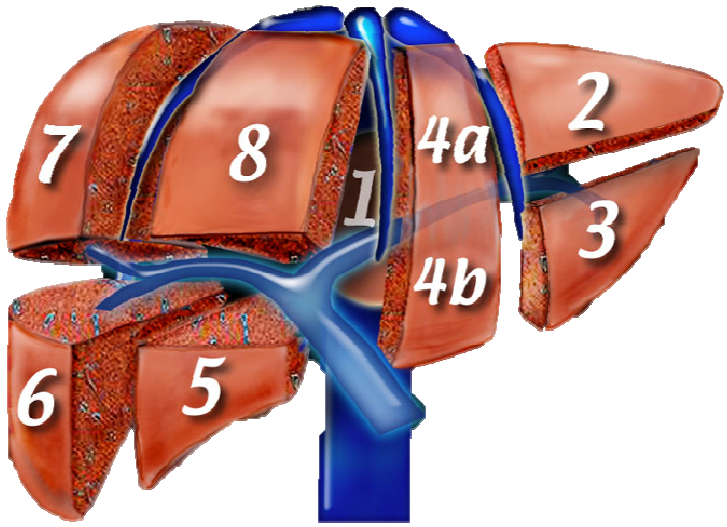

Figure 7. Liver segmentation based on the venous plans. Segment 1 is located posteriorly. Reproduced from www.radiologyassistant.nl.

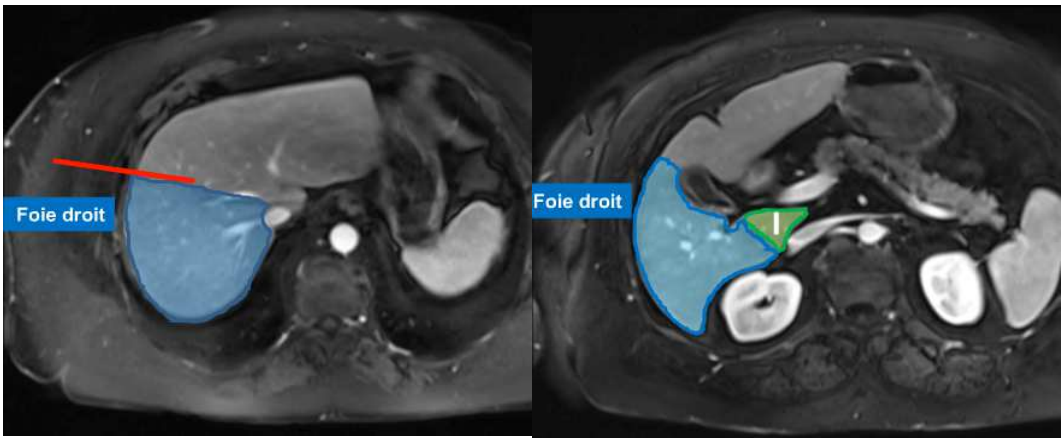

Figure 8. Longitudinal plane separating through the medial hepatic vein and gallbladder separating the right and left hemilivers Left: above portal vein bifurcation. Right: below portal vein bifurcation. I, caudate segment. Reproduced from www.sfrnet.org "Anatomie du foie et protocoles d'exploration: trucs et astuces pour la pratique".

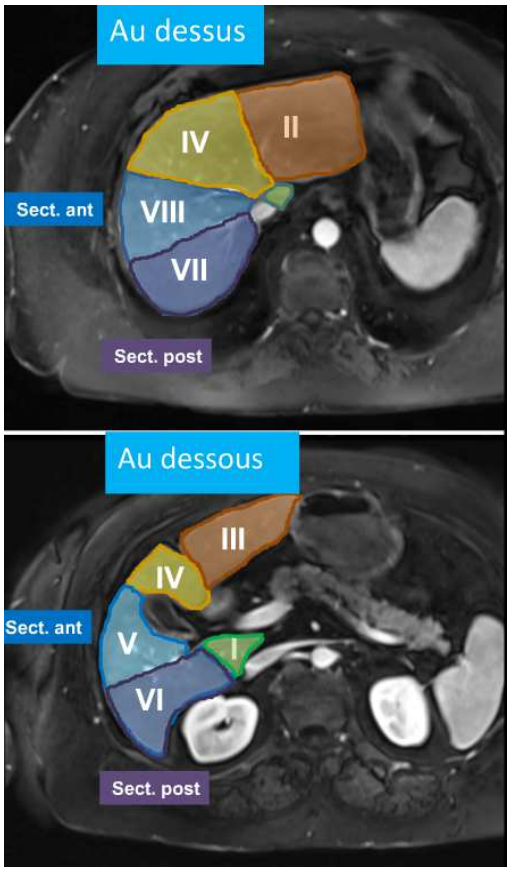

Figure 9. Liver Segments. Reproduced from www.sfrnet.org "Anatomie du foie et protocoles d'exploration: trucs et astuces pour la pratique".

2.1.4. Hepatic Lobules

The liver parenchyma is divided into lobules. The classic lobule resembles a hexagon and is centered on a central vein with portal triads (which contain a branch of the portal vein, hepatic artery and bile duct) at each corner (Fig. 10) (16). The lobular structure also contains liver cells, called hepatocytes, arranged in plates around the central vein. The space between those plates of hepatocytes is filled with sinusoids (low pressure vascular channels lined with endothelial cells) that receive blood from terminal branches of the hepatic artery and portal vein at the periphery of the lobule and deliver it into central veins (Figs. 10, 11) (5, 16). Functionally, the lobule can be divided into three zones based on the oxygen supply. Zone 1 encircles the portal triads, which are well oxygenated by the hepatic arteries, while zone 3 is located around the central veins where oxygenation is poor. Zone 2 is located in between (Figs. 12, 13) (17).

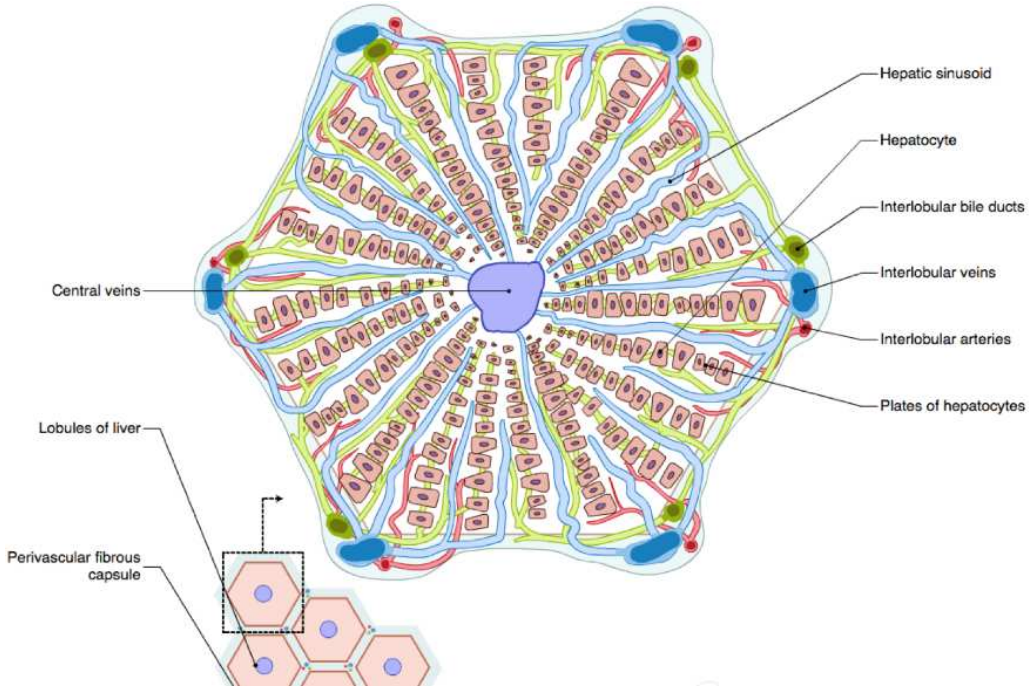

Figure 10. The classic hepatic lobule. Reproduced from IMAIOS

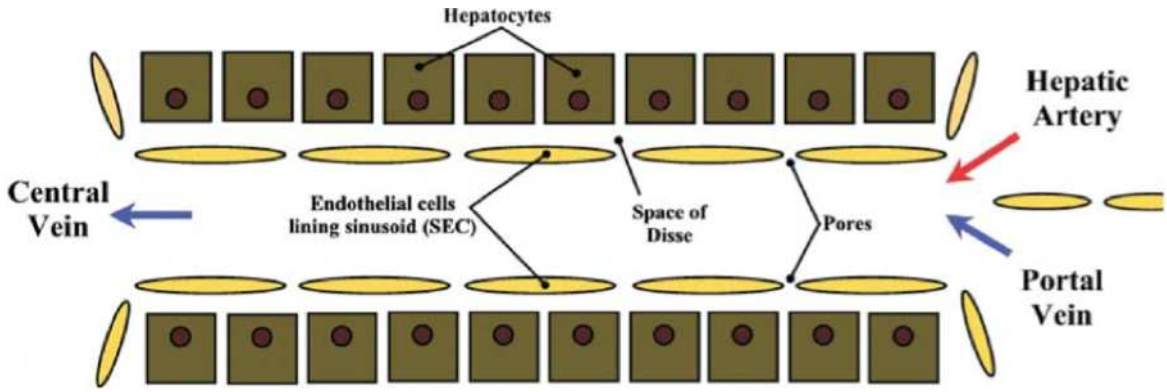

Figure 11. Enhancement of Figure 10 at the level of two plates of hepatocytes. Reproduced from [17].

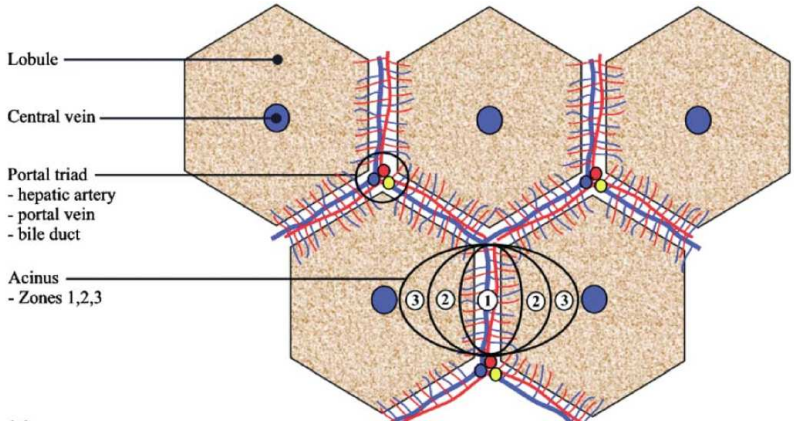

Figure 12. The hepatic lobule and acinus. The acinus is the physiological unit of the liver and is divided into three zones, according to distance from the afferent arterial supply. Reproduced from [17].

Between the sinusoidal endothelium and hepatocytes we can find the space of Disse. Sinusoidal endothelial cells are highly fenestrated, which allows unimpeded flow of plasma from sinusoidal blood into the space of Disse (5, 16). Therefore, hepatocytes are bathed in nutrient-rich plasma (derived from the small intestine), but this plasma will also flow back toward the portal triads, collecting into lymphatic vessels and forming a large fraction of the body's lymph. In fact, lymphatic vessels are also found in the portal triads but since their walls are delicate and often collapsed, they are less easily identified (5, 16). Another significant feature of hepatic sinusoids is that they house an important part of the phagocytic system, the Kupffer cells which are a type of macrophage (5).

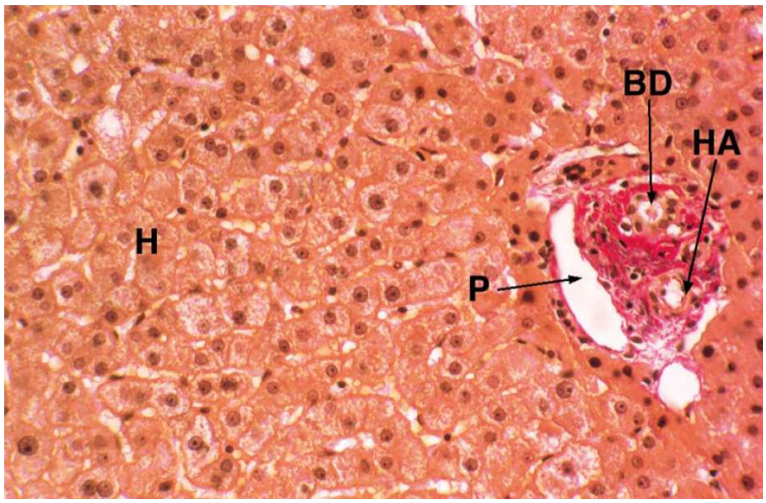

Figure 13. Normal liver tissue. H: hepatocytes, P: portal vein, BD: bile duct, HA: hepatic arteriole. Reproduced from [5].

2.2. Chronic Liver Diseases

2.2.1. Chronic Viral Hepatitis

Chronic hepatitis is not a single disease, but rather a clinical and pathological syndrome, which has several causes and is characterized by varying degrees of liver damage. For lack of a better definition of chronicity, chronic hepatitis is still defined as a disease that persists for at least six months (18, 19). The current classification of chronic hepatitis is based on the aetiology, activity of the inflammatory process (grading) and degree of fibrosis (staging). Globally, the most common aetiology of chronic hepatitis and cirrhosis is viral hepatitis B and C (18 - 20). Grading describes the necroinflammatory activity, which is based on the hepatocellular damage and inflammatory infiltration. Staging reflects the architectural alterations in the parenchyma that are due to fibrosis and cirrhosis (5). Fibrosis is characterized by an increase in collagen production (types I and III) and consequent deposition in the extracellular matrix, while cirrhosis represents the last stage of fibrosis progression. It is characterized by fibrosis, nodular regeneration of the liver parenchyma and vascular disturbance such as capillarization of the sinusoids and

intrahepatic shunts. The introduction of liver biopsy in the medical setting has revolutionized hepatology since the 1960s. Several semiquantitative systems, which are not directly comparable, have been proposed to assess chronic viral hepatitis and the most commonly used are the Ishak modification of the Knodell hepatic activity index and the METAVIR score (21). The latter, used in this project, stages fibrosis on a 5-point scale from F0 to F4 (cirrhosis), and grades activity on a 4-point scale from A0 to A3 (Table 2). A subclassification of cirrhosis was also proposed using the Laennec Scoring System that subdivides cirrhosis (F4) into F4 A (mild), F4 B (moderate) to F4 C (severe) (22). In chronic infection, the indication for treatment depends on the amount of fibrosis and aims to avoid the development of cirrhosis and hepatocellular carcinoma. The most clinical relevant end points are a fibrosis stage ≥ F2, which indicates the need for antiviral treatment, and the detection of cirrhosis (F4), which means that patients should be monitored for complications such as the development of portal hypertension and hepatocellular carcinoma (23). However, new triple therapy of HCV with increased response rates and decreased side effects may enlarge the indications for treatment to patients with < F2 fibrosis, making the detection of patients with ≥ F2 less crucial. Despite the widespread use of liver biopsy, there has been in the past decade an increased focus on its disadvantages. Apart from the invasiveness of the technique, which by itself carries risks, liver biopsy is subjected to sampling error (due to the small liver sample) and it suffers from intra- and interobserver variation (4, 21, 23). All these factors play an important role in its variability and highlight the fact that we are probably dealing with an imperfect gold standard. However, this perception has pushed even further the need to develop novel noninvasive biomarkers to screen and manage patients with chronic liver diseases.

Table 2. Metavir Scoring System

SCORE METAVIR

Score A (activité)	
- Absente	A0
- Minime	A1
- Modérée	A2
- Sévère	A3

Score F (fibrose)	
- Absence de fibrose	F0
- Fibrose portale stellaire sans septa	F1
- Fibrose portale avec rares septa	F2
- Nombreux septa sans cirrhose	F3
- Cirrhose	F4

Reproduced from www.ccr.fr.

2.2.2. Nonalcoholic Fatty Liver Disease (NAFLD)

Hepatocellular steatosis is a hallmark in NAFLD. Liver steatosis is characterized by lipid overload and is defined as more than 5% of hepatocytes containing fat (Fig. 14) (24, 25). In NAFLD liver steatosis is most often macrovesicular, which means that there is a single large fat droplet inside the cytoplasm pushing the hepatocyte nucleus to the periphery. The presence of microvesicular steatosis (multiple tiny droplets) is rare, never exceeding more than 16%, and is frequently associated with a more severe disease progression (26). The most used histopathological quantification of liver steatosis (grades 0 to 3) refers to the percentage of hepatocytes containing fat (< 5%; 5 – 33%; 33 – 66%; > 66%) (27).

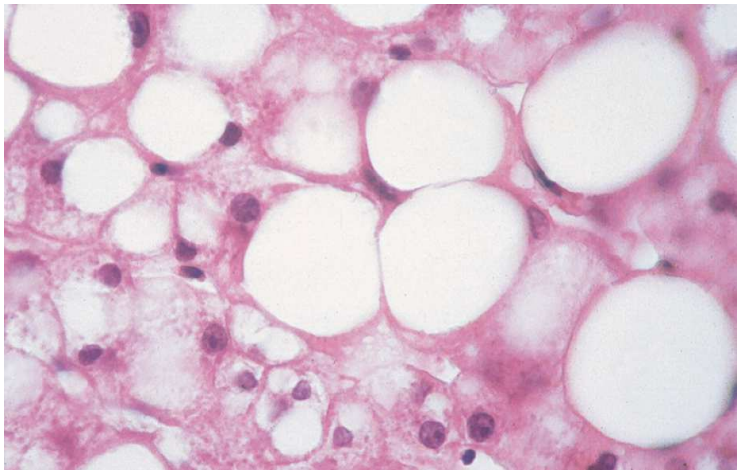

Figure 14. Liver slice with macrovesicular steatosis in a diabetic patient. Reproduced from [5].

NAFLD includes a spectrum of disorders and it ranges from nonalcoholic fatty liver (NAFL) to nonalcoholic steatohepatitis (NASH), progressive liver fibrosis and cirrhosis (28 - 30). In Portugal about 27% of the population is estimated to have NAFLD, which is currently considered the worldwide leading cause of chronic liver diseases being closely related to the growing frequency of obesity and insulin-resistant type 2 diabetes (1, 29, 31 - 33) (Figs 15, 16). The association of obesity and diabetes represents an added risk since in this case the prevalence of NAFLD, NASH and cirrhosis reaches almost 100%, 50% and 19%, respectively (29). NAFLD represents not only a considerable loss in the individual quality of life but also an increase in disease-related absenteeism and healthcare costs (3, 34).

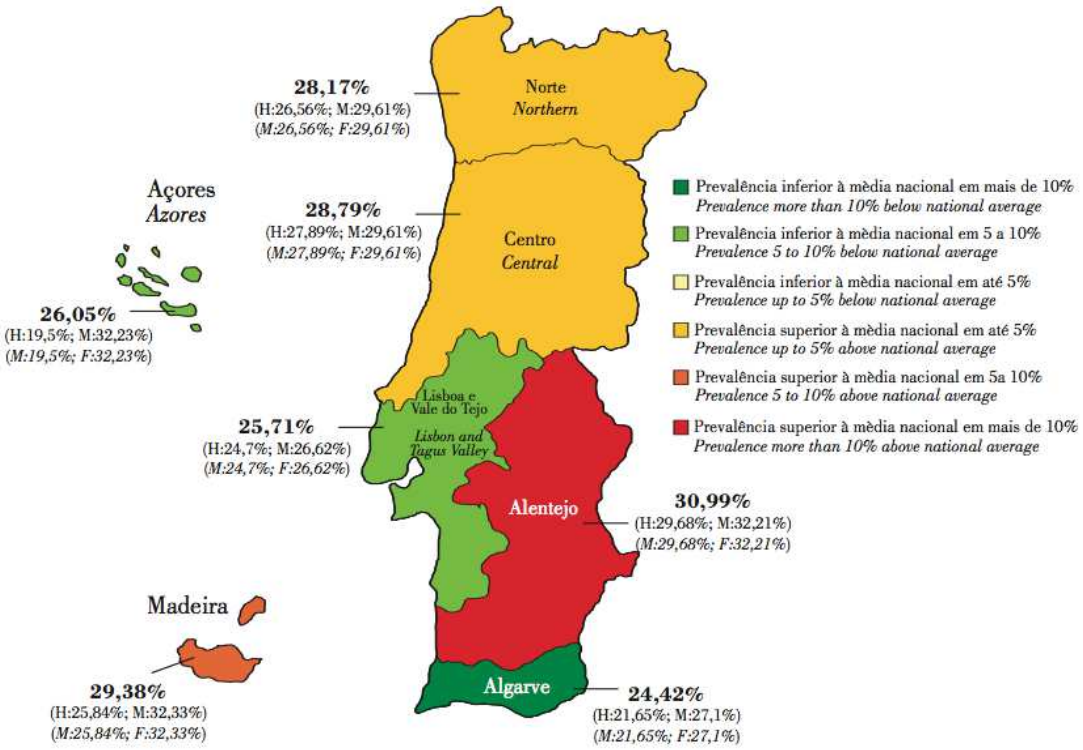

Figure 15. Color map of NAFLD prevalence based on the average national prevalence (27%).
Reproduced from [31].

Although early stages of liver steatosis may be reversible, still 25% of the patients with NAFL can progress to NASH, 50% of these will evolve to fibrosis and 10 - 29% to cirrhosis, ultimately leading to hepatocellular carcinoma (HCC) (24, 25). The evolution of steatosis, steatohepatitis, progressive liver fibrosis and cirrhosis is the result of a complex set of factors not yet fully understood. An inflammatory state has been associated with the development of NASH and liver damage, and a cytokine imbalance, in particular an increase in the ratio tumor necrosis factor-alpha/adiponectin, could be important in the development of NASH and correlate with disease severity, but the data available are limited (24, 29, 30). Currently, noninvasive markers for NAFLD include clinical signs and symptoms, laboratory tests, ultrasound and various combinations of these methods. Although useful, they lack the specificity and sensitivity to differentiate NAFL from NASH patients (35). Most patients with this disease are asymptomatic at presentation and

liver enzymes values such as aspartate aminotransferase and alanina transaminase frequently oscillate between normal and five times the upper limit. There have been cases where the full histological spectrum of NAFLD is present even with normal serum levels (4, 29, 30, 33).

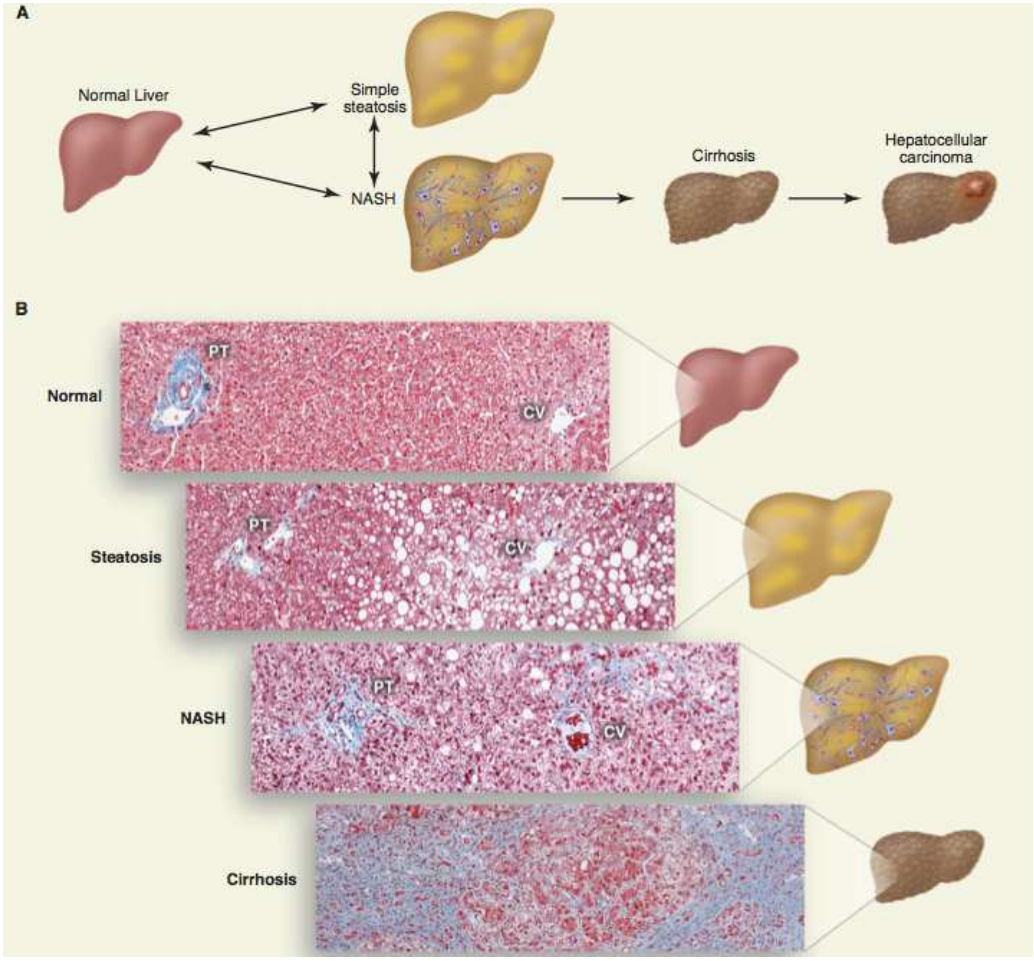

Figure 16. The disease spectrum of nonalcoholic fatty liver disease. (A) Schematic of progression of NAFLD. The accumulation of TG within lipid droplets in hepatocytes causes steatosis. Steatosis associated with inflammation, cell death, and fibrosis is referred to as NASH, which can progress to cirrhosis. Individuals with cirrhosis have an increased risk of hepatocellular carcinoma. (B) Histological sections illustrating normal liver, steatosis, NASH, and cirrhosis. Collagen fibers are stained blue with Masson's trichrome stain. The portal triad (PT), which consists of the hepatic artery, portal vein, and bile duct, and the central vein (CV) are shown. Reproduced from [24].

The existence of fibrosis is not required to diagnose NASH but a specific pattern of steatosis, hepatocyte hydropic ballooning (cell injury) and surrounding lobular

inflammation is essential (28). Although the presence of fibrosis does not represent a critical end point, the detection of fibrosis is by itself highly suggestive of NASH and is important to recognize. It should be noticed that in NASH adult patients the initial site of fibrosis (but also steatosis and ballooning) development is in acinar zone 3 while in viral hepatitides the initial fibrosis is portal and periportal (4, 27, 28). In 2005, the NASH Clinical Research Network (NASH CRN) proposed a scoring system (from 0 to 8) for disease activity based on the assessment of steatosis, ballooning and inflammation (Table 3) (27, 36).

Table 3. Nonalcoholic Fatty Liver Disease activity score

NAFLD activity score: 0–8		
Steatosis grade	Lobular inflammation	Hepatocellular ballooning
0: <5%	0: none	0: none
1: 5–33%	1: <2 foci/20 × optical field	1: mild, few
2: 34–66%	2: 2–4 foci/20 × optical field	2: moderate marked, many
3: >66%	3: >4 foci/20 × optical field	

Fibrosis score
0: none
1: 1a mild (delicate) zone 3 perisinusoidal fibrosis
1b moderate (dense) zone 3 perisinusoidal fibrosis
1c portal/periportal fibrosis only
2: zone 3 perisinusoidal fibrosis with portal/periportal fibrosis
3: bridging fibrosis
4: cirrhosis

Reproduced from [27].

Currently, the individual natural history of NAFLD is unknown and, unlike other chronic liver diseases, there are no algorithms to simplify its management and no specific pharmacological treatment (3, 36).

2.3. Noninvasive Techniques to Assess Liver Fibrosis, Inflammation and Steatosis

To overcome the complications and limitations posed by liver biopsy, alternative noninvasive methods ranging from serum biomarker assays to advanced imaging techniques have been developed for the evaluation of liver fibrosis, inflammation and steatosis.

Section 2.3.1. will briefly review current noninvasive serum biomarkers. In the next two sections noninvasive imaging modalities will hence be detailed. Section 2.3.2. will focus on imaging techniques not directly related to this project and the final section 2.3.3. will thereafter provide greater detail on Ultrasound-based Supersonic Shear Imaging and Magnetic Resonance, which are the basis for all studies presented in the current project.

2.3.1. Noninvasive Serum Biomarkers

Several noninvasive serum biomarkers have been studied to assess fibrosis, particularly in viral hepatitis C, which can be divided in direct and indirect markers of extracellular matrix remodeling. Amongst direct biomarkers we currently have hyaluronan, laminin, procollagen III, type IV collagen and YKL - 40, which have variable reported performances for the diagnosis of significant fibrosis. They all lack large-scale independent studies (Table 4) (23, 37). Among indirect serum biomarkers the most commonly used are the aspartate-to-platelet ratio and FibroTest. The latter combines five biochemical markers (haptoglobin, α_2-macroglobulin, apolipoprotein A1, γ-glutamyltransferase and bilirubin). These biomarkers demonstrate greater utility in the detection of advanced fibrosis than intermediate and early stages, whose patients are more likely to benefit from therapeutic intervention. Moreover, they produce false positives in patients with hyperbilirubinemia

and elevated aminotransferases levels. In patients with viral hepatitis B noninvasive composite scores are not as well validated (21, 23). The accuracy and clinical usefulness of serum biomarkers to detect liver inflammation is yet to be determined. Although caspase-cleaved cytokeratin-18 fragments have shown some promise to distinguish patients with NAFL from those with NASH (AUROC of 0.82 - 0.83) their use is still limited to clinical trials (38). A common flaw to these biomarkers is also that their utility in following disease progression is still currently unknown.

Table 4. Performance of different serum biomarkers to detect fibrosis stages ≥ F2 and F4

	AUC		Sensitivity (%)		Specificity (%)		PPV (%)		NPV (%)	
Index	≥F2	F4	≥F2	F4	≥F2	F4	≥F2	F4	≥F2	F4
Hyaluronan	0.73–0.86	0.89–0.92	64.5–75	79.2–100	81.0–91.2	80.0–89.4	44.0–86.3	63.0–100	78.5–93	99.0–100
Laminin	0.77–0.82	N/A	80.0	N/A	83.0	N/A	N/A	N/A	N/A	N/A
YKL-40	0.70–0.81	0.80	78	80	81	77.0	61.2–80	73	68.4–79	78.0
Collagen type IV	0.74–0.83	0.60	65	60	69	61	67	61	66	60
Procollagen III	0.69–0.75	0.73–0.79	70–78	60–77	63.4–75	74–66	76	69	77	67
Fibrometer®	0.85–0.89	0.91	80.5–89	94.1	84.1–89.9	87.6	82–86.3	68	77.6–82.5	94.7
FibroSpect®	0.82–0.87	N/A	71.8–93.0	N/A	66–73.9	N/A	60.9–82.6	N/A	77.7–94	N/A
Hepascore®	0.79–0.85	0.85–0.94	53.0.8–82	71–76.5	65–92.0	84–89.8	70–88	64.9	63.5–78	89.6–98
ELF score	0.80	N/A	90	N/A	31	N/A	27.5	N/A	92	N/A
AAR	N/A	0.51–0.83	N/A	46.7–78	N/A	95.9–100	N/A	73.7–100	N/A	80.7–89
APRI	0.69–0.88	0.61–0.94	41–91	57–89	47–95	75–93	61–88	38–57	64–86	93–98
Lok index	N/A	0.78–0.81	N/A	37–92	N/A	30–94	N/A	32–75	N/A	84–91
Forns' index	0.60–0.86	N/A	79.8–94	N/A	61.2–95	N/A	66–94.7	N/A	63.8–96	N/A
Fib-4	0.82–0.89	0.79–0.91	37.6–74.3	N/A	80.1–98.2	N/A	82.1	N/A	94.7	N/A
Fibrotest®	0.74–0.87	0.71–0.87	65–77	50–87	72–91	70–92.9	76–80	57.9–93	66.7–81	44–90.5

AUC, area under the receiver operating characteristic curve; N/A, not available; AAR, AST-to-ALT ratio; APRI, AST-to-platelet ratio index; NPV, negative predictive value; PPV, positive predictive value. Adapted and reproduced from [37].

2.3.2. Overview of Imaging Techniques not Related to this Project

- *Liver Ultrasound*

Ultrasounds are sound waves traveling in pulses with frequencies higher than the ones audible by the human ear (> 20,000 Hz). Piezoelectric crystals in an ultrasound transducer

generate a pulse and ultrasound imaging depends on the reflection of those sound waves, which then become echos. The ultrasound device processes the returning echos and assigns them a level of gray, somewhere between black and white, correlating to that signal's amplitude, or strength, and an image is immediately visible on a screen (39).

Ultrasound is widely used in clinical practice to detect fatty infiltration of the liver. Steatosis increases liver echogenicity making the liver appear brighter than the cortex of the right kidney or the spleen (Fig. 17) (39). The initial stages of fibrosis may have very little effect on the ultrasound appearances of the liver, but at advanced stages the liver is more reflective, giving the appearance of a bright liver often with a coarse texture (40). The association of fibrosis with fatty changes further complicates the clinical picture, since both increase liver echogenicity. Ultrasound is unable to provide a precise grading and staging of steatosis and fibrosis, respectively. Moreover, its sensitivity is reduced in the morbidly obese patients and its performance is highly operator-dependent (35).

Figure 17. Liver steatosis assessed by B-mode ultrasonography. The liver (circle) is brighter than the right kidney, represented at the inferior left corner of the image.

Only few studies have used contrast-enhanced ultrasound and time intensity curve analysis

to assess NASH and liver fibrosis (41, 42). Iijima et al (41) showed that the accumulation of ultrasound contrast microbubbles in the liver parenchyma is decreased in patients with NASH but not NAFLD, which led to lower peak signal intensity and faster decrease in the measured signal intensity over time in NASH patients. However, the authors did not find any correlation between these measurements and fibrosis and steatosis as assessed by histopathology. In the work by Orlacchio et al (42) in patients with viral hepatitis C, a significant correlation was found between liver parenchyma peak signal intensity and fibrosis staging. Moreover, liver parenchyma peak signal intensity was able to distinguish patients with F1 *vs* F2 and F2 *vs* F4 fibrosis scores. However, intra- and interobserver agreement and technique reproducibility were not assessed in the study.

- *Transient Elastography (TE)*

The effectiveness of palpation as a diagnostic tool to detect disease has lead to the development of imaging techniques able to assess the changes in the mechanical properties of an organ, such as the liver, with increased fibrotic tissue. Transient elastography is a unidimensional ultrasound-based method that determines tissue stiffness by measuring the propagation of a shear wave in the liver. This device contains a transducer, used both as receiver and emitter, mounted on a mechanical vibrator that with a short, mild amplitude and low frequency (50 Hz) tone burst (transient) generates the shear wave. An important feature of this method is that the mechanical vibration has to be transient to avoid reflections and interferences occurring within the tissue (43). The stiffer the tissue, the faster this shear wave propagates. TE is rapid, easy to perform and painless, measuring liver stiffness in a cylinder of 1-cm wide per 4-cm long, around 25 - 65 mm below skin surface, which results in a tissue volume 100 times larger than the biopsy specimen

(Fig. 18) (23, 44). Although the results are immediately available in kiloPascals (kPa), a cautious interpretation of data is needed and all the following conditions must be fulfilled: at least 10 valid measurements, a success rate (ratio of valid measurements to the total number of measurement) > 60% and an interquartile range (IQR; which reflects variations among measurements) of less than 30% of the median value (IQR/M, ≤ 30%) (Fig. 19). Uninterpretable data or failed examinations still occur in at least 16 - 20% of patients with a body mass index (BMI) ≥ 28 kg/m^2, in patients with narrow intercostal spaces and in the presence of ascites (23, 44). Moreover, the measurement place is confined to the right liver edge, which limits the analysis of the liver parenchyma.

Figure 18. Left: Probe positioning to measure liver stiffness with Transient Elastography. Right: Representation of the explored liver volume. Reproduced from [44] and from www.apef.com.pt (Associação Portuguesa para o Estudo do Fígado).

Figure 19. Measurement image for Transient Elastography. The result of 3.9 kPa indicates that the patient has an F0 fibrosis stage. Reproduced from www.jle.com/fr ("Le FibroScan®: un nouvel outil pour l'évaluation non invasive de la fibrose au cours des maladies chroniques du foie").

Liver stiffness values measured with transient elastography have been well correlated with mild and severe fibrosis stages (AUROC 0.79 - 0.98) in a wide range of patients with chronic liver diseases, but its performance is limited for the intermediary stages of fibrosis (23, 45, 46). Moreover, fibrosis is frequently associated with other parenchymal changes and a significant increase in liver stiffness has recently been observed in *in vivo* and *in vitro* studies in the presence of edema, inflammation, steatosis and cholestasis (45 - 49). This overestimation of liver stiffness and the consequent fibrosis overstaging have very important clinical consequences in terms of treatment and patient follow-up.

- *Accoustic Radiation Force Impulse (ARFI)*

Acoustic radiation force impulse imaging is a radiation force-based imaging method that is provided by conventional B-mode ultrasonography. ARFI imaging involves transmission of an initial ultrasonic pulse, at diagnostic intensity levels, to obtain a baseline signal for later comparison. An acoustic pushing pulse with short-duration (0.3 msec) and high-intensity is afterwards transmitted by the same transducer. This induces a shear-wave that

propagates away from the region of excitation and generates localized displacements in the tissue, which are measured by a series of diagnostic intensity pulses (43). The propagation speed of the shear wave (m/sec) is measured in a cylinder of 10-mm long per 6-mm wide, which is smaller than the one for transient elastography, but has the advantage of being chosen by the operator who is able to place it avoiding large vessels or liver lesions (Fig. 20) (23). ARFI demonstrates a stepwise increase in mean velocity with increasing fibrosis stages. The diagnostic accuracy (AUROC) for the detection of mild and severe fibrosis was found to vary between 0.74 - 0.98 (50). In several studies ARFI was as accurate as transient elastography for the assessment of patients with severe fibrosis, but it should be noted that in one of these studies patients in the control group had velocities in the cirrhotic range (23, 38, 44, 51, 52). As opposed to TE this method can be implemented on regular ultrasound equipment, the region of interest is chosen by the operator and overcomes the reported limitations for TE such as ascites and obesity (23). However, ARFI still requires further validation in larger cohorts of patients and with diverse chronic liver diseases.

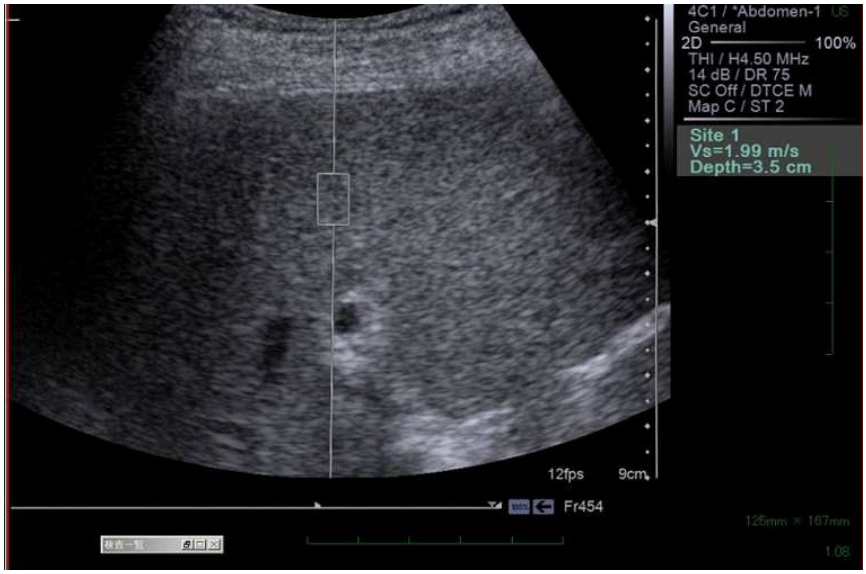

Figure 20. Measurement window for ARFI elastography. Reproduced from www.intechopen.com.

- *Computed Tomography (CT)*

Multidetector CT systems use x-ray tubes and x-rays detectors around the patient. CT measures the attenuation of the liver, which can be expressed as an absolute value (in Hounsfield Units), or a ratio, by comparing it to that of the spleen. At unenhanced CT, the normal liver has a slightly greater attenuation than the spleen and intrahepatic vessels are visible as hypoattenuating structures (Fig. 21). Liver steatosis is diagnosed if the measured liver attenuation is at least 10 HU less than that of the spleen. In severe liver steatosis, the intrahepatic vessels appear hyperattenuated relative to the liver tissue (Fig. 22). A measured liver-to-spleen attenuation ratio of less than 1 is indicative of fatty liver (35, 40, 53). However, liver attenuation is influenced by other factors such as edema, fibrosis, iron and copper and glycogen, which induce errors in fat quantification. Furthermore, the concomitant presence of liver steatosis and iron will induce opposite effects on liver attenuation. Thus, this technique has a poor performance as a screening tool, particularly in patients with mild steatosis (40, 53).

Figure 21. Normal appearance of the liver at unenhanced CT. The attenuation of the liver (66 HU) is slightly higher than that of the spleen (56 HU), and intrahepatic vessels *(v)* appear hypoattenuated in comparison with the liver. Reproduced from [40].

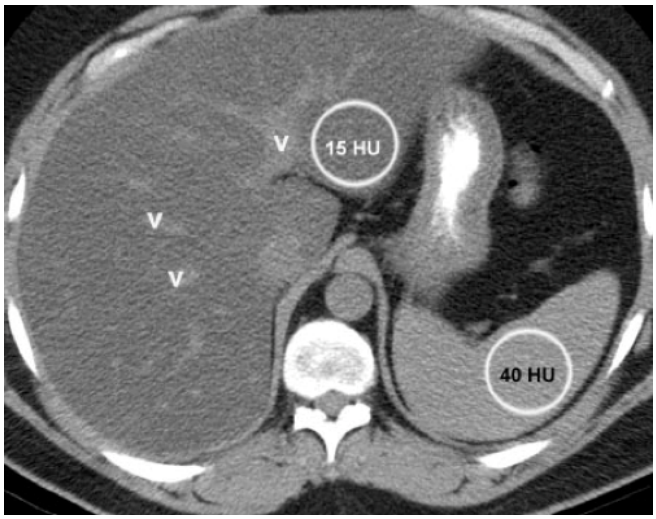

Figure 22. Diffuse fat accumulation in the liver at un- enhanced CT. The attenuation of the liver (15 HU) is markedly lower than that of the spleen (40 HU). Intrahepatic vessels *(v)* also appear hyperattenuated in comparison with the liver. Reproduced from [38].

Dual-energy CT with different tube potentials (140 and 80 kVp) can however present some advantages in the evaluation of liver steatosis, since the steatotic liver has more strikingly attenuation changes than normal liver with the different tube potentials (Fig. 23) (54). The attenuation difference is between 1.7 – 5.8 HU in mildly steatotic liver, 5.9 – 9.9 HU in moderately steatosis and more than 10 HU in the severely steatotic liver. However, this difference is attenuated in livers with concomitant iron and fat deposition (54).

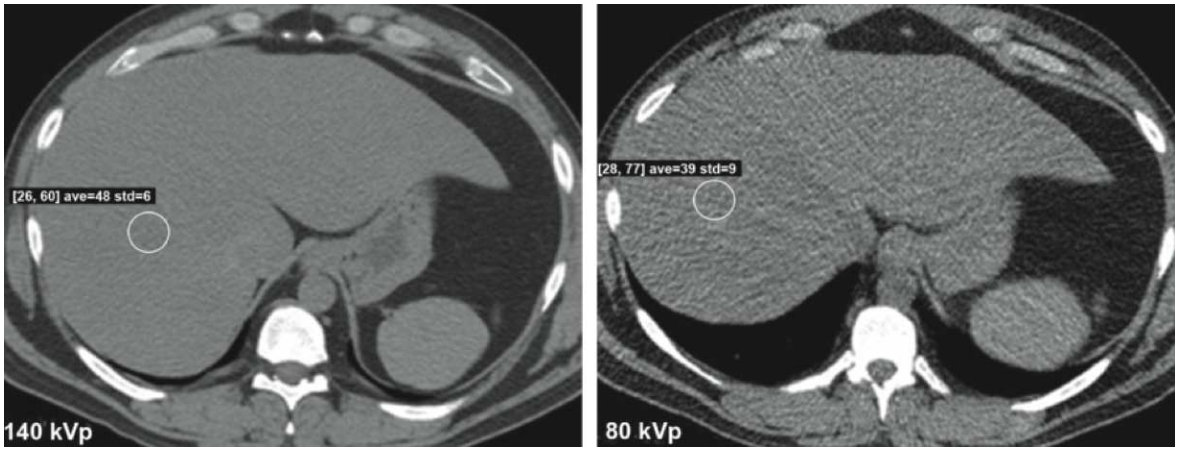

Figure 23. Dual-energy CT evaluation of liver in a 45-year-old male potential donor for living transplantation. Axial unenhanced CT scans obtained at 140 kVp **(left image)** and 80 kVp **(right image)** show a hepatic attenuation difference of 9 HU, a finding indicative of moderate hepatic steatosis. Reproduced from [54].

Recently, CT was found to be useful in the assessment of liver inflammation and mild to moderate fibrosis in patients with chronic liver diseases. The measurements of the xenon solubility coefficient and portal venous tissue blood flow, with xenon-based computed tomography, were able to discriminate between patients with simple steatosis and advanced NASH (i.e., presence of bridging fibrosis) (55). Additionally, the measurement of the mean transit time with perfusion CT was found to have an early increase in patients with fibrosis but the performance of this parameter to dichotomize patients with F1 vs F2-3 fibrosis stages was only moderate (56, 57). The studies with CT not only need further validation but also expose the patients to ionizing radiation.

2.3.3. Imaging Techniques used in the Current Project

- *Real-time ShearWave Elastography (SWE)*

Liver stiffness measured by ultrasound-based methods can be described in both physics and mechanics as the Young's modulus (E), which represents the mechanical response of the liver to the shear stress and is expressed in kiloPascals (kPa) (43). In contrast to transient elastography that creates a transient excitation with a low frequency wave of 50 Hz, shearwave elastography uses radiation force with a large frequency bandwidth, from 60 to 600 Hz ("shear wave spectroscopy"), which allows a more precise analysis of the mechanical behavior in the tissue. The ultrasound probe of the device creates a "supersonic mach cone" in the liver as ultrasounds are focused successively at different increasing depths (10 mm apart), almost simultaneously and perpendicular to the patient's skin (Fig. 24). The different spherical waves generated by each focus, interfere along this "mach cone" and create a conical shear wave front on both sides of the focal points propagating at

a speed of 2 m/s (Fig. 24) (43, 58, 59).

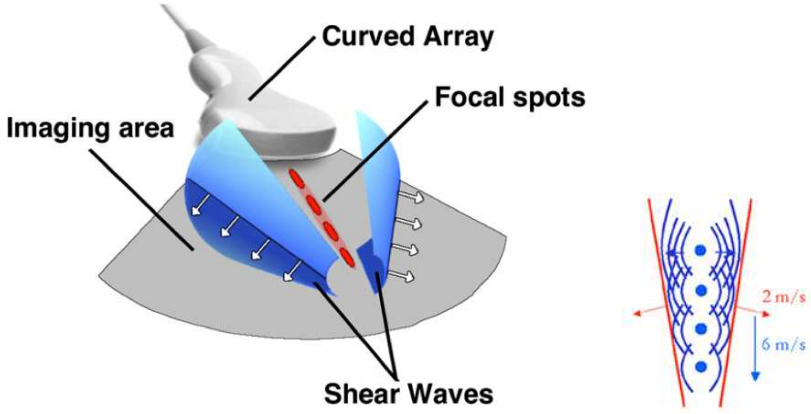

Figure 24. Left Image: generation of the Mach Cone shear waves from pushing beams at increasing depths. Right Image: Propagating velocities of the shear waves (2 m/s) and pushing beams (6 m/s). Adapted and reproduced from [58, 59].

The progression of the shear waves is captured by the very rapid acquisition ultrasound imaging system with good temporal resolution, typically up to 20,000 frames per second (i.e., Supersonic Shear Imaging). With this method the operator easily chooses the region of interest (ROI) in the liver for specific measurements. This ROI tool, "Q-box", allows measuring an area that ranges from 1 to 7 cm^2 up to 7 cm below the Glisson's capsule (Fig. 25) (58, 60). The propagation speed of the shear wave is displayed in the monitor of the ultrasound device, on a pixel-by-pixel-based colour map at the same time as a B-mode image. For each one of the pixels of the colour map there is a corresponding stiffness value. The operator is able to assess the stiffness colour of a specifically chosen liver region and obtains the mean stiffness value and standard deviations for that same area (Fig. 25). One important advantage of this ultrafast imaging (it takes only a few milliseconds), is that neither patient nor operator movements will influence the measured liver stiffness. Moreover, as opposed to ARFI, which only evaluates elasticity at a focal point, SWE assesses elasticity using a shear wave front as explained previously (Table 5).

Table 5. Characteristics of the quantitative elastography techniques

	TE	ARFI	SWE
ROI chosen by operator	N	Y	Y
Shear wave generation mode	Mechanical vibration	Radiation force	Radiation force
Frequency	50 Hz	Wideband	Wideband
Real-time images	N	Y	Y
Possibility to evaluate lesions	N	Y	Y
Influenced by ascites and obesity	Y	N	N

N, no; Y, yes; TE, Transient Elastography; ARFI, Accoustic Radiation Force Imaging; SWE, ShearWave Elastography.

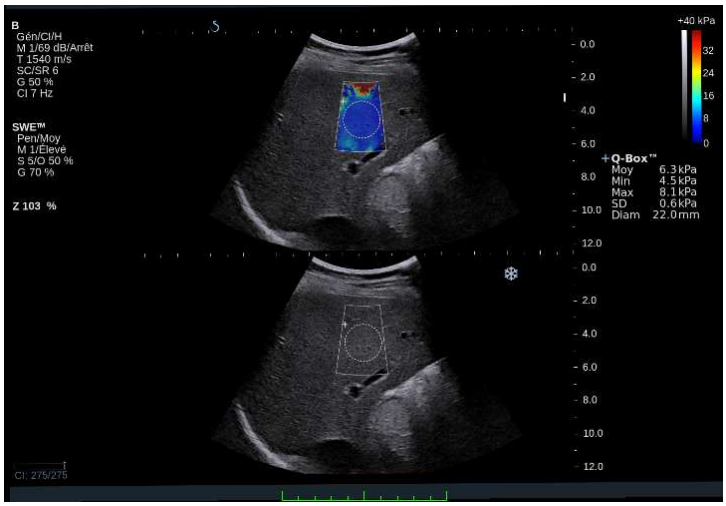

Figure 25. Measurement window for ShearWave Elastography.

Only one study compared real-time SWE with TE and used liver biopsy for all patients as the reference standard (60) The authors found that SWE could more accurately

discriminate patients with a fibrosis stage F0-1 *vs* ≥ F2 (AUROC 0.92 *vs* 0.84, *P* = 0.002; SWE *vs* TE, respectively). However, the difference between both methods was not significant for patients with a F3 fibrosis stage or cirrhosis (AUROC 0.98 *vs* 0.96, *P* = 0.14 - 0.48; SWE *vs* TE, respectively). The resulting cut-offs for SWE derived from this work, according to the fibrosis stages, are shown in table 6. This work included patients with chronic hepatitis C and low prevalence of obesity. This method still requires further validation in the clinical setting.

Table 6. Median values obtained for each fibrosis stage with SWE and TE

METAVIR Stage	Method	F0-F1	F2	F3	F4
Median value, kPa	SWE	6.2	7.6	10.0	15.6
	TE	5.6	6.4	9.1	19.8
IQR	SWE	5.1-6.8	7.2-8.3	9.2-10.1	12.8-18.8
	TE	4.5-6.5	5.4-8.0	8.4-11.6	13.4-23.0
Range	SWE	4.5-9.3	5.6-13.0	8.9-12.0	8.0-22.5
	TE	3.5-8.9	3.6-10.2	6.1-20.8	6.4-36.3
Number of outliers	SWE	1	2	1	0
	TE	0	0	2	0
P value	SWE		0.0001*	0.003**	0.09***
	TE		0.02*	0.002**	0.06***

IQR, Interquartile range; kPa, kiloPascals; P values refer to differences between consecutive fibrosis stages (*F0-F1 versus F2; **F2 versus F3; ***F3 versus F4). Reproduced from [60].

- ***Magnetic Resonance Imaging (MRI)***

a. Basic Concepts and Physical Principles

The human body is approximately 70% water and MRI uses the signal from these Hydrogen (^{1}H) protons to generate images. The proton rotates around is own axis and since it has an electrical charge it behaves live a small magnet, called the magnetic moment. When protons are exposed to an external magnetic field (B_0) they align in with the direction of the field and start to wobble, which is called precession (Figs. 26 - 28). The precession occurs at a characteristic frequency (Larmor Frequency), which is directly

proportional to the strength of the external magnetic field and is given by the Larmor equation (61, 62):

$$\omega_0 = \gamma_H B_0 / 2\pi \qquad \text{[Equation 1]}$$

where, ω_0 is the Larmor frequency (MHz), γ_H the gyromagnetic ratio specific to the hydrogen nucleus (42.58 MHz T^{-1}) and B_0 the strength of the magnetic field in Tesla (T).

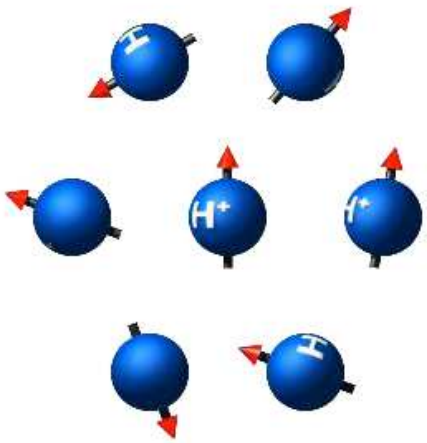

Figure 26. Random alignment of spins without an external magnetic field. Image reproduced from IMAIOS.

Hydrogen protons have a Larmor frequency of 63.9 MHz at 1.5 T. When the spins suffer the influence of B_0, and according to the classical theory, they tend to align into a parallel and anti-parallel manner. However, the parallel alignment is slightly prefered because the spins reside in a more favorable energy state. The difference between both alignments creates the net magnetization vector (NMV) or longitudinal magnetization that increases with higher field strenghts (Fig. 27) (61). This also happens in the earth's magnetic field but the resulting longitudinal magnetization is considerably weaker than the one in an MR

unit.

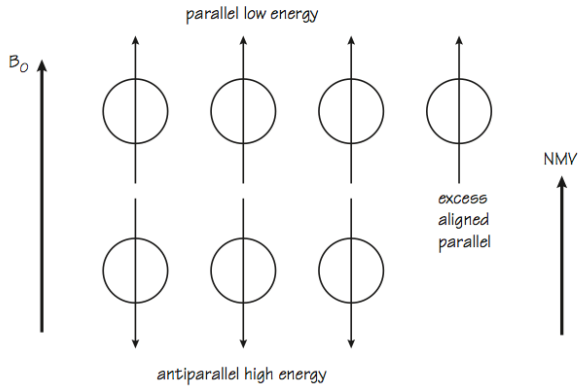

Figure 27. Alignment of spins: parallel and antiparallel with an external magnetic field. Reproduced from [62].

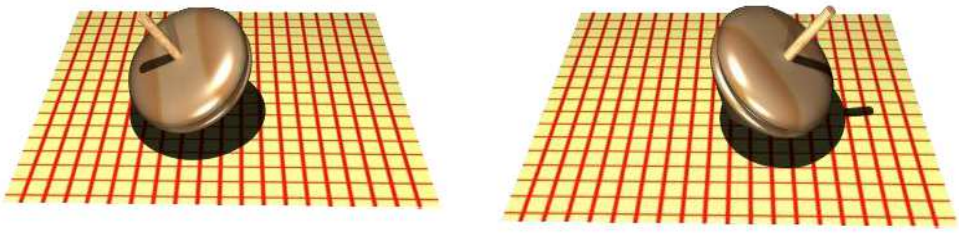

Figure 28. The wobbling spin is frequently compared to a spinning top. Images reproduced from IMAIOS.

At this time the system is at equilibrium. When we apply a radiofrequency pulse (RF), by means of a coil, with exactly the same frequency as the proton Larmor frequency, we create the resonance condition. At this time spins are at an excited state and with a 90º pulse, all the longitudinal magnetization is flipped into a transverse plane (Fig. 29). The resulting magnetization is now called transverse magnetization. Whenever transverse magnetization is present, it rotates around its axis and induces a voltage in a receiver coil creating the MR signal (Fig. 30) (61, 62).

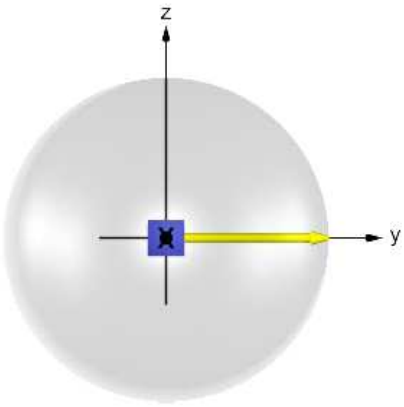

Figure 29. **Transverse magnetization in the XY plane after the RF pulse.** Image reproduced from IMAIOS.

Once the RF pulse is turned off the MR signal rapidly starts to fade away. Two independent processes (spin-lattice and spin-spin interaction) decrease transverse magnetization and induce a return to the initial equilibrium energy state, while recovering longitudinal magnetization (61, 62).

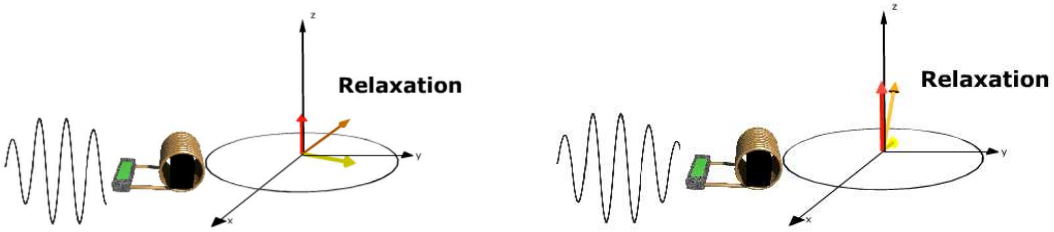

Figure 30. Coils transmit the MR signal. This signal is rapidly decreased due to the decay in transverse magnetization and the consequent increase in longitudinal magnetization (return to a stable energy state in axis Z). Images reproduced from IMAIOS.

Longitudinal relaxation is the recovery of the net magnetization vector along the Z axis. This recovery is exponential in time, with a characteristic time T1 (longitudinal relaxation time). Dissipating the spins energy into the surrounding medium makes the return to the initial equilibrium energy state and this process is called spin-lattice interaction.

Transverse relaxation is the decay of transverse magnetization in the XY plane. This decay is exponential in time, with a characteristic time T2 (transverse relaxation time). The energy exchange for this process is due to energy transfer between spins (spin-spin interaction). This process is called T2 recovery. However, inhomogeneities of the external magnetic field (caused by insufficient magnet shimming, the magnetic field generator and the patient being imaged) further contribute to the decay of the transverse magnetization and the sum of the two processes leads to T2* recovery. Thus, the exponential loss of MR signal is caused by T2* effects, and is called the free induction decay (FID) (61, 62).

The T1 and T2 relaxation times are intrinsic MR image contrast parameters and depend on the tissue of interest that is being imaged. They represent the time it takes to recover or reduce 63% of the longitudinal and transverse magnetizations, respectively.

Repetition time (TR) is the length of the relaxation period between two excitations pulses and therefore determines how much T1 recovery occurs in a particular tissue (Fig. 31). By choosing a short TR (< 600 ms) we increase T1-weighting i.e., the image contains mostly T1 information. Indeed, tissues with short T1 relax quickly and give a large signal (are bright) after the next RF pulse, while tissues with long T1 suffer very little relaxation and have less signal available (are dark) for the next excitation. Nuclei in fat tissue dissipate their energy to the surrounding medium very fast and have a short T1, but water takes a longer time to do it and therefore has a longer T1 (Table 7) (61, 62).

The Echo time (TE) is the interval between the application of the excitation pulse and the collection of the MR signal. TE determines how much T2 decay occurs in a particular tissue. If a short TE (< 30 ms) is chosen, the differences in signal between tissues will be very small since T2 decay has just started and the image will have a low T2 weighting (Fig. 32) (61, 62). However, a longer echo time will enable detection of different signal intensities in the tissues. Tissues with a long T2 will produce a stronger signal and appear

bright.

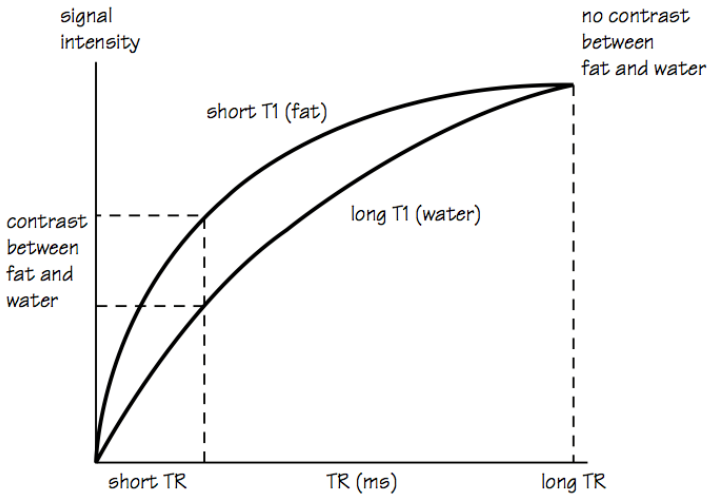

Figure 31. T1 differences between fat and water, according to the chosen short or long TR. Reproduced from [62].

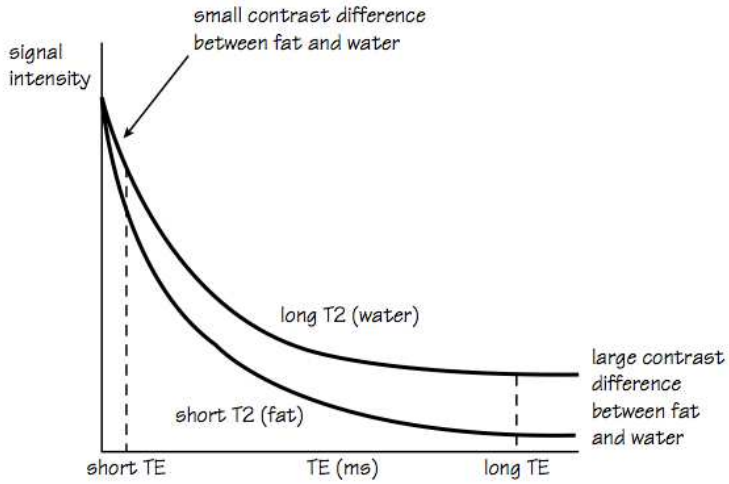

Figure 32. T2 differences between fat and water, according to the chosen short or long TE. Reproduced from [62].

A short TR and short TE sequence is usually called T1-weighted. A long TR and long TE sequence is usually called T2-weighted. In proton density-weighted images (PD) differences in the number of hydrogen protons in the tissues have to be demonstrated. To

reduce both T1 and T2 effects these sequences have a long TR and short TE.

Table 7. T1 and T2 relaxation times of different tissues at 1.5 T

	T1 (ms)	T2 (ms)
Water	3000	3000
Gray matter	810	100
White matter	680	90
Liver	420	45
Fat	240	85
Gadolinium	Reduces T1	Reduces T2

Note: T1 and T2 values shown for water represent the measured values in pure water and not water in biologic tissues. Reproduced from IMAIOS.

The selective excitation of a desired slice and identification of a signal origin will rely on the fact that the Larmor frequency is proportional to the magnetic field strength. The magnetic field is first made inhomogeneous by means of additional magnetic fields (gradients) applied in a specific direction. As a result, the magnetic field strength has a smooth change and each slice has now its own specific Larmor frequency. Therefore, the application of a RF pulse with the same frequency as the one of the desired slice, will only excite protons in that area leaving all the others unaffected (Fig. 33) (61, 62).

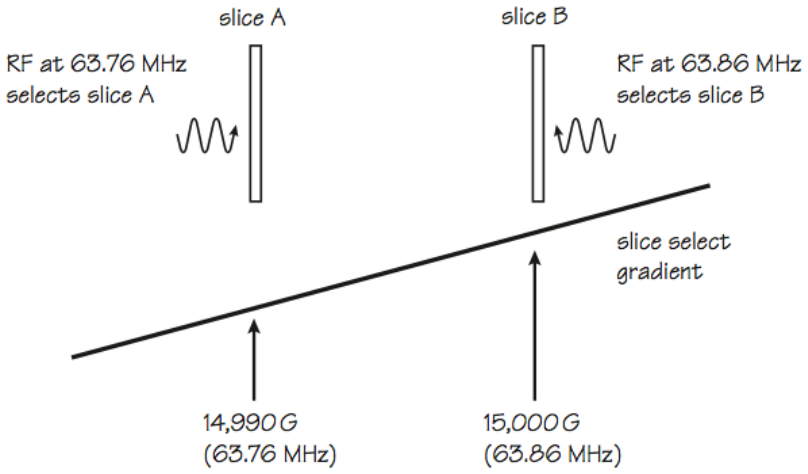

Figure 33. Slice selection. After applying the gradient, the magnetic field changes gradually and each slice has its own Larmor frequency. The magnetic field strength as a difference of 10 G between slice A and B. 1 T equals 10^4 Gauss (G). Reproduced from [62].

Spatial encoding identifies the spatial positioning of the MR signal and it involves two important steps: phase and frequency encoding. Each one of this steps uses a specific gradient, either phase or frequency-encoding gradient, that induces phase and frequency-shifts between the spins. All the collected data are stored in a mathematical area called the K-space that has a phase and frequency axis (Fig. 34). An MR image will be created after applying the Fourier transform to the raw data. Data-points in the center of the K-space determine contrast while those in the periphery determine the spatial information of the resulting images (63).

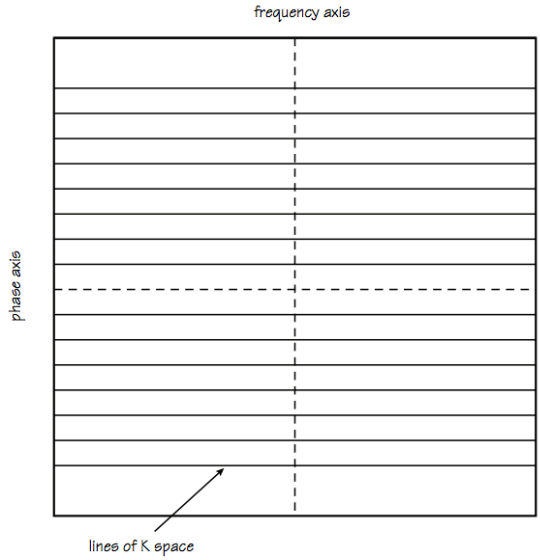

Figure 34. Graphical representation of the K space. Reproduced from [62].

The signal-to-noise ratio (SNR) is the relationship between the MR signal and the amount of noise in the image. A high SNR is desirable in clinical imaging. Parameters related to the MR unit field strength, emitter/receiver coils and sequence are able to increase or decrease the final SNR (Table 8).

Table 8. Parameters affecting signal-to-noise ratio (SNR)

Change in parameter	SNR
Increasing slice thickness	Increases
Increasing FOV	Increases
Reducing FOV in phase-encoding direction (rectangular FOV)	Decreases
Increasing TR	Increases
Increasing TE	Decreases
Increasing matrix size in frequency-encoding direction	Decreases
Increasing matrix size in phase-encoding direction	Decreases
Increasing NEX	Increases
Increasing magnetic field strength	Increases
Increasing receiver bandwidth	Decreases
Employing local coils	Increases
Partial Fourier imaging	Decreases
Fractional echo imaging	Decreases

FOV, field of view (distance across an image); Nex, number of averages. Reproduced from [61].

b. Basic Pulse Sequences

The Spin Echo (SE) pulse sequence uses a 90º pulse for excitation which changes all the magnetization into the XY plane, as previously explained. The transverse magnetization decays because some spins precess at a faster rate than others so after half the echo time a 180º pulse is applied to refocus ("reverse") the spins. At this time, those who were behind are now ahead and vice versa, and at the second half of the TE all spins will be again in phase. At this moment the echo is formed (Fig. 35). Since the 180º RF pulse eliminates de effect of field inhomogeneities but cannot compensate for the spin-spin interaction the signal decay is of the T2 kind. The spin echo sequence is characterized by an excellent image quality but long scan time (61 - 63).

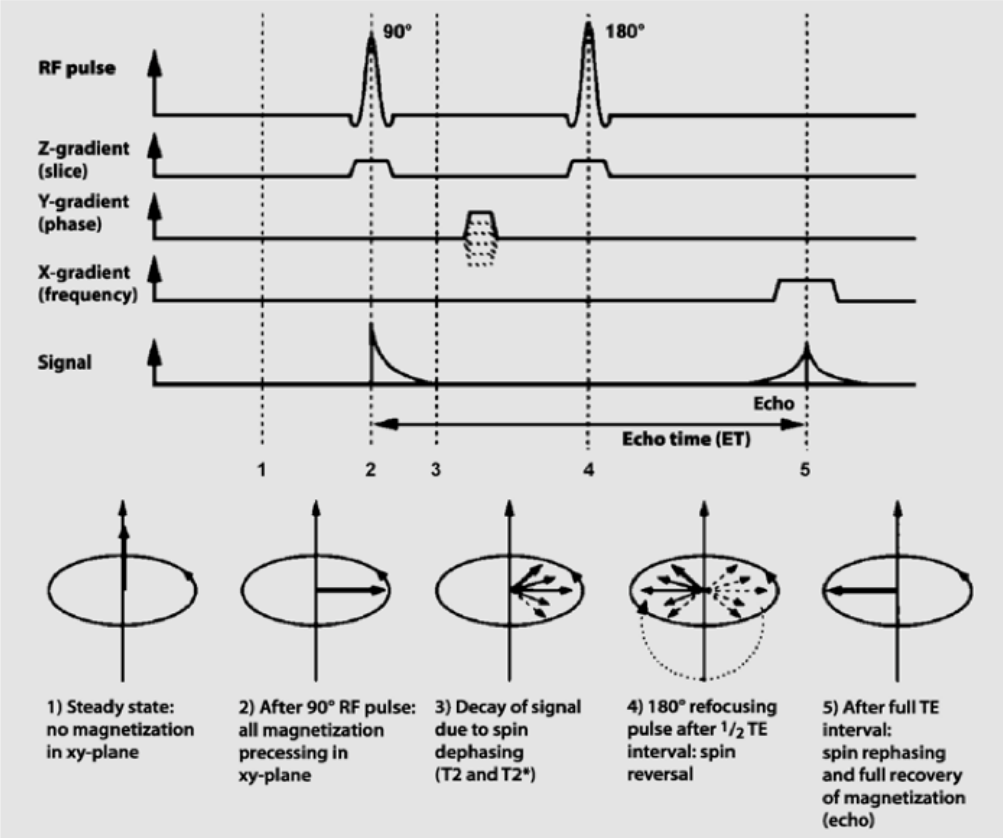

Figure 35. SE sequence. The excitation pulse always has a flip angle of 90°; the dephased spins are refocused into the spin echo by the 180° pulse. The dashed lines indicate the phase-encoding steps. Reproduced from [61].

The gradient echo sequence (GRE) uses gradient coils, rather than pairs of RF, to produce the dephasing and rephasing of spins (Fig. 36). A major advantage of using gradients and not the 180º RF pulse, is that a very short TR can be used, which allows faster imaging compared to the SE sequence. Since the static field heterogeneities are not corrected by the 180º RF signal decay is of the T2* kind (61 - 63).

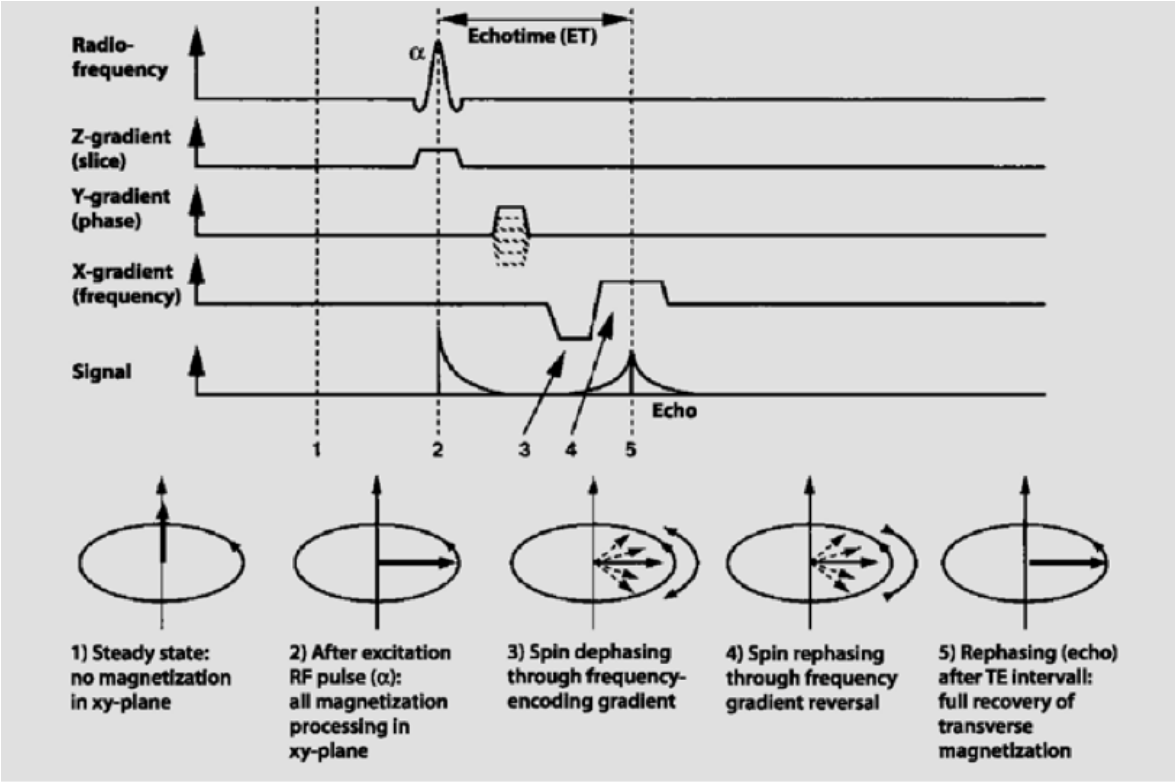

Figure 36. **Gradient echo sequence.** For the sake of simplicity, a flip angle α of 90° is assumed here as well. Reproduced from [61].

At this time a brief explanation is required about in-phase and opposed-phase GRE imaging, since this method has been used to detect liver fat for more than 25 years. The Larmor resonance frequency of fat protons is slower than that of water protons and they have a gap of approximately 210 Hz at 1.5 T (25, 64, 65). As shown in Figure 36 the two vectors in the transverse plane dephase with time and they will be in opposed-phase at half

the cycle and in-phase at the end of the cycle. The corresponding TE can be calculated according to the formula (25):

$$TE_n = n / 2 \times CS_{water\text{-}lipids} \times \omega_0 \quad \text{[Equation 2]}$$

Where TE is the echo time, $CS_{water\text{-}lipids}$ is the frequency gap between water and lipids and ω_0 is the Larmor frequency (MHz). These theoretical calculations show that water and fat peaks are in-phase (IP); i.e., the signals are summed ($IP = W_{ater} + F_{at}$) and in opposed-phase (OP); i.e., the signals cancel each other out ($OP = W_{ater} - F_{at}$) at 4.6 and 2.3 ms, at 1.5 T, respectively (25, 65). The signal from the fat fraction (FF) can be calculated with equation [3]:

$$FF = F_{at} / W_{ater} + F_{at} \quad \text{[Equation 3]}$$

Where F_{at} is the signal from fat and W_{ater} the signal from water. We can nonetheless rearrange the terms of this equation and fat fraction can therefore be calculated as follows:

$$FF = IP - OP / 2 \times IP \quad \text{[Equation 4]}$$

However, when performing this standard measurement (two echoes and high flip angle) errors are introduced in the final result because the T1 weighting of fat and the different T2* relaxations for water and fat are not taken into account. For greater detail please refer to chapter IV.

c. ^{1}H Magnetic Resonance Spectroscopy in the Liver (MRS)

Magnetic resonance spectroscopy can record proton signals as a function of their resonance frequency and is able to detect metabolites present in tissues at very small concentrations. MRS is currently considered the imaging reference standard for liver fat quantification and is extremely sensitive to even trace amounts such as 0.5% (65 - 67). The resonance frequencies of water and fat protons are distinct, which translates into different positions in the overall peak spectrum, and are expressed as a shift in frequency, in parts-per-million (ppm), relative to a standard. The area under each peak is used to calculate the metabolite concentration within a given voxel of tissue. Triglycerides are spectrally complex and have at least six different peaks: the dominant methylene peak (CH_2; 1.3 ppm), the methyl peak (CH_3; 0.9 ppm) and the 2.8, 2.1, 4.2 and 5.3 ppm peaks (Fig. 37) (66, 68). Measurements of the total lipids, frequently includes only the methylene peak (70 % of total fat peaks) or the methylene plus the methyl peaks (70% + 8%, respectively, of total fat peaks), because the 5.3 ppm peak overlaps with the one of water and the others are difficult to individualize at clinical field strengths (Fig. 38) (68). Water peak is located at 4.3 ppm (66, 68).

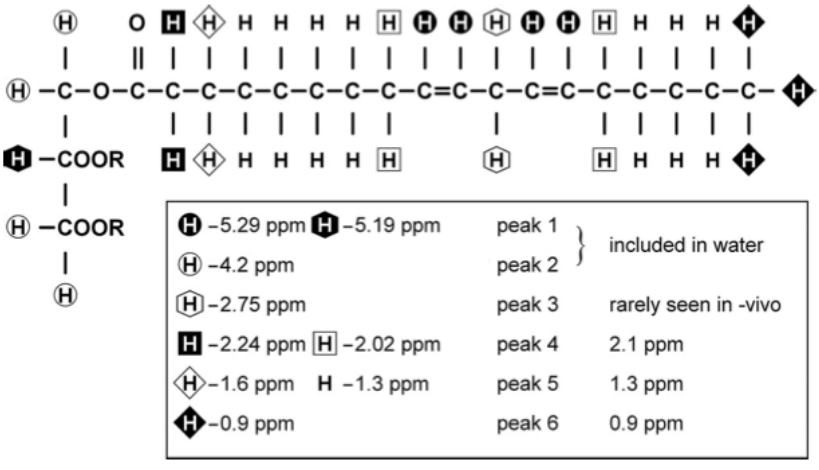

Figure 37. Representation of typical triglyceride molecule. The chain shown is linoleic acid. R indicates the other fatty acid chains in the triglyceride. Several resonances (at 5.29 and 5.19 ppm; 2.20 and 2.02 ppm; 1.6 and 1.3 ppm) are not resolvable in vivo at clinical field strengths (≤ 3 T) and appear as single peaks. Reproduced from [68].

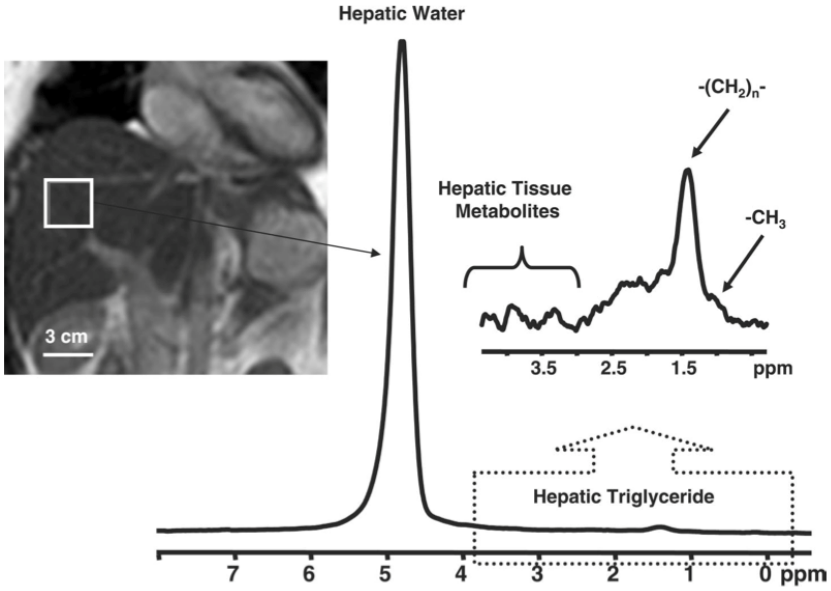

Figure 38. Left: coronal section of upper abdomen showing the region within the upper right hepatic lobe, in which measurement of liver triglycerides was obtained. Middle: proton spectrum from the liver, showing resonance peaks derived from hepatic water and triglycerides. Right: expanded view of the spectrum, highlighting resonances from protons of methylene (CH2), and methyl (CH3), in the fatty acid chains. Reproduced from [67].

MRS is technically challenging and to compensate for the low SNR, spectra are usually obtained from tissue volumes at least twice as larger than the voxels of water-based MRI and by repetitive signal averaging. Major drawbacks of this method are a substantially lower spatial resolution than the one for MRI and the longer time required for examinations and data post-processing (69).

MRS in the liver is usually performed as a single voxel technique (66). The main advantage is that the sampled volume is larger and therefore the SNR is increased. The two most commonly used spectroscopic sequences in the liver are the stimulated-echo acquisition mode (STEAM) and point-resolved spectroscopy (PRESS). In STEAM, a cubic voxel is generated with three orthogonal section-selective 90º pulses (Fig. 39). PRESS uses a 90º pulse followed by two 180º pulses (66, 69). Several studies compared the clinical performances of these two sequences. The volume of interest with STEAM is larger than

the one selected with PRESS and STEAM is also somewhat less sensitive to the J-coupling (i.e., interaction between spins within a molecule - also called spin coupling - which could cause these sequences to give different peak amplitudes). However, in STEAM only part of the available signal is used to produce the stimulated echo, thus PRESS has a higher SNR (by a factor of 2). There are still no specific recommendations as for the use of one or the other (66, 69 - 72).

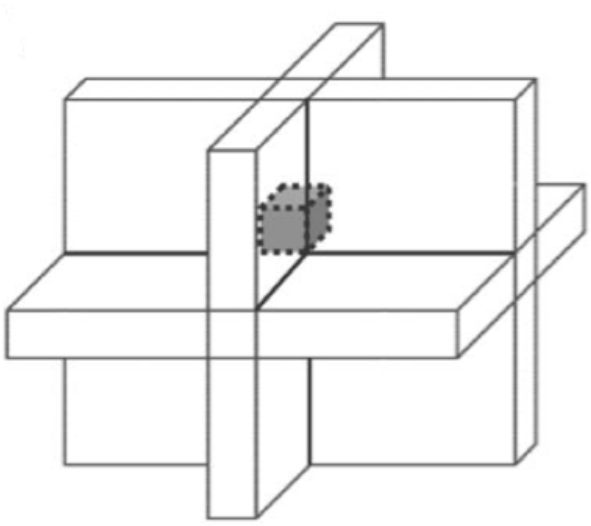

Figure 39. A 3D localized volume (voxel) is formed at the intersection of three orthogonal slices.
Reproduced from [72].

Although MRS is the imaging gold standard for liver fat quantification it has several limitations. First, it has limited spatial coverage, allowing measurements only at the voxel site. Second, it does require substantial expertise for its practical implementation. Third, even with automated post-processing it is still time-consuming in the busy clinical setting. Therefore, MRS is mainly limited to research and academic centers.

d. Intravoxel Incoherent Motion Diffusion-Weighted Imaging (IVIM DWI)

Diffusion reflects the random Brownian motion of water due to thermal agitation. At 37 ºC the water molecules have an average displacement of 30 micrometers during a 50-millisecond interval. This movement in biologic tissues suffers from the interaction of water molecules with cells, hydrophobic membranes, macromolecules (e.g. collagen in liver fibrosis) and vessels that will disturb free motion. Therefore the resulting diffusion is called apparent (ADC: apparent diffusion coefficient), and is considerably less than in pure water (73 - 76).

The original pulse sequence was based on a spin echo sequence that has symmetric diffusion sensitizing gradients inserted before and after the 180º refocusing pulse (Fig. 40). Water spins experience a dephasing induced by the first diffusion-sensitizing gradient and afterwards rephasing by the second gradient (74). The derived signal of stationary water spins is maintained as practically unaltered as the spins are at the same position during the two diffusion-sensitizing gradients. However, moving water spins will be in different positions and are not perfectly rephased by the second gradient, so the derived signal is reduced. The degree of water motion is proportional to the signal attenuation.

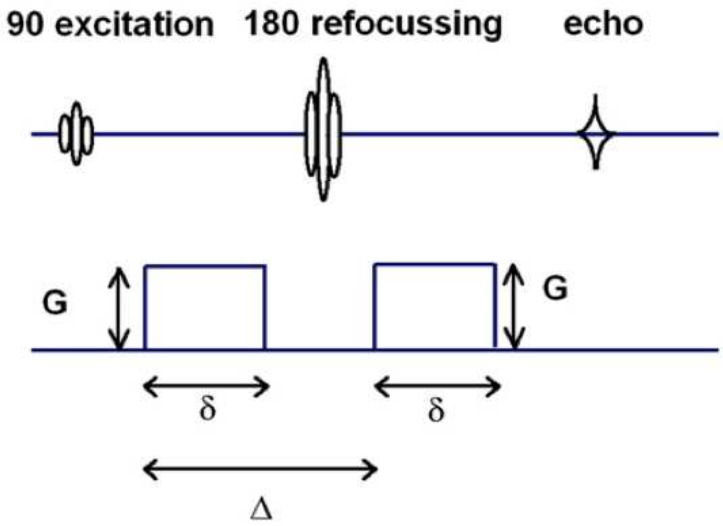

Figure 40. The Stejskal-Tanner pulsed field gradient (1965), is the default diffusion sensitive sequence. Two diffusion-sensitizing gradients inserted before and after 180º RF refocusing pulse using precisely controlled duration and distance. G, amplitude; δ, duration of the sensitizing gradient; Δ, time between the 2 sensitizing gradient lobes. Reproduced from [74].

Echo-planar imaging (EPI) is the gold standard DWI (diffusion-weighted imaging) technique. EPI is an ultrafast acquisition that uses oscillation gradient reversals to generate "odd" and "even" echoes that take significantly less time to be generated. Since EPI sequences are very sensitive to off-resonance effects of water and fat protons they are usually fat suppressed. Since liver is an isotropic organ (uniform in all directions) liver DWI uses tridirectional (x, y and z axis) diffusion gradients to calculate the average DWI image. The b-value provides diffusion weighting for DWI images. The higher the b-value, the more diffusion-weighted the image will be (low SNR), while at low b-values (< 100 s/mm^2) perfusion effects will dominate over diffusion weighting (high SNR) (76). ADC can be calculated as the slope of the signal attenuation as a function of b, expressed by the following equation using a mono-exponential fit (76).

$$S_b/S_0 = \exp^{(-b\ ADC)} \qquad \text{[Equation 5]}$$

where ADC (10^{-3} mm^2/s) is the apparent diffusion coefficient, S_b the signal intensity for each *b* value and S_0 the signal intensity at b_0.

The term intravoxel incoherent motion (IVIM) was first introduced in the clinical practice by Denis le Bihan in 1986, and translates the motion of water molecules at the voxel level, both intra- and extracellular but also in the capillary network. This theory allows the separation and measurement of pure diffusion and perfusion-related diffusion coefficients (Fig. 41). According to the IVIM theory, signal attenuation as a function of b is expressed by the following equation using a bi-exponential fit (76, 77):

$$S_b/S_0 = (1\text{-}f)^{\exp(-b\,D)} + f \exp^{(-b\,(D + D^*))} \qquad \text{[Equation 6]}$$

where S_b is the signal intensity for each *b* value, S_0 the signal intensity at b_0, f (%) the fraction of diffusion linked to microcirculation, D (10^{-3} mm^2/sec) the true diffusion coefficient, and D* (10^{-3} mm^2/sec) the perfusion-related diffusion coefficient.

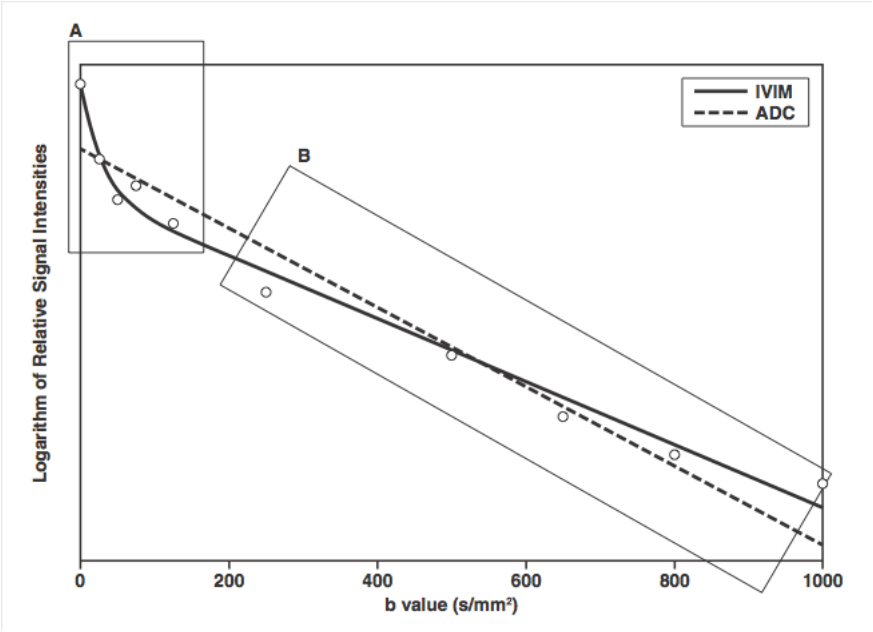

Figure 41. Plots show logarithm of relative signal intensity versus b value from normal liver parenchyma. Note that there is initially steeper decrease in plotted signal values (circles) at low b values (within rectangular box A) compared with more gradual attenuation of signal at higher b values (within rectangular box B). By applying intravoxel incoherent motion (IVIM) analysis, biexponential behavior of signal attenuation is characterized (solid *line)*, resulting in typical hockey stick appearance of fitted curve. Using simple monoexponential apparent diffusion coefficient (ADC) line fitted to data (dotted *line)* in this case provides suboptimal characterization of signal attenuation behavior. Reproduced from [77].

At high b-values (> 100 - 200 s/mm^2), the influence of D* on the signal decay is almost negligible and equation [6] can be simplified. D can therefore be calculated with a simple monoexponential fit (76, 77):

$$S_b/S_0 = \exp^{(-b\,D)} \qquad \text{[Equation 7]}$$

It has recently been recommended to calculate ADC using at least 2 *b* values > 100 s/mm^2 to avoid the perfusion effects. In this case, equations [5] and [7] become equivalent and the apparent diffusion coefficient equals the pure diffusion coefficient.

DWI performed with a b-value of 0 s/mm^2 corresponds to a T2-weighted sequence because S_0 is proportional to exp (-TE/T2) (78). Thus, diffusion images have a T2 contamination and regions/structures with a long T2 may have an artificial signal enhancement known as

the T2 shine-through artifact. This can be overcome by using exponential images that are simply the diffusion image divided by the b = 0 image or by viewing the ADC map whose contrast represents the calculated ADC.

DWI has been used to assess liver fibrosis and inflammation (79 - 86). In fact, liver fibrosis is characterized by the accumulation of collagen, proteoglycans and other macromolecules in the extracellular matrix as a consequence of chronic injury and water molecules are hence expected to have restricted diffusion. Several studies reported that ADC was lower in cirrhotic than in non-cirrhotic livers and that it could be used to differentiate severe from mild stages of fibrosis. However, ADC was not reliable in distinguishing F0 from F1 and F1 from F2 fibrosis stages (80, 85, 86). Furthermore, one experimental and two clinical studies, the latter using IVIM, have reported that the decrease in ADC could be due instead to specific decreases in liver perfusion, which occur with increasing liver fibrosis (82, 83, 87).

Only few studies addressed the influence of increasing inflammation grades in ADC measurements and with conflicting results. Taouli et al (81) found that patients with liver inflammation grades ≥ 1 and ≥ 2 had significantly lower ADCs when compared to patients without inflammation or with inflammation ≤ 1, respectively, and that ADC had a significant inverse correlation with the inflammation grade ($r = -0.543$, $P = 0.0001$). However, Bonekamp et al (85) only reported a very weak correlation between inflammation and ADC ($r = -0.23$, $P = 0.03$) and no significant independent influence for inflammation on the ADC.

These diverging results and the scarcity of IVIM studies have opened the door to new discoveries in the relationship between diffusion/perfusion parameters and other parenchymal changes besides fibrosis, such as steatosis and inflammation, in patients with

chronic liver diseases.

e. Magnetic Resonance Elastography of the Liver (MRE)

MRE was first described in 1955 and along with the initial work in the 1990s this technique has now become very useful in the assessment of liver fibrosis (88). MR-based elastography uses a harmonic mechanical vibration of low frequency (typically between 50 to 80 Hz) induced by an external transducer, to obtain information about the mechanical properties of the liver. This excitation generates compressional waves in the liver parenchyma and shear waves are obtained by mode conversion at tissue interfaces. Sinusoidal motion-encoding gradients at the same frequency as the vibration frequency are applied during image acquisition. The resulting phase-contrast images are processed with an inversion algorithm to generate viscoelastic maps or the elasticity can be calculated from the wave speed as done with ultrasound elastography (76, 88, 89). Usually, the viscoelastic properties at MRE are based upon spatial derivatives of the measured displacement fields and not on the shear wave speed. The shear properties of an organ, referred to as the shear modulus (|G*|, kPa), calculated by demodulation and local inversion of the linear viscoelastic 3D wave equation, are best described as a complex number composed of a real part, the storage modulus (G', kPa) and an imaginary part, the loss modulus (G'', kPa) (90). The former is determined by the elastic properties (return of the organ to the initial position), whereas the latter is associated with the viscous properties of the organ (tissue friction and attenuation of waves). Thus, G' and G'' are distinct from one another and may respond differently with respect to the underlying pathology.

The complex shear modulus measured by MRE is not directly interchangeable with the Young's modulus (E) measured with transient elastography, as explained by the following equation (91 - 93):

$$E = 2\,(1+\sigma) \times \rho\,(\lambda \times \Upsilon)^2 \qquad \text{[Equation 8]}$$

Where E is the Young's modulus, σ the Poisson's Ratio, ρ the density, λ the wavelength and ϒ the wave frequency. The Poisson's ratio equals 0.5 in incompressible organs such as the liver, and the second part of the equation equals μ, the shear modulus. Therefore, equation [8] can be further simplified as follows:

$$E = 3\,\mu \qquad \text{[Equation 9]}$$

Where the Young's modulus measured at ultrasound equals 3 times the shear modulus measured at MRE. This unflawed relationship only happens in the perfect elastic material that conserves its volume after the removal of the stressful agent. However, tissues are not perfectly elastic but viscoelastic (90, 92).

The complex-valued shear modulus can also be converted into the wave number (k) with equation [10] (Fig. 42) (94).

$$G^* = \rho \times \omega^2 / k^2 \qquad \text{[Equation 10]}$$

Where G* is the complex shear modulus, ρ the density of the organ, ω the circular frequency and k the wave number (or wave vector). The wave number is a complex number composed of a real part, propagation coefficient β (mm^{-1}) and an imaginary part, attenuation coefficient α (mm^{-1}).

The propagation coefficient β is inversely related to the wavelength (λ), as described in the following equation:

$\beta = 2\,\pi / \lambda$ [Equation 11]

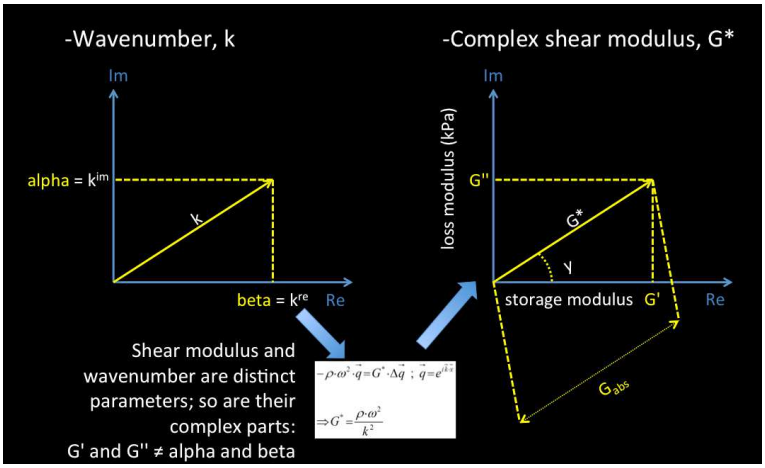

Figure 42. The wave number (k) and the Shear Modulus (G*) are complex numbers consisting of real and imaginary parts. Equation adapted from [94].

This complete assessment of the viscoelastic parameters and wave-related coefficients is until now only reliably obtained with three-directional, three-dimensional (3D) MR elastography. MRE can easily be added to the standard abdominal MRI protocols and only adds a very small incremental time.

MRE was found to accurately distinguish between fibrosis stages (AUROC 0.91 - 0.99) and with a better performance compared to transient elastography alone (Table 9) or in combination with the aspartate-to-platelet ratio (95 - 98). Moreover, MRE has several advantages compared to the ultrasound-based methods. First, an acoustic window is not required and it is operator independent. Second, the whole 3-dimensional displacement vector is assessed. Third, it enables the analysis of a larger liver volume. Fourth, the generation and good propagation of compressional waves allows the evaluation of obese patients and patients with ascites (Fig. 43). Fifth, MRE can be integrated into a complete clinical liver examination and the measured parameters are not affected by the prior use of gadoxetic acid (44, 95, 99, 100). It should also be noted that with very rapid gradient echo-

based MRE sequences the presence of increased hepatic iron content is no longer a limitation for this technique (101).

Table 9. Areas Under ROC Curves With 95% Confidence Intervals for MR Elastography and Transient Elastography

	F ≥ 1	F ≥ 2	F ≥ 3	F = 4
MR elastography	0.962 (0.929–0.995)	0.994 (0.985–1.0)	0.985 (0.968–1.0)	0.998 (0.993–1.0)
Ultrasound elastography	0.803 (0.701–0.904)	0.837 (0.756–0.918)	0.906 (0.838–0.975)	0.930 (0.877–0.982)

Reproduced from [95].

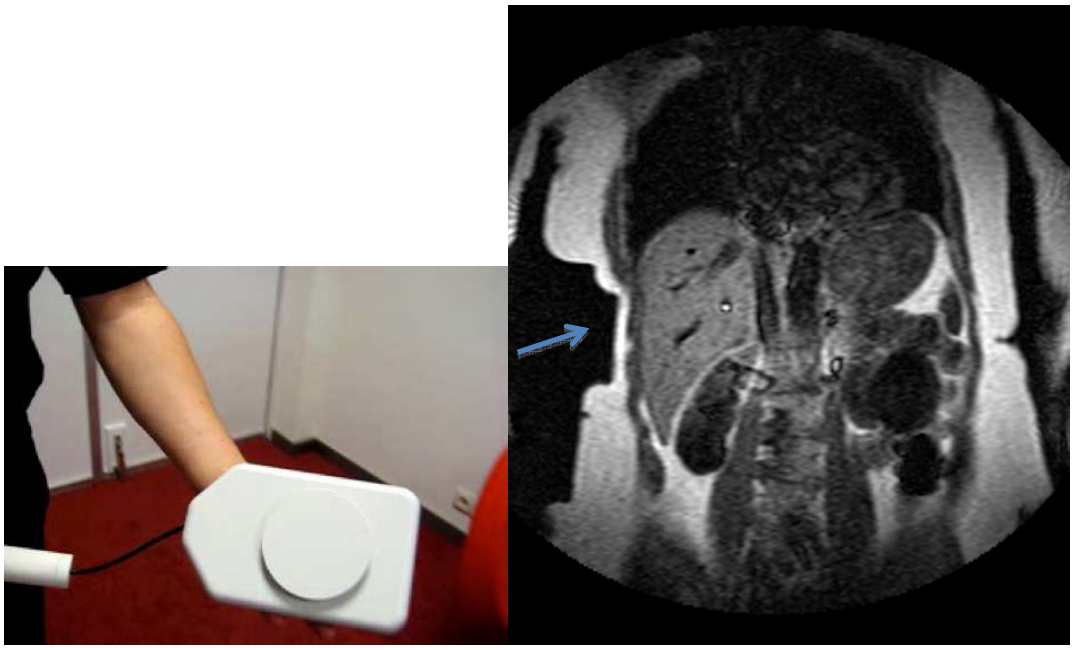

Figure 43. Left: External transducer that generates the mechanical vibration. Right: coronal MR image showing the placement of the transducer on the right flank of the patient (arrow).

Data regarding the influence of steatosis and inflammation on the measured MRE viscoelastic parameters is, nonetheless, limited and contradictory. In the two clinical studies by Huwart et al (95) and Yin et al (96) no independent effect was found for inflammation and steatosis on the measured shear modulus in patients with chronic liver diseases. However, in the clinical study by Chen et al (102) the shear modulus increased in

patients with NAFLD that presented pure inflammation but no fibrosis. In these aforementioned clinical studies, only one viscoelastic parameter was measured, thus lacking important information about the complex behavior of the shear, storage and loss moduli and the wave number. Until now only the work by Salameh et al (103) in animal models of steatosis and fibrosis started to shed a light on this matter since the authors found that viscosity related closely with steatosis while elasticity was particularly linked with inflammation and fibrosis.

Since magnetic resonance imaging techniques have been described in this section, a brief note should also be made about the hepatobiliary MR contrast agent, gadolinium ethoxybenzyl diethylenetriamine pentaacetic acid (Gd-EOB-DTPA), even though it wasn't used in the current work.

Gd-EOB-DTPA is used in routine clinical practice in many countries, including Portugal. This compound has a lipophilic residue attached to the DTPA that specifically targets the agent for uptake into the organic anion transport polypeptide (OATP1B1/3) in the sinusoidal plasma membrane of the hepatocyte. The contrast agent is excreted into the bile by the multidrug resistance protein (MRP2) (104). It is estimated that the hepatocyte uptake for the gadoxetic acid disodium is approximately 50% of the injected dose, which is ten times higher than the other available hepatospecific contrast agent (Gd-BOPTA). With this contrast agent, a delayed hepatobiliary phase, usually performed 20 min after the injection, is added to the dynamic MR imaging, (104 - 107). Several studies used Gd-EOB-DTPA to evaluate liver function and stage fibrosis, with simple or more complex pharmacokinetic analysis, and have obtained encouraging results (105-107). However, precaution is warranted in the analysis of these results, as many aspects have to be taken into account such as the lack of linear relationship between signal enhancement and the contrast concentration, factors that might influence the clearance of the contrast agent or even the known complexity of transporter proteins regulation (104).

Chapter III

Overview and Aims of the Studies

3.1. Overview and Aims of the Studies

3.1.1. Overview of the studies

All the results presented in this thesis were based on 5 clinical studies and 1 experimental animal study. Tables 10 and 11 provide the reader with a brief description of the aforementioned research.

Table 10. Overview of the clinical studies

NAME OF THE CLINICAL STUDY	NUMBER	PATHOLOGY	CHAPTER	IMAGING METHOD	STATUS
MR fat fraction mapping: a simple biomarker for liver steatosis quantification in nonalcoholic fatty liver disease patients	26 PATIENTS	NAFLD	IV	TRIPLE ECHO GRE MRI	ACCEPTED AT *ACADEMIC RADIOLOGY*
Fat deposition decreases diffusion parameters at MRI: a study in phantoms and patients with liver steatosis	9 PHANTOMS 19 PATIENTS	LIVER STEATOSIS	V	IVIM DWI	PUBLISHED AT *EUROPEAN RADIOLOGY*
The influence of liver fibrosis, inflammation and steatosis on MR diffusion and viscoelastic parameters: a study in patients with chronic liver disease	68 PATIENTS	NAFLD CHRONIC HEPATITIS B CHRONIC HEPATITIS C	VI	IVIM DWI 50 Hz MR ELASTOGRAPHY	SUBMITTED FOR PUBLICATION AT *HEPATOLOGY*
Accuracy and reproducibility of shear wave elastography to assess liver fibrosis in patients with chronic viral hepatitis and nonalcoholic fatty liver disease	48 PATIENTS	NAFLD CHRONIC HEPATITIS B CHRONIC HEPATITIS C	VII	SHEAR WAVE ELASTOGRAPHY	UNPUBLISHED WORK
Evaluation of Multifrequency MRE Wavelength Exponent in Patients with Liver Fibrosis and Inflammation: a Feasibility study	25 PATIENTS	CHRONIC HEPATITIS B CHRONIC HEPATITIS C	VII	28, 56, 84 Hz MR ELASTOGRAPHY	UNPUBLISHED WORK

Table 11. Overview of the experimental animal study

NAME OF THE EXPERIMENTAL STUDY	NUMBER	PATHOLOGY	CHAPTER	IMAGING METHOD	STATUS
Molecular Imaging of Liver Fibrosis with EP-2104R: a Feasibility Study in Rats	20 RATS	LIVER FIBROSIS	VII	Dynamic MRI	UNPUBLISHED WORK

3.1.2. Aims of the Studies

Chapter IV study: MR fat fraction mapping: a simple biomarker for liver steatosis quantification in nonalcoholic fatty liver disease patients.

The purpose of this prospective, single-center and clinical study was to assess the performance, cut-off values, post-processing time, and intra- and interobserver agreement of a simple MR-based mapping technique to quantify liver fat in the daily clinical setting.

Chapter V study: Fat deposition decreases diffusion parameters at MRI: a study in phantoms and patients with liver steatosis.

The objective of this study was to estimate the effect of fat deposition on the MR-derived apparent and pure diffusion coefficients, in lipid-based phantoms and patients with pure liver steatosis, as proven by histopathology.

Chapter VI study: The influence of liver fibrosis, inflammation and steatosis on MR diffusion and viscoelastic parameters: a study in patients with chronic liver disease.

In this prospective and single-center clinical study we investigated the influence of liver fibrosis, inflammation and steatosis on the measured MR viscoelastic and intravoxel incoherent motion parameters.

Chapter VII experimental study: Molecular imaging of liver fibrosis with EP-2104R: a feasibility study in rats.

In this experimental and feasibility study a fibrin-targeted MR contrast agent, the EP-2104R, was evaluated in its ability to detect moderate and severe fibrosis, induced by diethylnitrosamine (DEN) in rats.

Chapter VII clinical study 1: Accuracy and reproducibility of shearwave elastography to assess liver fibrosis in patients with chronic viral hepatitis and nonalcoholic fatty liver disease.

The purpose of this prospective and single-center clinical study was to evaluate the performance of ultrasound-based shearwave elastography to detect patients with a fibrosis stage ≥ F2. Moreover, the interobserver reproducibility and the influence of inflammation and steatosis on the measured liver stiffness were assessed.

Chapter VII clinical study 2: Evaluation of multifrequency MRE wavelength exponent in patients with liver fibrosis and inflammation: a feasibility study.

In this prospective and single-center clinical study the performance of the multifrequency-derived MRE wavelength exponent was studied in patients with liver fibrosis and inflammation.

Chapter IV

MR Fat Fraction Mapping: a Simple Biomarker for Liver Steatosis Quantification in Nonalcoholic Fatty Liver Disease Patients

4.1. MR fat fraction mapping: a simple biomarker for liver steatosis quantification in nonalcoholic fatty liver disease patients

Introduction

Nonalcoholic fatty liver disease is being increasingly recognized as a disease associated to liver-related morbidity and even mortality in the western countries. Its prevalence has been rising in the past two decades to become the leading cause of chronic liver disease, being closely associated to insulin resistance and type 2 diabetes (1, 3). This chronic liver disease includes not only bland steatosis but also steatohepatitis, which can progress to fibrosis, cirrhosis and ultimately hepatocellular carcinoma (3). Although early stages of liver steatosis may be reversible, patients can progress to nonalcoholic steatohepatitis even without any proven inflammation or cell injury (108 - 111). Liver biopsy is the current gold standard for diagnosing nonalcoholic fatty liver disease and quantifying liver fat. However, its invasive nature limits the use for screening or follow-up of nonalcoholic fatty liver disease patients (28). Alternative noninvasive imaging methods, such as magnetic resonance spectroscopy and multiecho ($\geq$ 6 echos) gradient-echo imaging with or without fat spectral modeling, have been used to accurately quantify liver fat (67, 112 - 115). However, they are time-consuming and require the use of extensive logarithmic calculations. Yokoo et al (112 - 113) have recently found no significant differences between triple echo gradient-echo imaging and the more complex methods for fat quantification. Therefore, the purpose of our study was to (1) assess the performance and specific cut-off value of a simple MR-based mapping technique for liver fat quantification at 1.5-T in patients at risk for nonalcoholic fatty liver disease, (2) quantify the time it can add to routine clinical practice abdominal protocols and (3) assess its intra- and

interobserver reproducibility.

Materials and methods

Study design and patients

This prospective, single-center study was approved by the review board at our institution and written informed consent was obtained for all patients. Between May 2010 and June 2011 a screening program was initiated at the Department of Endocrinology, using the following inclusion criteria: age 18 years and older, overweight with type 2 diabetes, at risk for nonalcoholic fatty liver disease, and absence of a clinical history of hepatitis, cirrhosis or hemochromatosis. A total of 32 patients were initially included in the study protocol which consisted of liver MR imaging at 1.5-T (Magnetom Symphony, Siemens Healthcare, Erlangen, Germany), using a four element surface coil, performing a triple echo gradient-echo T1-weighted MR imaging, from which the fat fraction mapping was processed, and ^{1}H magnetic resonance spectroscopy, used as the reference standard. Six patients were excluded for the following reasons: 2 patients due to technical failure during the magnetic resonance spectroscopy acquisition, 2 had uninterpretable spectra and 2 missed the scheduled MR imaging. The final study population consisted of 26 patients, 6 men and 20 women, with a mean age of 47 years (range, 28 - 70 for women; 25 - 55 years for men). The mean body mass index (BMI) was 36.2 kg/m^2 (range, 25 - 44 kg/m^2 for women; 33 - 48 kg/m^2 for men).

Magnetic resonance imaging

^{1}H magnetic resonance spectroscopy (MRS)

Single-voxel liver spectroscopy was performed with a 30 mm x 30 mm x 30 mm voxel (27 mL). Spectra were acquired with the use of point-resolved spectroscopy sequence (PRESS) during free breathing. Water suppression was not performed. To minimize T1 effects, repetition time was set at 3,000 ms. To correct for T2 effects, 5 average-spectra were collected at echo times 20, 30, 40, 50, 60 and 80 ms. Other parameters were receiver bandwith 2,000-Hz and 2,048 point spectral resolution. Automated optimization of gradient shimming was followed by manual adjustment of the central frequency, and spectra were used only if full width at half maximum water peak was 40 Hz or less. The total acquisition time was 3 min 6 s. A region of interest containing a tissue volume of 27 mL was placed in one segment of the right liver at least 10 mm from the edge of the liver, avoiding vessels or focal lesions, by a radiologist with 5-year experience in MR abdominal imaging. The ^{1}H magnetic resonance spectroscopy data was analyzed with the spectroscopic analysis package jMRUI (A. van den Boogaart, Catholic University, Leuven, Belgium). We measured the water peak (H_2O) at 4.7 ppm and the methylene peak (CH_2) at 1.3 ppm (116). T2 relaxation for water and methylene were determined from their integral values, at each echo time, by using a standard least-squares fitting algorithm with the following equation (115):

$$A(t)=A_0.e^{(-t/T2)} \qquad \text{[Equation 12]}$$

where A is the integral value at time t and A_0 is the integral value at time 0.

The peak areas of water and methylene corrected for T2 effects ($A_{0\ H2O}$ and $A_{0\ CH2}$) were

used to calculate liver fat fraction with the following equation (115):

$$\% FF = 100.\ A_{0\ CH2}/(A_{0\ CH2}+A_{0\ H2O}) \quad \text{[Equation 13]}$$

We used the 5.56% value proposed by Szczepaniak et al (67), as a threshold for the upper normal limit of liver fat. Time required for post-processing the magnetic resonance spectroscopy data was registered in each patient.

Fat fraction mapping (FFM)

A T1-weighted 2D triple echo gradient-echo sequence was initially acquired with a repetition time/echo time 164/4.6 ms (In $Phase_{1,}$ IP_1), 7.27 ms (Opposed Phase, OP), 9.98 ms (In $Phase_{2,}$ IP_2), matrix 192 x 256 pixels, 390-mm field of view (providing a pixel size of 2.0 x 1.5 mm), slice thickness 6 mm and 20° flip angle to correct for the T1-weighting effect. The acquisition time was 35 s. The final liver fat fraction mapping images were acquired on an automated pixel-by-pixel basis and computed in a post-processing workstation (Leonardo, Siemens Healthcare, Erlangen, Germany) using its basic mathematical functions as follows: 1) Images representing the IP signal intensity (SI) were corrected for T2* decay (SI_{IPco}) using the arithmetic mean function, where $SI_{IPco} = (IP_1 + IP_2)/2$; 2) OP images ($SI_{OP}$) were subtracted from the previously obtained SI_{IPco} images ($SI_{IPco} - SI_{OP}$); 3) The final fat fraction mapping images were obtained by dividing the ($SI_{IPco} - SI_{OP}$) images by SI_{IPco} images, and applying a scaling factor of 50%, as previously reported (117). A circular region of interest of 2 - 3 cm^2 was manually placed by a radiologist blinded to spectroscopy results at the right liver lobe, matching the anatomical location of the spectroscopic region of interest and avoiding vessels or focal lesions. The region of interest drawn in the liver mapping provided an immediate percentage result of

the fat content in that area (Figs. 44, 45). A similar volume-matched region of interest was placed in the spleen, to serve as internal reference for technical consistency. All FFM were repeated 1 week later to assess intraobserver reproducibility by a radiologist with 5-year experience in MR abdominal imaging. Ten cases were randomly selected to assess interobserver reproducibility, which was performed by one radiologist with 2-year experience in MR abdominal imaging. The latter was previously taught to post-process the IP/OP images in order to obtain the fat fraction mapping in half an hour Time required for post-processing the FFM was registered for each patient.

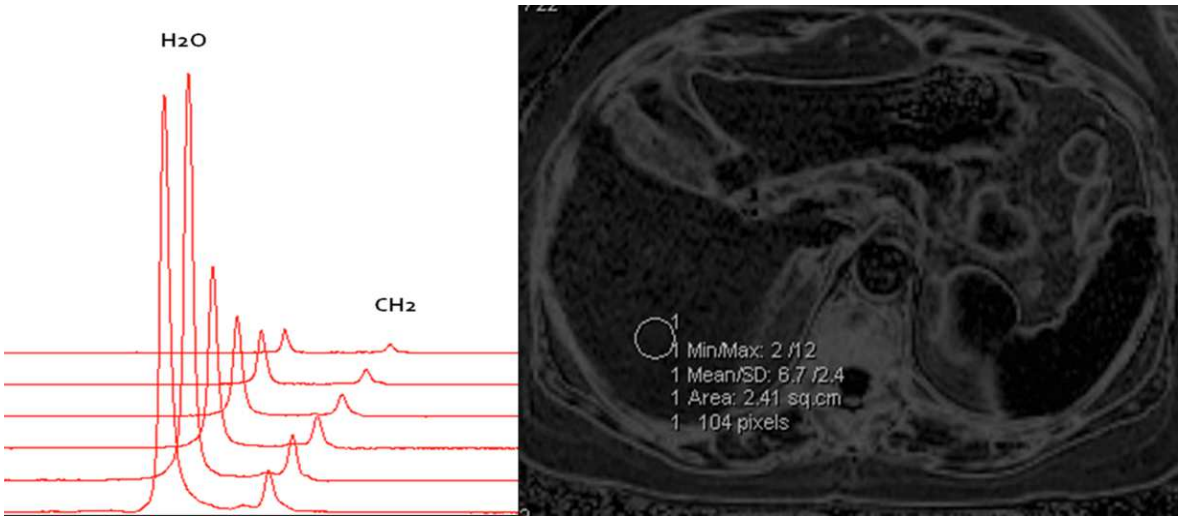

Figure 44. Left: ^{1}**H magnetic resonance spectra.** Liver fat content was 5.7 %. **Right: Liver fat fraction mapping of a 67-year old patient with type 2 diabetes.** Region of interest (1) positioned in the liver directly provides the respective fat fraction value of 6.7 %. Liver signal is only slightly more intense compared to the spleen (internal reference standard).

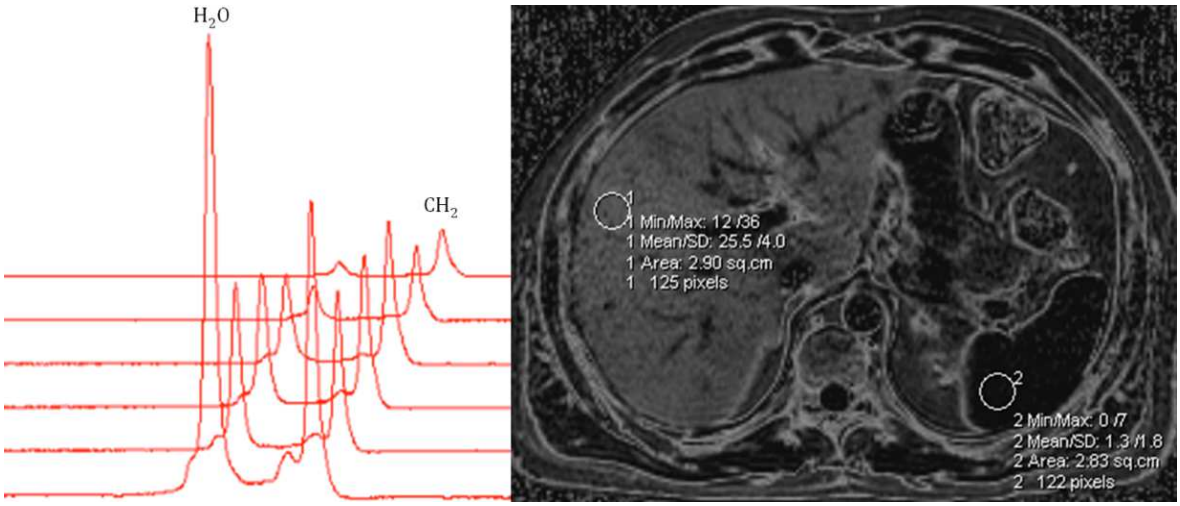

Figure 45. Left: ^{1}H magnetic resonance spectra. Liver fat content was 26.7 %. **Right: Liver fat fraction mapping of a 40-year old patient with type 2 diabetes and severe steatosis.** Liver fat is clearly visible on the mapping, as the liver is very hyperintense compared to the spleen. Measurements in the liver (1) and spleen (2) provide fat fraction within regions of interest (25.5 % and 1.3 %, respectively).

Statistical Analysis

In this prospective study an *a priori* power analysis was performed in order to obtain a significance of 0.05 and a power of at least 80%. Previous reports in the literature for the prevalence of liver steatosis and mean liver fat content in a similar population were used for that purpose (114, 118). A minimum number of 21 patients had to be included in our study.

The correlation between the fat fraction mapping measurements and magnetic resonance spectroscopy was assessed using the non-parametric Spearman rank correlation coefficient (r). The evaluation of bias was done using the 95% limit-of-agreement method developed by Bland and Altman (119), in which the difference between fat content measured by two methods is plotted against their mean. The performance of the fat fraction mapping was assessed by plotting the true positive rate in function of the false positive rate for different cut-off points, which allowed calculating the area under the curve of a receiver operating

characteristic curve and determining the cut-off value for the technique. The difference in acquisition and post-processing times between both methods was assessed using the non-parametric Wilcoxon test. Intra- and interobserver reproducibility was calculated using intraclass correlation coefficients. A *P* value ≤ 0.05 was considered statistically significant. Statistical analysis was performed with the MedCalc software (MedCalc, Mariakerke, Belgium).

Results

In this patient cohort a mean fat percentage of 11.7% (range, 2 - 35.4%) was obtained using the FFM technique corresponding to 9.8% (range, 0.8 - 30%) using MRS (Table 12). A strong correlation was found between both methods (r = 0.89, *P* < 0.0001). On the Bland-Altman plot 25 of the 26 fat measurements were within ± 4.2% of the mean difference of both methods (2%) (Fig. 46). Using the reference threshold proposed by Szczepaniak et al (67) for MRS, we found that a cut-off value of 6.9% for FFM provided an accurate diagnosis of fat content with 93% sensitivity and 100% specificity. The area under the curve for fat fraction mapping was 0.99. The spleen was used as our internal reference and all spleen measurements had a fat content ≤ 1.5% (Fig. 45). Median post-processing and reading time was 5 minutes (range, 5 - 15 min) for FFM and 35 minutes (range, 30 - 50 min) for MRS (*P* < 0.0001). Intraclass correlation coefficients for intra- and interobserver agreement were 0.98 (95% CI, 0.96 - 0.99) and 0.99 (95% CI, 0.97 - 0.99), respectively.

Table 12. Fat fraction measurements with FFM and MRS in the 26 patients

FFM (%)	MRS (%)
4.8	1.2
2.8	0.8
2.6	0.8
27.4	28.6
4.5	1.2
35.4	30
15.7	14.2
2.0	1.0
6.7	5.7
12.0	7.0
15.9	15
10.8	7.3
3.0	1.0
20.8	21.7
25.5	26.7
12.6	10.8
6.9	3.1
2.5	1.0
5.3	1.3
11.4	10.3
16.8	20.5
6.7	1.6
2.2	0.8
6.8	4.4
31.7	29.3
12.0	11.0

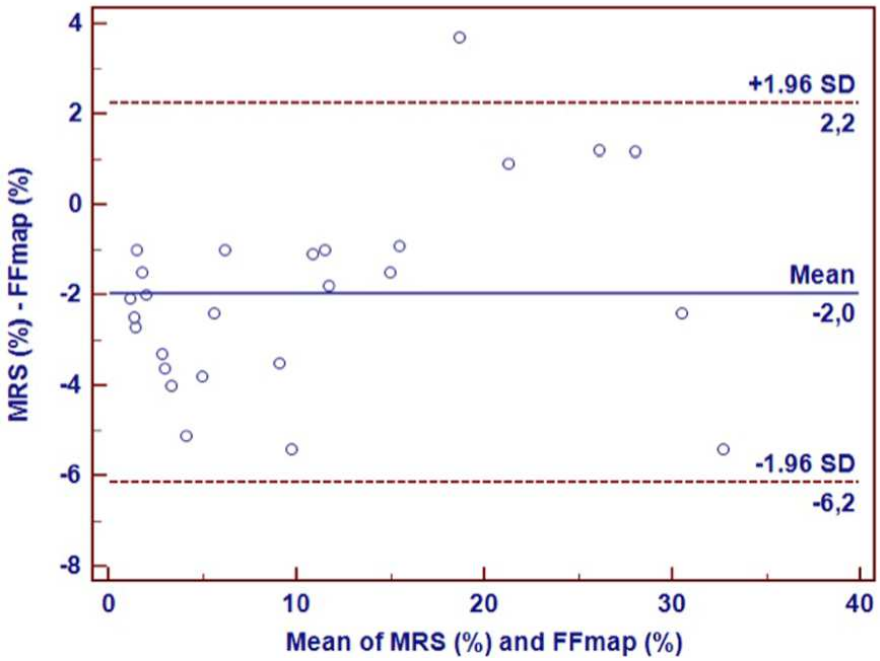

Figure 46. Bland-Altman plot representing the difference between liver fat fraction (%) estimated with magnetic resonance spectroscopy and mapping (measured by observer 1 at one time point) plotted against their means. Only one fat fraction measurement wasn't within the ± 1.96 SD (4.2 %) of the mean for both methods, but all fat fraction measurements stayed within the upper maximum and lower minimum 95 % limit of agreement. SD = Standard Deviation.

Discussion

In this prospective, single-center study we have assess the performance, post-processing time, intra- and interobserver agreement of an MR-based mapping for liver fat quantification using a triple-echo gradient-echo sequence for T2* correction. Our results show that this mapping can accurately provide liver fat quantification within a short post-processing time with excellent intra- and interobserver agreement. The cut-off value of 6.9% for the mapping method was found to have the best sensitivity and specificity to diagnose patients with and without liver fat deposition. Histological assessment of liver biopsy is considered the reference standard for the diagnosis of steatosis but its use for screening or follow-up studies remains impractical due to its invasive nature. Moreover, it is subjected to important sampling errors since liver steatosis is a heterogeneous process often associated with spared areas that may be related, among other reasons, to vascular abnormalities (120). The noninvasive quantification of liver fat has been made possible by the use of magnetic resonance imaging with either ^{1}H magnetic resonance spectroscopy or multiecho gradient-echo sequences. However, spectroscopy has limited spatial coverage and requires substantial expertise for its implementation and analysis, and the multiecho sequences ($\geq$ 6 echos) require the use of equations with increasing complexity and additional analysis software to measure fat content (25, 53, 112). Recently good agreement of fat fraction measurements between MRS and triple echo gradient-echo imaging over a wide range of fat content was reported (112). The FFM technique used in our study also showed very good correlation with MRS, although the correlation coefficient was lower than previous reports ($\approx$ 0.98) (119). This may probably be explained by two factors: first, due to technical limitations at 1.5-T we assumed a simplified fat spectrum consisting of a single methylene peak at 1.3 ppm (116), while gradient-echo magnetic resonance imaging

includes signals from all fat peaks. Secondly, T2* effect was corrected assuming a linear T2* decay between the two IP echoes, as previously observed by Guiu et al (117). However, to insure that no bias from T2* decay influenced our measurements we used the first two closely spaced in-phase echo times to obtain the in-phase corrected signal. These two in-phase echo times have superior signal-to-noise ratio and are less influenced by fat-fat interference. We are aware that the FFM technique does not solve the problem of fat-water ambiguity since subcutaneous fat will show values of 8 - 12%, when the real fat fraction is obtained subtracting this value from 100%. However, liver fat fractions higher than 50% are very uncommon in the liver parenchyma (67, 112, 114, 118). The highest fat fraction measured in the present study was 35.4%. When performing visual assessment of the map, liver fat is hyperintense compared to the spleen, our internal reference. The spleen does not contain visible fat on MRI except in cases of lipid storage disorders and after administration of intravenous fat emulsions (117, 121). Since splenic measurements obtained for all patients were consistently $\leq$ 1.5%, it allowed us to conclude about the good reproducibility of the technique.

The Bland-Altman plot showed that the fat fraction measurements for all patients, except one, were within ± 4.2% of the mean difference of both methods. This is a fairly reasonable value considering that quantification of liver fat by visual assessment on pathological specimens has broader grading limits (4). The median time spent for acquisition and post-processing of ^{1}H MRS in our study was ≈ 38 min, which can at least be partially explained by the lack of fully automated spectral analysis software. However, the mean time spent to produce and analyze FFM was only 5 min 35 s, which makes the technique a realistic choice to incorporate in a busy clinical setting. Compared to previous studies that only assessed the agreement of the mapping technique with respect to an imaging gold standard (114, 117), we have determined its cut-off value and intra- and

interobserver reproducibility. Using 6.9% as a cut-off value can accurately distinguish patients with and without liver steatosis. Furthermore, in our work excellent intra- and interobserver reproducibility were observed and we believe that this is an additional reason to apply FFM as a potential biomarker for liver steatosis quantification.

The clinical relevance of FFM must be considered especially in the setting of longitudinal population-based epidemiologic studies, since recent studies have reported a 5% prevalence of fatty liver in the general pediatric population, 38% in obese children and 48 % in children having type 2 diabetes (122).

Our study has limitations: first, steatosis quantification was not confirmed by histology since performing liver biopsy in asymptomatic patients is not ethically justified, and may be under representative since only 1/50000 of the organ is actually analyzed (4); second, the absence of liver iron overload was not histologically verified but it must be stressed that the present series was composed of patients only at risk for nonalcoholic fatty liver disease, without clinical or biological evidence of iron overload; third, we were not able to test the longitudinal reproducibility of FFM since each patient was submitted to a single MR session for each quantification technique.

In conclusion, FFM is a simple and accurate technique for liver steatosis quantification. Since it can be performed in a short time frame it can potentially be included in routine liver studies dealing with this clinical problem, especially in the setting of large longitudinal population-based epidemiologic studies.

Chapter V

Fat Deposition Decreases Diffusion Parameters at MRI: a Study in Phantoms and Patients with Liver Steatosis

5.1.Fat deposition decreases diffusion parameters at MRI: a study in phantoms and patients with liver steatosis

Introduction

Chronic liver diseases are frequent causes of morbidity and mortality in the Western countries. In a recent screening study performed in a general population older than 45 years, liver fibrosis related to unsuspected chronic liver disease was detected in 7.5% of the subjects and cirrhosis in about 1% (123). The most frequent causes of chronic liver diseases encountered were nonalcoholic fatty liver disease (NAFLD), alcoholic liver disease and viral hepatitis C and B (123). Among these, nonalcoholic fatty liver disease is a major healthcare problem since excessive liver fat is detected in one third of the United States adult population (67, 122).

Recently, various imaging methods, including diffusion-weighted magnetic resonance imaging, have emerged as potential biomarkers for chronic liver disease (67, 97). Prior studies have shown that chronic liver diseases are associated with a decrease of the diffusion coefficients. This has been related to progressive fibrosis, inflammation and decreased perfusion (81, 82, 85, 87, 124). Liver steatosis is also frequently observed in patients with liver fibrosis, especially in patients with nonalcoholic and alcoholic liver diseases and viral hepatitis C and B (53, 108).

However, only few and conflicting data are available regarding the influence of liver steatosis on the diffusion parameters. In most reported studies liver steatosis is considered not to restrict diffusion (85, 115, 125). Two recent studies performed in patients and rats suggested a relationship between steatosis and diffusion (126, 127). However, because no liver biopsies were obtained in the patient study, the effect of confounding factors such as fibrosis and inflammation on the diffusion measurements could not be assessed. In the

animal study, biopsies were obtained, but a multivariate analysis of the influence of steatosis, inflammation and fibrosis on the diffusion measurements was not performed. Therefore, the purpose of our study was to assess the effect of fat deposition on the MRI diffusion coefficients, in lipid emulsion-based phantoms and in patients with normal liver and with isolated liver steatosis, without any other confounding factors, as confirmed by histopathology.

Material and methods

Lipid emulsion-based phantom study

The phantoms consisted of 50 mL tubes containing a constant amount of 5 mL of gelatin, used as a solidification agent. To obtain the various fat fractions in the phantoms, we progressively increased the added amount of a lipid emulsion of refined olive oil (16%) and soybean oil (4%) (ClinOleic 20%, Baxter, Maurepas, France) in each tube and decreased the added amount of water in parallel. The final fractions of fat in the phantoms ranged from 0 to 18% (0%, 3%, 5%, 7%, 9%, 12%, 14%, 16%, 18%). Fat droplets inside the phantoms had a mean diameter of 0.6 microns, which is similar to that of fat droplets within the hepatocyte cytoplasm (about 1 micron) (128, 129).

The phantoms were imaged using 1.5T MR (Intera, Philips Medical Systems, Best, The Netherlands) with a four-element surface coil. Diffusion-weighted magnetic resonance imaging was performed without and with a fat suppression scheme (Spectral Presaturation with Inversion Recovery), using a single-shot echo-planar acquisition and the following parameters: repetition time/echo time 305/57 ms, matrix 80 x 80 pixels, 250-mm field of view, 3 transverse slices, slice thickness 4 mm, 11 b values (0, 10, 20, 30, 40, 50, 75, 100, 150, 300 and 500 s/mm^2), 20 averages and 3 directions. The acquisition time was 3

minutes 30 seconds.

Patient study

This retrospective clinical study was approved by the review board at our institution and informed consent was waived. Patients who underwent magnetic resonance imaging for the assessment of a liver tumour, between June 2010 and March 2011, were identified for this study. Inclusion criteria were: age 18 years and older; liver MRI with a multi-b diffusion-weighted sequence; histopathological assessment of the tumour and non-tumourous liver parenchyma performed by liver biopsy or after surgical resection. Ninety-seven patients were identified based on the inclusion criteria.

The diffusion-weighted images in the patients were obtained using the same 1.5T MRI system and surface coil described above for the phantom study. The multi-b single-shot echo-planar diffusion-weighted acquisition had the following parameters: repetition time/echo time 305/57 ms, matrix 80 x 80 pixels, 320-mm field of view, 3 transverse slices, slice thickness 4 mm, 11 b values (0, 10, 20, 30, 40, 50, 75, 100, 150, 300 and 500 s/mm^2), 20 averages and 3 directions. Image acquisition was obtained with fat suppression (Spectral Presaturation with Inversion Recovery) and free breathing. The acquisition time was 3 minutes 30 seconds.

Exclusion criteria were as follows: motion artefact on the diffusion-weighted images precluding the analysis of the diffusion parameters (7 patients); liver inflammation, fibrosis, cirrhosis or iron overload at histopathological evaluation (71 patients). The final study population consisted of 19 patients, 12 women and 7 men, with a mean age of 50.7 years (range: 24 - 72 years for women; 37 - 74 years for men). The median interval between magnetic resonance imaging and biopsy (n = 16) or surgical resection (n = 3) was 14.5 days (range: 0 - 90 days).

For the patients included in the study, the non-tumourous liver biopsies were retrospectively reviewed by an experienced hepatobiliary pathologist who was unaware of imaging results. This evaluation confirmed the absence of steatosis, inflammation, fibrosis and iron (*n* = 14, normal liver) or the presence of isolated liver steatosis (n = 5), and grading was performed according to the Brunt classification (4): three patients had grade 1 steatosis (number of hepatocytes containing fat: 5 – 33%), one grade 2 (33 – 66 %) and one grade 3 (> 66%).

Image interpretation

Regions of interest were placed on the diffusion-weighted images, by one of the authors with 5-year experience in MRI, blinded to the results of histopathology. The regions of interest were placed within the center of each test phantom to avoid edge artifacts and in the right liver avoiding large vessels and focal liver lesions. The absence of a liver lesion or large vessel in the region of interest was confirmed by visually comparing the region of interest positioned on the diffusion-weighted, T1 and T2-weighted images. The mean area for the regions of interest was 4.3 ± 0.5 cm^2 in the lipid emulsion-based phantoms and 18 ± 6.8 cm^2 in patients.

The apparent diffusion coefficient was measured using a monoexponential model (130) with the following equation:

$$S_b/S_0 = \exp^{(-b\ ADC)} \qquad \text{[Equation 14]}$$

where ADC (10^{-3} mm^2/s) is the apparent diffusion coefficient, S_b the signal intensity for each *b* value and S_0 the signal intensity at b_0.

The other diffusion coefficients were measured using a bi-exponential fit (130) with the

following equation:

$$S_b/S_0 = (1\text{-}f)^{\exp(-b\,D)} + f \exp^{(-b\,(D + D^*))} \quad \text{[Equation 15]}$$

where, f (%) is the fraction of diffusion linked to microcirculation, D (10^{-3} mm^2/s) the true diffusion coefficient, and D* (10^{-3} mm^2/s) the perfusion-related diffusion coefficient.

The algorithms were implemented with purpose built software running under the ROOT environment (ROOT 5.22, CERN, Geneva, Switzerland). The reproducibility of the diffusion parameters measurements has been reported previously (131).

Statistical analysis

The results are reported as mean ± standard deviation. The correlation between the fat fraction and the diffusion coefficients for the lipid emulsion-based phantoms was calculated with Spearman correlation coefficients (r). The diffusion parameters of the patients with and without isolated liver steatosis were compared with the Mann-Whitney *U* test after Bonferroni correction. $P \leq 0.01$ was considered to indicate a statistically significant difference. Statistical analysis was performed with the MedCalc software (MedCalc, Mariakerke, Belgium).

Results

The results of the diffusion parameters measurements in the phantoms are given in table 13. The apparent and pure diffusion coefficients decreased from 2 and 2.1 x 10^{-3} mm^2/s, for a fat fraction of 0%, to 1.42 and 1.49 x 10^{-3} mm^2/s, for a fat fraction of 18%, with fat

suppression, and from 2.04 and 2.1 x 10^{-3} mm^2/s, for a fat fraction of 0%, to 0.89 and 0.88 x 10^{-3} mm^2/s, for a fat fraction of 18%, without fat suppression, respectively. A strong inverse correlation was found between fat fraction and apparent and pure diffusion coefficients, either with fat suppression (r = - 0.98, $P < 0.0001$; r = - 0.97, $P < 0.0001$, respectively) or without fat suppression (r = - 0.99, $P < 0.0001$; r = - 0.99, $P < 0.0001$, respectively). The measured perfusion fractions (1.8 ± 1% and 1 ± 0.8% with and without fat suppression, respectively) and the perfusion-related diffusion coefficients (6.7 ± 3.5 x 10^{-3} mm^2/s and 3.6 ± 2.4 x 10^{-3} mm^2/s) were almost zero.

In patients with normal liver, the pure diffusion coefficient was significantly higher than in patients with isolated liver steatosis (1.18 ± 0.09 x 10^{-3} mm^2/s versus 0.96 ± 0.16 x 10^{-3} mm^2/s, $P = 0.005$) (Figs. 47 - 49). The apparent diffusion coefficient, perfusion-related diffusion coefficient and perfusion fraction did not differ significantly between patients without and with isolated liver steatosis, but there was a small decrease trend of the apparent diffusion coefficient in patients with liver steatosis (apparent diffusion coefficient: 1.41 ± 0.14 x 10^{-3} mm^2/s versus 1.26 ± 0.25 x 10^{-3} mm^2/s, $P = 0.298$; perfusion-related diffusion coefficient: 99.9 ± 2.18 x 10^{-3} mm^2/s versus 99.6 ± 3.79 x 10^{-3} mm^2/s, $P = 0.754$; perfusion fraction: 21 ± 2% versus 23 ± 4%, $P = 0.431$, respectively).

Table 13. Apparent (ADC x 10^{-3} mm^2/s) and pure (D x 10^{-3} mm^2/s) diffusion coefficients, measured without and with fat suppression, in lipid emulsion-based phantoms, according to the fat fraction

Fat fraction (%)	0	3	5	7	9	12	14	16	18	r	*P*
ADC without fat suppression	2.04	1.81	1.69	1.57	1.39	1.15	1.10	1.09	0.89	- 0.99	< 0.0001
ADC with fat suppression	2.00	1.94	1.81	1.74	1.69	1.68	1.61	1.54	1.42	- 0.98	< 0.0001
D without fat suppression	2.1	1.84	1.74	1.60	1.42	1.17	1.11	1.09	0.88	- 0.99	< 0.0001
D with fat suppression	2.1	2.02	1.90	1.82	1.76	1.75	1.68	1.62	1.49	- 0.97	< 0.0001

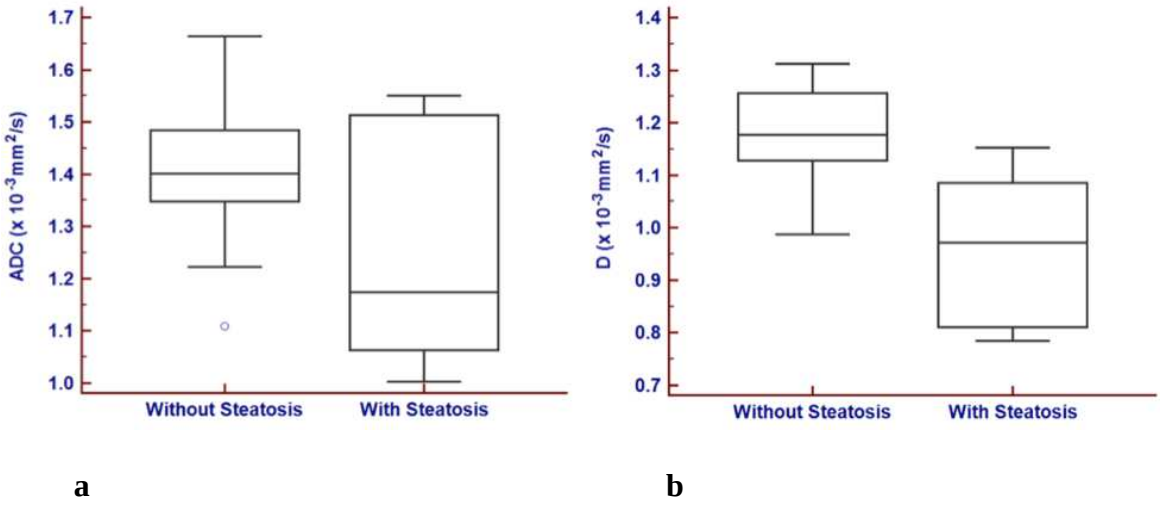

Figure 47. Box and whisker plots showing the apparent (a) and pure (b) diffusion coefficients (x 10^{-3} mm^2/s) according to the presence or absence of liver steatosis. Central box represents the values from the first to third quartiles and the middle line represents the median. The vertical line extends from the minimum to the maximum value within 1.5 times the interquartile range. Outliers are represented as individual points. No significant difference of apparent diffusion coefficient is observed between the two groups (a). The pure diffusion coefficient (b) is significantly lower in the steatotic group (P = 0.005).

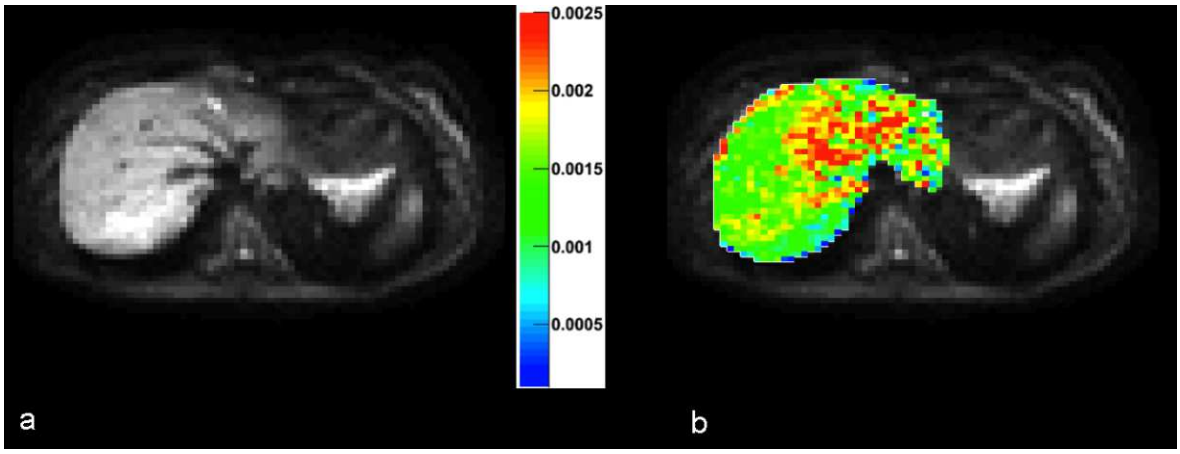

Figure 48. Left: Diffusion-weighted image at b = 10 s/mm^2. Right: the same image with a superposed parametric color map of the pure diffusion coefficient, with a scale in mm^2/s, in 68-year old woman without liver steatosis. The measured pure diffusion coefficient was 1.3 mm^2/s. The region of interest was placed in the right lobe, away from regions with apparent increase of diffusion. This apparent increase of diffusion in the left lobe may be explained by the flow in the large hepatic veins and transmitted cardiac motion.

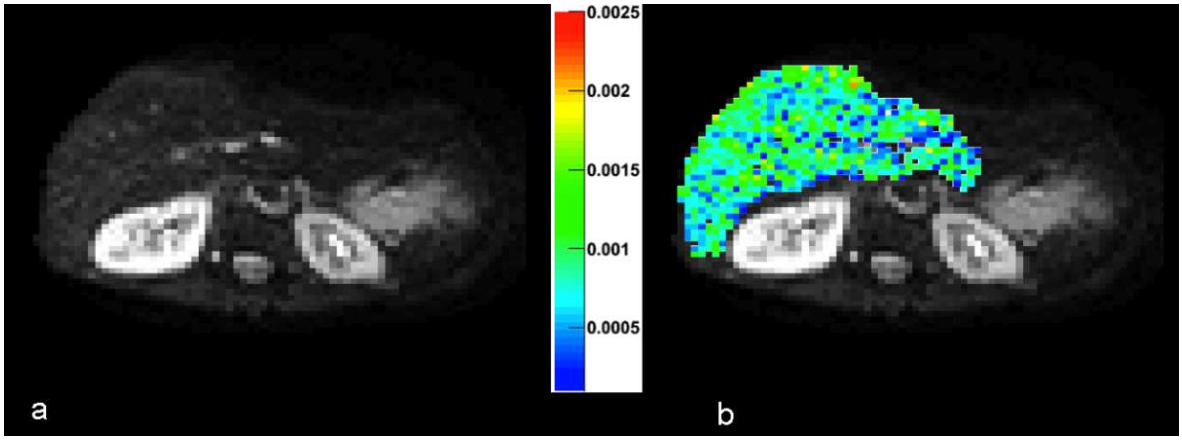

Figure 49. Left: Diffusion-weighted image at b = 10 s/mm^2. Right: the same image with a superposed parametric color map of the pure diffusion coefficient, with a scale in mm^2/s, in 52-year old woman with liver steatosis. The measured pure diffusion coefficient (0.82 mm^2/s) was lower than that observed in a patient with normal liver.

Discussion

In this study performed in lipid emulsion-based phantoms and patients with and without isolated liver steatosis, we have observed that the presence of fat droplets decreases the apparent and pure diffusion coefficients. In tissues containing both water and fat, it has been reported that slow diffusion may be explained by a restriction of water diffusion due to abundant lipids and by diffusion of mobile lipids, which is a slow phenomenon, occurring at a rate that is 100 times slower than water diffusion (132, 133). The respective influence of restricted water diffusion and slow lipid diffusion on the decrease of the diffusion parameters in steatosis is unknown. This influence will depend on the use of fat suppression. Without fat suppression, both restricted water diffusion and slow lipid diffusion may be observed, whereas with perfect fat suppression, only restricted water diffusion should be observed. Our findings in phantoms agree with these concepts, as the diffusion parameters measurements were higher with fat suppression than without. In vivo, perfect lipid signal suppression cannot be obtained, as multiple technical and biological reasons are at stake, including the fact that two of the fat spectrum peaks (olefinic acid at 5.3 ppm and glycerol at 4.2 ppm) have frequencies very close to that of the water peak (at 4.7 ppm) (116). These lipid peaks, representing 8 - 10% of the total fat spectrum, cannot be suppressed at clinical field strengths, without also suppressing the water peak. Residual fat signal on fat suppressed diffusion-weighted images may decrease the measured diffusion parameters in two ways. First, slow lipid diffusion may be observed in these fat areas. Second, residual fat signal on high b-value diffusion-weighted images, may artefactually decrease the measured diffusion parameters (134, 135). Regardless of the cause, our results show that isolated liver steatosis decreases the diffusion parameters measurements.

We observed similar results in liver steatosis and in phantoms closely mimicking this clinical condition. In contrast to the lipid phantom models previously described in the literature, containing unmixed volumes of water and mineral oil in a container, imaged with an oblique imaging plane through the boundaries of both chemical environments to obtain different concentrations of water and fat (136, 137), our phantoms consisted of lipid emulsions, with lipid droplets similar in size and concentration to the lipid inclusions in hepatocytes. Indeed, as mentioned in material and methods, the size of the lipid droplets in our phantoms (0.6 microns) was close to that of intracellular fat droplets in liver steatosis (about 1 micron). Moreover, the fat percentages in the phantoms (0 – 18%) covered a wide range of steatosis severity. It has previously been shown that the percentage of fat-containing hepatocytes is about 2.75 higher than the percentage of fat on a volume basis (138). This means that a fat percentage of 18% in the phantoms, relates to almost 50% of fat containing hepatocytes, i.e. moderate to severe steatosis according to the Brunt classification (4).

With respect to the clinical study and to the best of our knowledge, this is the first biopsy-proven study that reports the definite influence of isolated liver steatosis, with no other pathological confounding factors, on the diffusion parameters. Until now, limited and conflicting results have been published regarding the influence of steatosis on the diffusion parameters. In most studies, no significant influence was observed (85, 115, 125). Recently, an inverse correlation between the apparent diffusion coefficient and hepatic fat fraction was reported in ex-vivo rat livers by Anderson SW et al. (126) and in patients by Poyraz AK et al. (127). However, these two studies are limited by the absence of information about the specific influence of steatosis, inflammation and fibrosis on the apparent diffusion coefficients measurements. Namely, in the retrospective clinical study by Poyraz AK et al. (127), liver biopsy was not obtained. In the ex-vivo study by

Anderson SW et al. (126), histopathology was available, but a multivariate analysis of the influence of steatosis, inflammation and fibrosis on the diffusion measurements was not performed.

Moreover, except for the study of Lee JT et al. (125), only the apparent diffusion coefficient was measured in these previous works. The apparent diffusion coefficient, a compound parameter that includes influences from pure molecular diffusion and perfusion-related diffusion, may be less sensitive than the individual diffusion parameters to changes induced by steatosis or fibrosis, as shown in our study and that of Luciani et al. (82). In nonalcoholic fatty liver disease, liver perfusion is decreased because of reduced sinusoidal volume (139). However, we did not observe a decrease of the perfusion-related diffusion parameters in patients with liver steatosis. Several factors may explain this apparent discrepancy such as, the small number of patients with isolated liver steatosis in our study, and the known difficulty of obtaining reliable results for the perfusion-related diffusion parameters (140). Moreover, decreased perfusion has mainly been observed in steatohepatitis rather than in isolated steatosis, because sinusoidal compression and distortion in steatohepatitis are caused not only by fat deposits within hepatocytes, but also by hepatocyte hydropic ballooning, fibrosis of the space of Disse and leukocyte adhesion to the sinusoidal endothelium (139, 141).

Diffusion-weighted magnetic resonance imaging is not used to quantify liver fat, since other methods, such as proton spectroscopy and multi-echo gradient-echo imaging, are accurate for that purpose (67, 112). However, our results show that liver steatosis may decrease the measured diffusion parameters in chronic liver diseases. In addition to liver inflammation and decreased liver perfusion, which have previously been shown to decrease the diffusion parameters (81, 85, 87, 142), liver steatosis is hence a confounding factor when trying to stage liver fibrosis at diffusion-weighted MRI. Concomitant liver

steatosis and fibrosis are often observed in chronic liver diseases, not only in nonalcoholic and alcoholic steatohepatitis, but also in chronic viral hepatitis (143).

In our study, the decrease of diffusion parameters in patients with liver steatosis concerned the true diffusion coefficient, but not the apparent diffusion coefficient, calculated with a monoexponential approach using 11 b values, ranging from 0 to 500 s/mm^2. It has been recently recommended to calculate the apparent diffusion coefficient with a monoexponential approach using at least 2 b values > 100 s/mm^2 to avoid the perfusion effect on the measured value (75). In this case, the apparent diffusion coefficient equals the true diffusion coefficient and liver steatosis also decreases the apparent diffusion coefficient calculated with this method.

Our study has limitations. Firstly, the number of included patients was small, because we excluded all patients with combined fat infiltration, iron overload, fibrosis and/or inflammation. The small cohort of patients with isolated liver steatosis might explain why we have not found a significant difference in the apparent diffusion coefficient between the two subgroups of patients, since this composite parameter is less sensitive than the pure diffusion coefficient. Because of the small number of patients, we did not correlate the diffusion parameters with liver fat fractions. However, our phantom study suggests that increasing fat fraction correlates with decreasing diffusion. A larger prospective study in patients with isolated liver steatosis is needed to confirm these findings.

Secondly, we acquired free-breathing echo-planar diffusion-weighted imaging and physiological motion is always a concern when studying the microscopic displacement of protons. However, good reproducibility of the diffusion parameters was reported with free breathing or navigator-echo triggered sequences (75, 83).

In conclusion, our results show that the presence of fat droplets decreases the diffusion parameters and suggests that steatosis may have confounding effects when measuring the

diffusion parameters at MRI.

Chapter VI

The Influence of Liver Fibrosis, Inflammation and Steatosis on MR Diffusion and Viscoelastic Parameters: a Study in Patients with Chronic Liver Disease

6.1. The influence of liver fibrosis, inflammation and steatosis on the MR diffusion and viscoelastic parameters: a prospective study in patients with chronic liver disease

Introduction

Chronic liver diseases such as viral hepatitis and nonalcoholic fatty liver disease, are a major cause of morbidity and mortality worldwide. Their prevalence has been rising in the last decade mostly due to nonalcoholic fatty liver disease that increases along with metabolic conditions and obesity. Furthermore, the latter can also be associated with other causes of chronic liver diseases in the same patient (1, 144). Liver biopsy is commonly used as the reference standard to evaluate fibrosis and the associated inflammation and steatosis, but it has inherent risks, poor reproducibility and a low performance for intermediary stages of fibrosis (145). Moreover, from a patient's perspective the prospect of undergoing repeated liver biopsies for follow-up is daunting and highly inconvenient.

Several noninvasive imaging methods such as ultrasound-based transient elastography, magnetic resonance elastography and diffusion-weighted imaging are used to stage fibrosis, and assess inflammation and steatosis (47, 48, 81, 82, 85, 95 - 97, 102, 103, 146, 147). However, there is still a significant debate and conflicting data regarding the influence of the necroinflammatory activity and steatosis on the measured viscoelastic and diffusion parameters in patients with liver fibrosis. In three previous studies no independent effect was found for inflammation and steatosis on the measured liver stiffness and apparent diffusion coefficient, in patients with chronic liver disease (85, 95, 96). However, other authors reported that the presence of edema and inflammation, in acute hepatitis, increases liver stiffness and restricts diffusion (47, 48, 81). The same effect was found on viscoelastic and diffusion parameters for cholestasis and steatosis (23, 49, 146 - 149). Therefore, the purpose of our study is to assess the independent influence

of liver fibrosis, inflammation and steatosis on the measured MR diffusion and viscoelastic parameters. To the best of our knowledge this is the first study to evaluate this effect on both MR-derived parameters in the same cohort of patients.

Material and methods

Patients and study protocol

The review board at our institution approved this single-center and prospective clinical study and informed consent was obtained for all patients. From November 2010 through October 2012, all consecutive patients 18 years or older, seen at the department of hepatology with untreated viral hepatitis and nonalcoholic fatty liver disease and scheduled for liver biopsy were enrolled in this study. A total of 82 patients were initially included in the study protocol which consisted of liver MR imaging at 1.5-T (Intera, Philips Medical Systems, Best, The Netherlands), using a four element surface coil, and performing intravoxel incoherent motion diffusion-weighted imaging and monofrequency magnetic resonance elastography. Fourteen patients were afterwards excluded for the following reasons: in 2 patients a metallic implant contraindicated the study; in 2 patients MR imaging was stopped because of claustrophobia; in 9 patients the presence of imaging artefacts precluded the analysis of the MR parameters and 1 patient was pregnant at the time of the scheduled MR imaging. The final study population consisted of 68 patients, 21 women and 47 men, with a mean age of 41 years for women (range: 29 - 68 years) and 47 years for men (range: 22 - 71 years). Thirty-nine patients had viral hepatitis C, 20 had viral hepatitis B and 9 had nonalcoholic fatty liver disease. An expert hepatobiliary pathologist who was unaware of imaging results performed the histopathologic analysis of all liver specimens. Fibrosis and inflammation were documented according to the

METAVIR or NAS scoring systems (27, 150, 151) and steatosis was graded according to the Brunt classification (4) as explained in Chapter II, sections 2.2.1. and 2.2.2.. The mean interval between biopsy and MR imaging was 24 days (range: 0 - 60 days).

MR Imaging and post-processing analysis

Diffusion-weighted imaging:

Multi-b single-shot echo-planar diffusion-weighted imaging was acquired with a previously published protocol (152). Briefly, the following parameters were used: repetition time/echo time 305/57 ms, 320-mm field of view, matrix 80 × 80 pixels, 4 mm^3 isotropic voxels, 3 transverse slices, slice thickness 4 mm, 11 b values (0, 10, 20, 30, 40, 50, 75, 100, 150, 300 and 500 s/mm^2), 20 averages and 3 directions. Image acquisition was obtained with fat suppression (Spectral Presaturation with Inversion Recovery) and free breathing. The acquisition time was 3 min 28 s.

Regions of interest were placed in the liver on the diffusion-weighted images avoiding large vessels and focal liver lesions (which was confirmed by visually comparing the region of interest positioned on the diffusion, T1 and T2-weighted images), by one of the authors with 7-year experience in MR imaging, blinded to the results of the histopathologic analysis. The ROIs were copied on the DW images, and ROI location was checked over all b images. The ROIs were then copied on the DW parametric maps, and mean parameter values were obtained in each ROI. Mean area for the regions of interest was 18 ± 6.8 cm^2. The signal acquired from all the *b* values was used to generate the maps on a pixel-by-pixel basis for the intravoxel incoherent motion diffusion-weighted imaging parameters, using the ROOT environment (ROOT 5.22, CERN, Geneva, Switzerland).

All the parameters were measured by applying a segmented bi-exponential fit (130) with the following equation:

$$S_b/S_0 = (1\text{-}f)^{\exp(-b\,D)} + f \exp^{(-b\,(D + D^*))} \qquad \text{[Equation 16]}$$

where S_b is the signal intensity for each *b* value, S_0 the signal intensity at b_0, f (%) the fraction of diffusion linked to microcirculation, D (10^{-3} mm^2/sec) the pure diffusion coefficient, and D* (10^{-3} mm^2/sec) the perfusion-related diffusion coefficient. The reproducibility of the parameters measurements has been reported previously (131).

Magnetic resonance elastography

For MR elastography, harmonic mechanical waves were produced at 50 Hz by an electro-mechanical transducer placed near the liver on the right flank of the patient in supine position (Fig. 42) (95, 154 - 155). Synchronous motion-encoding bipolar gradients were added to a spin-echo sequence to encode the three directional components of the motion in the phase of the MR signal. The following sequence parameters were used: repetition time/echo time 560/40 ms, echoplanar readout with factor 3, matrix 80 × 80 pixels, 320-mm field of view, 7 transverse slices, slice thickness 4 mm and phase sampling of 4 points per vibration period. Nulling of fat signal was performed with spectral inversion recovery. The acquisition time was 19 s per direction. The consistency between breath holds was checked visually during data processing by assessing that the liver was at the same location on the consecutive images. Nine patients were excluded based on this visual assessment. The spatial resolution $(4\ mm)^3$ was chosen as a compromise between signal to noise ratio, acquisition time and spatial sampling of the wave. The complex-valued shear modulus was calculated from the phase images scaled to displacement values by first

suppressing the compressional components of the waves through application of the curl operator. Displacement values were then used to invert the local time-harmonic wave equation under physical constraints of local mechanical isotropy and incompressibility, as previously described (156, 157). Three-dimensional maps for the complex-valued shear modulus (G*, kPa), storage modulus (G', kPa) and loss modulus (G", kPa) were analyzed. Regions of interest were positioned in the liver on the viscoelastic maps matching the previous regions of interest in the DW parametric maps, by one of the authors with 6-year experience in MR imaging blinded to the results of the histopathologic analysis.

Statistical analysis

In this prospective study an *a priori* power analysis was performed and a minimum number of 45 patients had to be included to obtain a significance level of 0.05 and a power of 95% (95, 147). The univariate correlations between fibrosis, inflammation and steatosis on one hand, and the diffusion and viscoelastic parameters on the other hand were assessed with Spearman rank correlation coefficients (r) (158). In addition, fibrosis, inflammation and steatosis were introduced as independent variables in a stepwise multivariate regression model (the significant variables are entered sequentially, checked and possibly removed if non-significant), to assess their independent effect on the diffusion and viscoelastic parameters (159). With this model multivariate regression correlations (RC) were calculated.

$P \leq 0.05$ was considered to indicate a statistically significant difference. Statistical analysis was performed with the MedCalc software (MedCalc, Mariakerke, Belgium).

Results

In the 68 patients, the histopathologic analysis revealed the following distribution: fibrosis: F0 (n = 12; 18%), F1 (n = 27; 40%), F2 (n = 14; 20%), F3 (n = 9; 13%), F4 (n = 6; 9%); inflammation: A0 (n = 14; 20%), A1 (n = 39; 58%), A2 (n = 9; 13%), A3 (n = 6; 9%); steatosis: grade 0 (n = 34; 50%), grade 1 (n = 17; 25%), grade 2 (n = 11; 16%) grade 3 (n = 6; 9%). Three patients had only fibrosis (F1), two patients only inflammation (A1) and four patients only steatosis (grade 1: n = 2; grade 3: n = 2). Spearman correlation coefficients and multiple regression coefficients between fibrosis, inflammation and steatosis and the diffusion parameters and are shown in tables 14 and 15. A moderate negative correlation was observed between steatosis and the pure diffusion coefficient (r = - 0.5, $P < 0.0001$). The correlation between the pure diffusion coefficient and fibrosis was weak (r = - 0.3, $P = 0.01$). Inflammation showed a weak negative correlation with the perfusion fraction (r = - 0.3, $P = 0.04$) and none with the other parameters. In the multiple regression model, only steatosis showed an independent influence on the diffusion parameters and this was found exclusively for the pure diffusion coefficient (RC = - 0.4, $P = 0.0003$) (Fig. 50). Spearman correlation coefficients and multiple regression coefficients between fibrosis, inflammation and steatosis and the viscoelastic parameters are shown in tables 16 and 17. Fibrosis showed a univariate correlation with the shear and the storage moduli (G*: r = 0.6; G': r = 0.5; $P < 0.0001$), and a weak correlation with the loss modulus (G'': r = 0.4, $P = 0.001$). Inflammation showed a weak correlation (r = 0.2 - 0.4) with each viscoelastic parameter, as did steatosis. In the multiple regression model, fibrosis was a significant independent factor influencing the measured shear and storage modulus (G*: RC = 0.6; G': RC = 0.5; $P < 0.0001$) (Fig. 51). The multivariate correlation coefficient was weaker between fibrosis and the loss modulus (RC = 0.4, $P = 0.0002$). Steatosis showed a weak correlation (RC = 0.3, $P < 0.05$) on the shear and storage moduli

and inflammation had no effect on the measured viscoelastic parameters.

Table 14. Univariate Spearman rank correlations between diffusion parameters and fibrosis, inflammation and steatosis

	Fibrosis	**Inflammation**	**Steatosis**
D (10^{-3} x mm^2/s)	*P* = 0.01 r = - 0.3	*P* = 0.16	*P* = 0.0001 r = - 0.5
D* (10^{-3} x mm^2/s)	*P* = 0.5	*P* = 0.8	*P* = 0.14
f (%)	*P* = 0.2	*P* = 0.04 r = - 0.3	*P* = 0.7

Table 15. Multiple regression analysis between diffusion parameters and fibrosis, inflammation and steatosis

	Fibrosis	**Inflammation**	**Steatosis**
D (10^{-3} x mm^2/s)	nim	nim	*P* = 0.0003 RC = - 0.42
D* (10^{-3} x mm^2/s)	nim	nim	nim
f (%)	nim	nim	nim

nim, not in model.

Table 16. Univariate Spearman rank correlations between viscoelastic parameters and fibrosis, inflammation and steatosis

	Fibrosis	Inflammation	Steatosis
G* (kPa)	*P* < 0.0001 r = 0.6	*P* = 0.001 r = 0.4	*P* = 0.05 r = 0.2
G' (kPa)	*P* < 0.0001 r = 0.5	*P* = 0.01 r = 0.3	*P* = 0.003 r = 0.4
G'' (kPa)	*P* = 0.001 r = 0.4	*P* = 0.02 r = 0.3	*P* = 0.08

Table 17. Multiple regression analysis between viscoelastic parameters and fibrosis, inflammation and steatosis

	Fibrosis	Inflammation	Steatosis
G* (kPa)	*P* < 0.0001 RC = 0.6	nim	*P* = 0.02 RC = 0.3
G' (kPa)	*P* < 0.0001 RC = 0.5	nim	*P* = 0.01 RC = 0.3
G'' (kPa)	*P* = 0.0002 RC = 0.4	nim	nim

nim, not in model

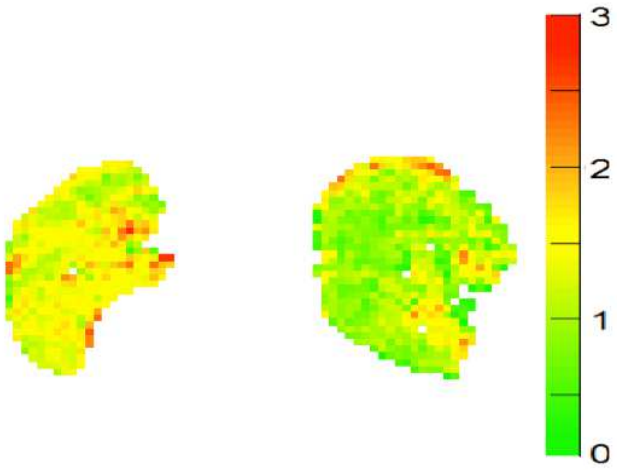

a **b**

Figure 50. Parametric color maps of true diffusion coefficient (10^{-3} mm^2/s) in two patients with viral hepatitis. METAVIR scoring and steatosis grading are: a) F1A0 steatosis grade 0, b) F1A0 steatosis grade 3. The mean values for the true diffusion coefficient are significantly decreased by the presence of steatosis.

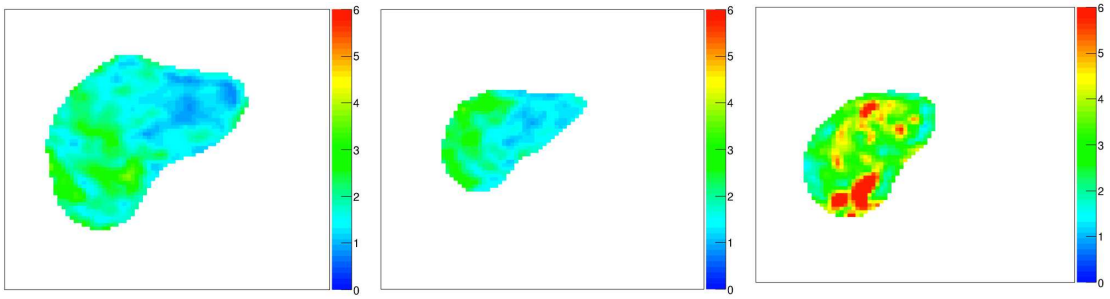

a **b** **c**

Figure 51. Parametric color maps of the complex shear modulus (kPa) in three patients with viral hepatitis. METAVIR scoring and steatosis grading are: a) F1A1 steatosis grade 0, b) F1A1 steatosis grade 2 and c) F3A2 steatosis grade 0. The mean values for the complex shear modulus are not significantly modified by the presence of steatosis: images a) G* = 2 kPa and b) G* = 1.8 kPa; but there is an increase in the measured complex shear modulus in the patient with higher liver fibrosis staging: image c) G* = 3.1 kPa.

Discussion

In this prospective clinical study we measured the correlation between liver fibrosis, inflammation, steatosis and the diffusion and viscoelastic parameters, in patients with viral hepatitis and nonalcoholic fatty liver disease. Our results in patients with chronic liver diseases show that the measurements of shear and storage moduli are mostly influenced by changes in liver fibrosis, while liver steatosis mainly influences the measurements of the pure diffusion coefficient and to a lesser extent those of the mechanical parameters.

Diffusion-weighted imaging has been increasingly used to assess liver fibrosis. In fact, previous studies have shown that the apparent diffusion coefficient values decrease in fibrotic and cirrhotic livers compared to the normal liver tissue, which is mainly related to the decrease in capillary perfusion (81, 82, 85, 87). However, there are still limited data regarding the specific influence of histopathologic findings such as inflammation and steatosis on the measured intravoxel incoherent motion parameters in patients with liver fibrosis. In our study, we found a significant negative correlation between the pure diffusion coefficient and the presence of liver steatosis. Moreover, steatosis was the only histopathologic factor that independently influenced the true diffusion coefficient. These results are in agreement with the recently reported findings by Leitão et al (146) and Guiu et al (147) in patients with pure steatosis and nonalcoholic fatty liver disease, respectively. Although an inverse correlation was found between liver fibrosis and the pure diffusion coefficient no independent influence was seen for fibrosis. Thus, our work clearly highlights that steatosis is definitively a confounding factor, that overweighs fibrosis when present. We did not see any univariate or multivariate correlation for the perfusion-related diffusion coefficient, which is not surprising since this is the most unstable parameter, has poor reproducibility and is prone to noise (83, 125).

It is known that the increase in liver stiffness is well correlated with the degree of fibrosis (103). However, conflicting data still exists regarding the influence of inflammation and steatosis, which frequently coexist with liver fibrosis in chronic liver disease, on the measurements of liver stiffness. In previous studies, inflammation has been reported to have no effect (95, 160, 161) or to increase the biomechanical parameters (102, 162 - 165). The differences in these results are probably related to the study population. In studies including an elevated proportion of high grade inflammation, especially in studies of patients with acute hepatitis or acute flares in chronic HBV infection, inflammation significantly increases the liver stiffness. In populations with more chronic diseases and less advanced grades of inflammation, this effect is not seen. Weak correlations between inflammation and the biomechanical parameters were observed in our study at univariate analysis and no significant effect of inflammation was seen at multivariate analysis. In contrast, in the study of Fraquelli et al. (164) inflammation was a significant confounder on stiffness measurements at multivariate analysis. In their study population, 54% of the patients had an inflammation grade < 2, whereas 46% were $A \geq 2$. Moreover, when we excluded the patients with ALT (Alanine Transaminase) > 2 the upper limit of normal, the correlation between inflammation and mechanical parameters disappeared. This shows that the relationship between stiffness measurements and fibrosis stage in patients with high ALT levels should be regarded cautiously. Therefore, it has been recommended to correct the stiffness measurements in patients with increased ALT levels. However, this correction is not yet used in clinical practice since different cut-off values for normal and elevated ALT levels have been proposed in order to adjust the inflammation-induced overestimation of fibrosis stage (166).

The influence of steatosis on the biomechanical parameters is also debated. Steatosis has been reported not to modify (95, 160,161, 167) to increase (103, 164) or even to decrease

the liver mechanical parameters (168). Again these differences may be explained by differences in steatosis grade between the populations, but also by differences in liver diseases with steatosis. Indeed, Fraquelli et al. (164) reported increases in liver stiffness with steatosis in patients with HCV infection, but not in patients with HBV or NAFLD. They explained this condition by the increase of inflammation and fibrosis that is caused by liver steatosis in patients with HCV. The decrease of stiffness observed in the study of Gaia et al. (168) in patients with steatosis is more difficult to explain, but may be caused by suboptimal measurements of transient elastography in obese patients. In our study, we observed that steatosis correlated weakly with the biomechanical parameters at univariate analysis and had a modest influence at multivariate analysis. We can conclude from our study that the measuremants of the biomechanical parameters are mainly influenced by the stage of liver fibrosis, whereas the measurements of the diffusion parameters are mainly influenced by liver steatosis. This is a strong argument for using MR elastograghy rather than DW-MRI to stage liver fibrosis. These results are in agreement with those of Wang et al. (97) who showed with ROC analysis the superior diagnostic performance of MR elastography relative to DW-MR imaging in staging liver fibrosis.

This study has some limitations that need to be acknowledged. First, the number of patients in this study, albeit acceptable, included only a small group with severe inflammation. However, this is a true reflection of the population with chronic liver disease. Our observations that inflammation has no influence on viscoelastic parameters may not be valid in patients with ALT flares, which highlight the need for its measurement. Secondly, we acquired free-breathing echo-planar diffusion-weighted imaging and physiological motion is always a concern when studying the microscopic displacement of protons. However, it was recently proposed that free breathing with multiple acquisitions is superior to complex gating techniques (75).

In conclusion our work confirms that the measured diffusion parameters are significantly modified by the presence of liver steatosis and that there is clearly an advantage in using MR elastography parameters when assessing patients with liver fibrosis, since these are less sensitive to the confounding effects of inflammation and steatosis.

Chapter VII

Other Experimental and Clinical Studies: unpublished data

7.1. Experimental Animal Study

7.1.1. Molecular Imaging of Liver Fibrosis with EP-2104R: a Feasibility Study in Rats

Introduction

Liver damage leads to the development of fibrosis as a paradigm of the wound healing process, since increased coagulant factors such as fibrin and fibrinogen have been described in chronic liver disease, despite the prolonged conventional coagulation tests (169 - 173). Furthermore, haemophiliac patients with chronic viral hepatitis demonstrate a slow progression of liver fibrosis (174). Currently, there are no effective antifibrotic drugs clinically available but the association between hypercoagulation and increased fibrosis seems to indicate that interference with the coagulation cascade may in fact reduce liver fibrosis.

EP-2104R is a novel fibrin-specific MR contrast agent that combines strong fibrin binding, fibrin selectivity, and high molecular relaxivity (175). EP-2104R was found to be effective at providing positive contrast enhancement in preclinical models of arterial and venous thrombosis and pulmonary emboli (176 - 180). Moreover, EP-2104R has already entered a phase II clinical trial and confirmed the increased specificity and sensitivity to detect thrombo-embolic disease in patients and without any serious adverse effects (180). This contrast agent demonstrated increased usefulness in both fresh as well as aged clots. However, the efficacy of EP-2104R in the detection of liver fibrosis was never assessed. Therefore, the purpose of this feasibility study was to determine whether fibrin-targeted dynamic MRI could be used as a noninvasive biomarker to detect liver fibrosis in a rat model.

Materials and Methods

Animal Model

All experiments were performed in accordance with the NIH (National Institutes of Health) Guide for the care and use of laboratory animals and were approved by the Athinoula A. Martinos Center care and use committee. Male Wistar rats (Charles River Laboratories, Wilmington, MA) were given weekly intraperitoneal injections of 100 mg/kg diethylnitrosamine (DEN; Sigma, St. Louis, MO) for 5 weeks (n = 5), defined as the moderate fibrosis group, and 9 weeks (n = 5), corresponding to the cirrhosis group. Control animals received PBS (phosphate buffered saline) for 4 weeks (n = 5) and 8 weeks (n = 5).

Probe

EP-2104R (EPIX Pharmaceuticals, Lexington, MA) represents a new class of MR imaging contrast agents in which a specific protein is targeted for imaging. EP-2104R comprises a fibrin-binding peptide (11 amino acid peptide) coupled to 4 gadolinium DOTA-like chelates (Fig. 52). EP-2104R binds equally to 2 sites on human or rat fibrin (Kd = 1.7 or 1.8 μmol/L, respectively) and has excellent specificity for fibrin compared with serum proteins, e.g., > 100-fold affinity relative to fibrinogen and > 1000-fold relative to serum albumin (175). The relaxivity of EP- 2104R bound to fibrin at 37 °C and at 1.4 Tesla is 71.4 $mM^{-1}s^{-1}$ (17.4 mM^{-1} s^{-1} by [Gd]), about 25 times higher than that of Gd-DOTA measured under the same conditions (175). EP-2104R was provided as a sterile, white lyophilized powder that was reconstituted at the site and administered to the animals at a dose of 1μL/g (20 μmol Gd/kg).

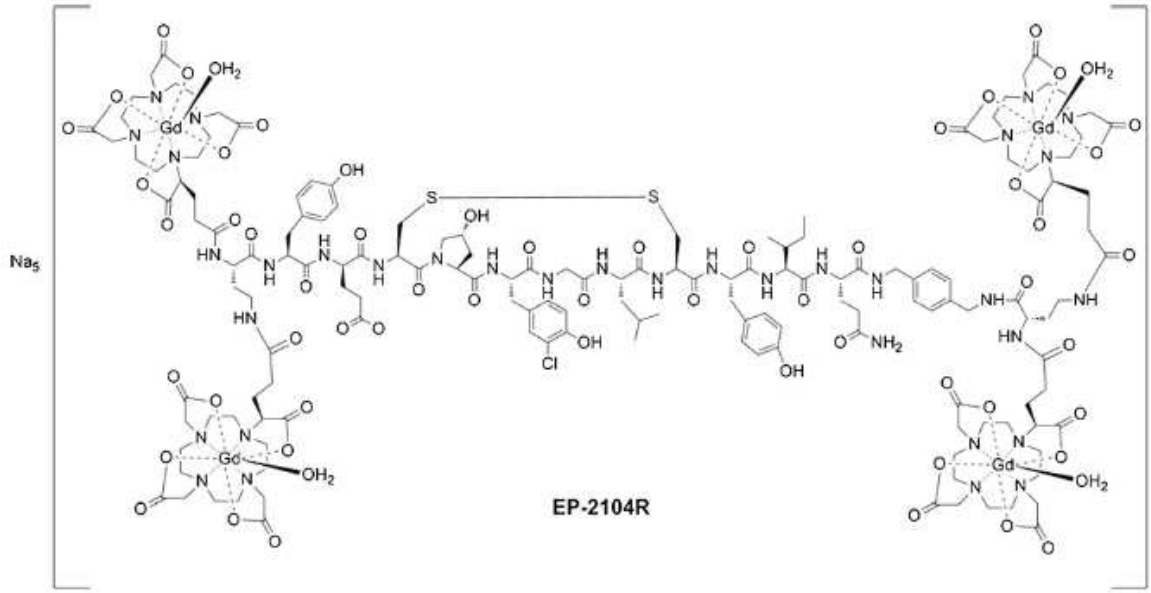

Figure 52. Chemical structure of EP-2104R. Reproduced from [175].

MR imaging and analysis

Rats were anesthetized with 2.5% isoflurane. Intraperitoneal injection of ketamine at a dose of 100 mg/kg was given as maintenance dose. The tail vein was cannulated for intravenous delivery of the contrast agent. Magnetic resonance imaging was performed in a 1.5-T MR unit (Magnetom Avanto Syngo, Siemens Healthcare, Erlangen, Germany) with a high-resolution 4-channel wrist coil. The animals were placed in prone position in the scanner and body temperature was approximately kept at 37.5 °C by a heating device.

The imaging protocol included pre and post contrast imaging with the 3D T1-weighted VIBE sequence with the following parameters: repetition time/echo time 7/3.27 ms, 77-mm field of view, matrix 192 x 192, in-plane resolution 0.4 mm, 30 transverse slices per slab, slice thickness 1 mm, 8 averages. The acquisition time was 3 min and 8 s. The T1 VIBE sequence post dynamic imaging was repeated out to 30 min. For the dynamic imaging a 2D multislice fast low angle shot sequence (FLASH) was used with the

following parameters: repetition time/echo time 5/2.17 ms, 80-mm field of view, matrix 61 x 61, in-plane resolution 1.3 mm, 1 transverse slice, slice thickness 3 mm, 4 averages. The total acquisition time was 6 min, 2 min baseline imaging and 4 min dynamic imaging.

A radiologist, with 5-year experience in MR imaging, drew a region of interest of ± 0.8 cm^2 in the right lobe of the liver of each rat. The signal intensity of the region of interest was measured using OsiriX imaging software (v.3.9.4 - 32 bits) with a specific homemade plugin (fit toolbox), and was exported to Microsoft Excel with Solver software (Fig. 53). Noise was quantified as the standard deviation of the signal intensity in the air adjacent to the animal. Contrast-to-noise ratio (CNR) was calculated as the signal intensity difference between liver and skeletal muscle.

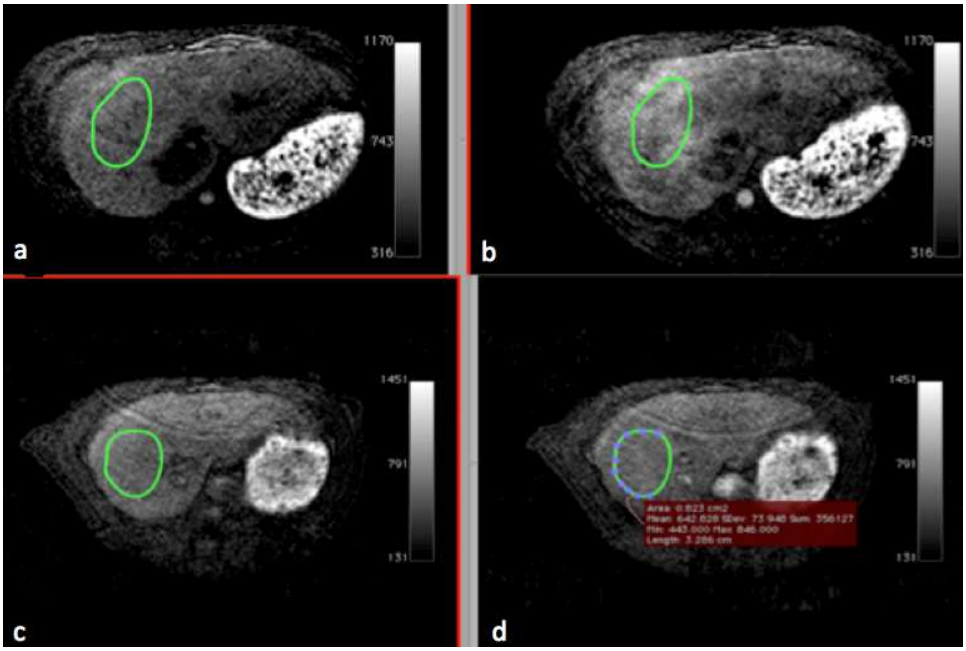

Figure 53. MR images before (a and c) and after EP-2104R injection (b and d) with regions of interest in rat with liver fibrosis (a and b) and control rat (c and d). Remaining signal intensity enhancement is observed in rat with liver fibrosis 30 min after EP-2104R injection.

Tissue Analysis

Several organs (liver, lungs, pancreas, spleen, kidney, muscle, heart, bone, tail, brain, fat and intestines) and blood were harvested 45 min after imaging. Formalin-fixed samples were embedded in paraffin, cut into 5 mm-thick sections and stained with sirius red according to standard procedures. The stained sections underwent blinded review by a board certified hepatobiliary pathologist to score the amount of liver fibrosis according to the METAVIR score (150). Gadolinium was quantified in tissue acid digests by inductively coupled plasma-mass spectrometry (Agilent 7500 Series, Agilent Technologies, California, USA) using dysprosium as internal standard. Gadolinium concentrations in the livers were normalized to the gadolinium concentration in blood to compensate for variations in the injected doses, and expressed as the percentage of the injected dose per wet weight of tissue.

Statistical Analysis

The differences between both groups of animals (control *vs* diseased) were assessed with Student's *t* test. A P value ≤ 0.05 was considered statistically significant. Statistical analysis was performed with the MedCalc software (MedCalc, Mariakerke, Belgium).

Results

During this feasibility study the rats of the cirrhotic group died at week 7 due to a nematode infestation in the animal house. One of our control rats also died during MR imaging. The final imaged population consisted of 4 rats with 5 weeks PBS injection (control group) and 5 rats with 4 weeks DEN injection (moderate fibrosis group). The

histopathological analysis revealed a normal liver parenchyma in the control group and the following fibrosis distribution for the diseased group: one rat had mild fibrosis (F1) and 4 rats moderate fibrosis (3 F2 and 1 F3) (Fig. 54).

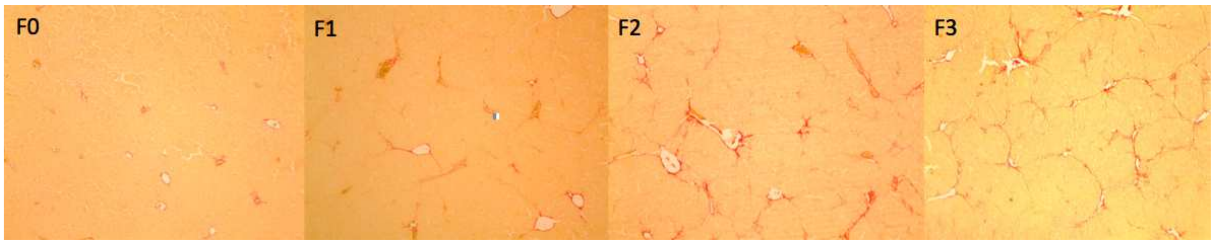

Figure 54. Liver slices stained with sirius red in four rats. Corresponding fibrosis stages are indicated in the upper left corner of each image.

Since one rat had only mild fibrosis after 4 week injections of DEN, it was removed from the analysis of the fibrosis group. The mean time to peak enhancement was significantly longer in fibrotic rats (22.4 s *vs* 14.4 s; $P = 0.002$) (Fig. 55). Signal intensity enhancement was still observed in the liver parenchyma 7 min after EP-2104R injection in the rats with liver fibrosis, but not in the control rats (mean enhancement 19.3 % vs 1%; $P = 0.01$) (Fig. 56). The prolonged retention of EP-2104R in the liver parenchyma of the rats with liver fibrosis was also shown by the lack of significant signal intensity decrease in the rats with liver fibrosis between 10 and 30 min after EP-2104R injection. The liver percentage of injected dose of gadolinium was higher in the rats with liver fibrosis than in the control rats, but the difference was not significant (Fig. 57). We also compared the increase in CNR at 7 min after EP-2104R injection relative to the baseline. Although the measured CNR at 7 min was higher in the rats with liver fibrosis relative to the normal rats, a statistically significant difference was not found.

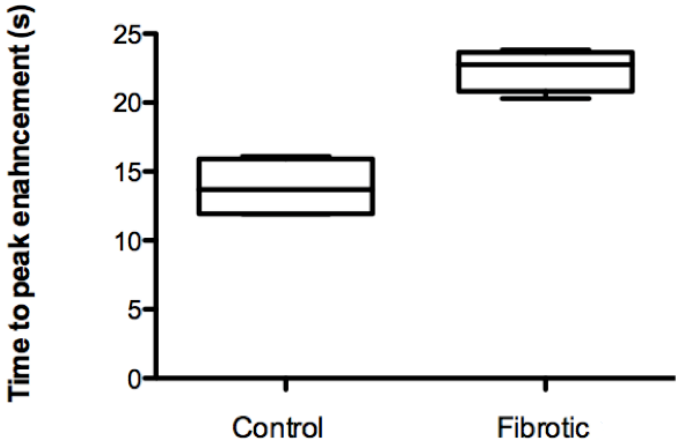

Figure 55. Time to peak enhancement (s) between control rats and rats with liver fibrosis. Time to peak enhancement is significantly higher in rats with liver fibrosis ($P = 0.002$)

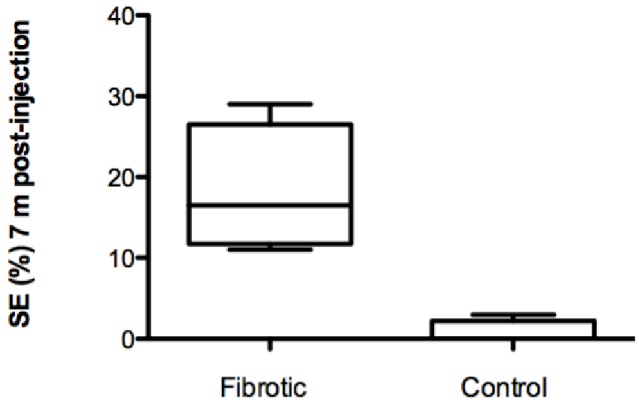

Figure 56. Signal enhancement in control rats and rats with liver fibrosis 7 min after EP-2104R injection. Signal enhancement is significantly higher in rats with liver fibrosis ($P = 0.01$).

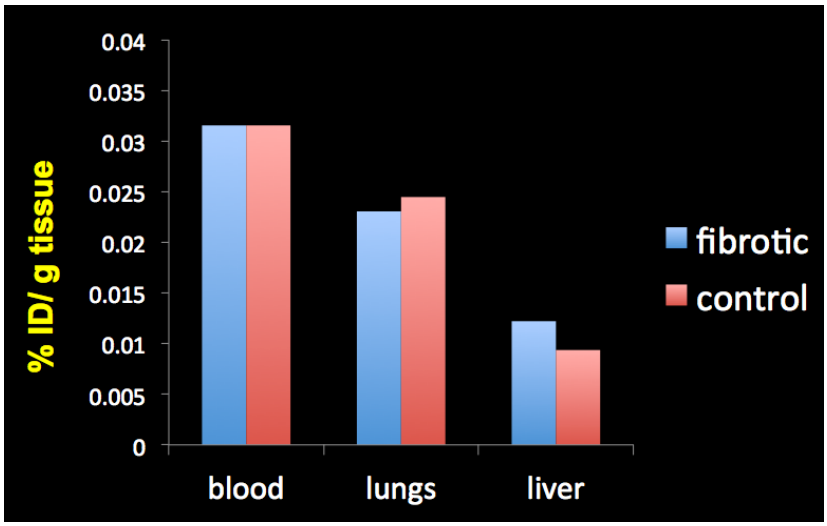

Figure 57. Percentage of injected dose per wet weight of tissue (blood, lungs and liver) in control rats and rats with liver fibrosis. The values represented are normalized by liver/blood and lung/blood ratio. There is a trend to higher percentage of injected dose in the liver of rats with liver fibrosis relative to control rats.

Discussion

In this feasibility study we were able to differentiate murine livers with moderate DEN induced fibrosis from normal livers with the novel fibrin-specific contrast agent EP-2104R. The time to peak enhancement with this contrast agent and the signal decrease in the liver were significantly prolonged in rats with liver fibrosis relative to controls.

The rationale of using a fibrin-targeting agent in liver fibrosis is based on the presence of a procoagulant status in liver fibrosis. For a long time clinicians thought that patients with cirrhosis were protected against thrombotic events. However, several studies have shown that patients with advanced hepatic fibrosis have a procoagulant state that places them at risk for thrombo-embolic episodes (174). Two complementary theories could explain how the coagulation cascade may be related with liver fibrosis (170, 174). The first one (parenchymal extinction theory) postulates that microthrombi in branches of the hepatic and portal veins are induced by the adjacent necroinflammatory activity. The resulting

imbalance between inflow and outflow leads to congestion and tissue ischaemia with resulting parenchymal extinction and replacement by fibrous tissue (Fig. 58). The second theory (direct stellate cell activation) proposes that the aggression to the liver parenchyma increases the expression of thrombin receptor PAR-1 and of tissue factor, which will initiate the coagulation cascade by increasing thrombin expression. The binding of thrombin to PAR-1 leads to direct stellate cell activation and fibrinogenesis (Fig. 58).

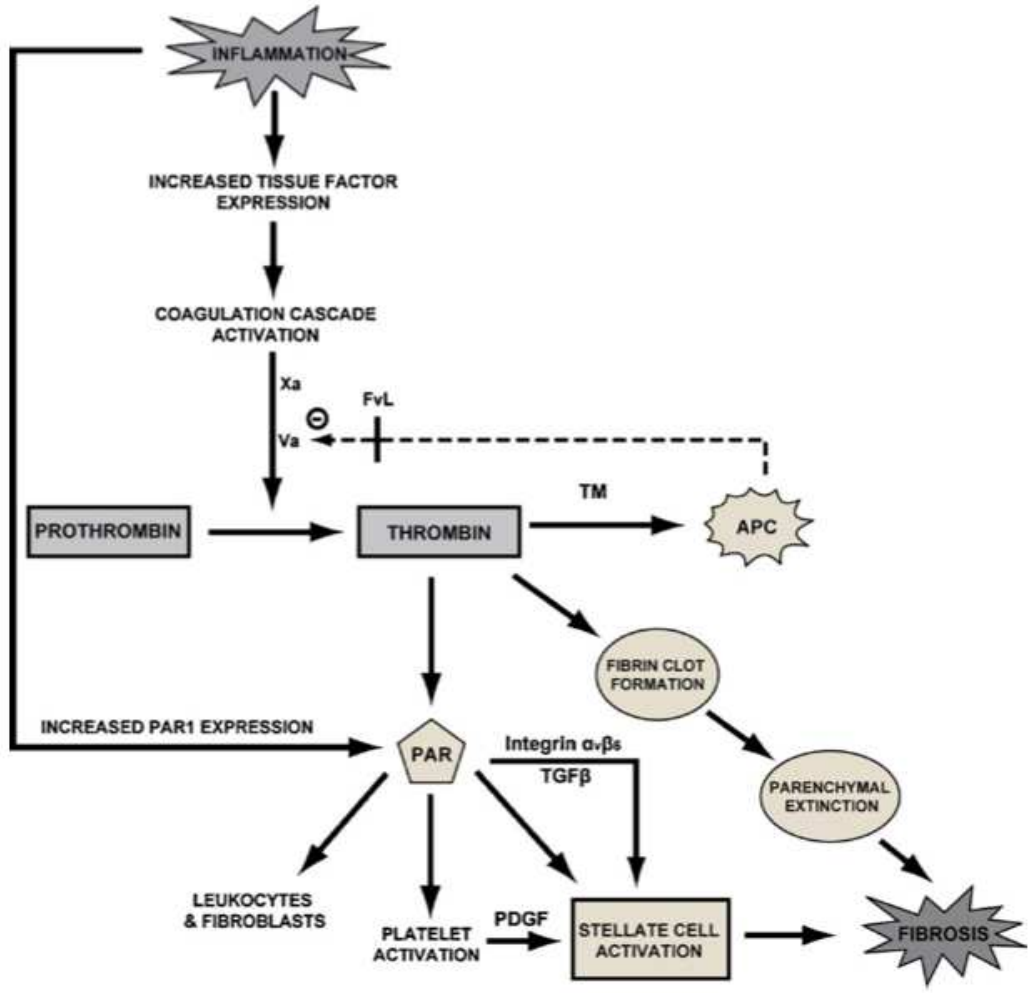

Figure 58. PAR-1 mediated actions of thrombin in stellate cell activation. Inflammation within the hepatic parenchyma increases expression of tissue factor, a key initiator of the coagulation cascade, and the thrombin receptor, PAR-1. Inflammation thus primes both the generation of thrombin and its down-stream signaling activity. In the presence of the FvL (factor V Leiden) mutation, the normal thrombin/ thrombomodulin negative feedback loop via activated protein C (APC) that limits thrombin production is ineffective. This allows thrombin generation to proceed unchecked in a hepatic environment that is already sensitized for PAR-1 mediated stellate cell activation both directly and via platelet released PDGF (platelet-derived growth factor). (TM, thrombomodulin). Reproduced from [174].

The fibrin-targeted agent presented here has the potential to be a complementary approach to detect liver fibrosis. We were, nonetheless, somewhat surprised by the small concentrations of the probe in the liver. This might be explained by probe binding in other organs. We analyzed blood, liver and lung with inductively coupled plasma-mass spectrometry and also found EP-2104R in the lung. This is not totally surprising because pulmonary and liver fibrosis have the same pro-coagulant and pro-fibrotic factors. Moreover, DEN is able to induce lung injury (181 - 183). The kinetic properties of EP-2104R found in this study were significantly different between controls and rats with fibrosis, even though we only assessed a group with moderate fibrosis. Moreover EP-2104R offers a genuine clinical potential since in phase II trials for thrombi detection, no serious adverse events were observed in patients. EP-2104R also has a high relaxivity at common clinical field strengths (1.5 and 3 T). Although with this work we tried to demonstrate the feasibility of using EP-2104R as fibrin targeting agent in liver fibrosis, this study has some limitations that need to be acknowledged. First, we did not evaluate EP-2104R in rats with liver cirrhosis. Second, we only analyzed the concentrations of the probe in the liver, lung and blood. Third, fibrin immunohistochemistry of liver slices was not performed. These points will however be addressed in future studies.

In conclusion, the results of our study in rats with DEN induced liver fibrosis suggest that the fibrin-targeting agent EP-2104R may be useful for distinguishing between normal liver parenchyma and liver fibrosis.

7.2. Clinical Studies

7.2.1. Accuracy and Reproducibility of ShearWave Elastography to Assess Liver Fibrosis in Patients with Chronic Viral Hepatitis and Nonalcoholic Fatty Liver Disease

Introduction

Liver biopsy with histopathological quantification is the current gold standard to stage fibrosis. However, this method is invasive, not easily accepted by the patient, provides only a semiquantitative evaluation and suffers from pooling errors in the assessment of diffuse and heterogeneous liver diseases (4, 50). The need for novel noninvasive imaging biomarkers is a real clinical challenge. Although serum biomarkers have been proposed to stage fibrosis, their diagnostic value still remains debated for intermediary stages of fibrosis (23, 37, 44, 46, 50). Transient elastography was the first ultrasound-based method implemented in clinical practice showing that liver stiffness rises along with increasing fibrosis stages (23, 37, 43, 44). However, this method has limitations because measurements are difficult to obtain in at least 16% of the patients and are often impossible to obtain in patients with ascites or who are obese (23). Shearwave elastography (SWE) is a new ultrasound-based method with ultra rapid image acquisition under evaluation in the clinical setting (58, 59). Very few studies have evaluated SWE and mostly only included hepatitis C patients, but clinicians are already confronted with conflicting results (58, 60, 184). Moreover, reproducibility of the technique has only been assessed in healthy volunteers. Therefore, the purpose of this still ongoing work was to (1) determine the performance of shearwave elastography to differentiate F0-1 *vs* $\geq$ F2 fibrosis stages in patients with chronic viral hepatitis and NAFLD and the respective cut-off value, (2) assess interobserver reproducibility, (3) evaluate the independent influence of steatosis and

inflammation on the measurement of liver stiffness and (4) determine the time it adds to routine abdominal ultrasound examinations.

Materials and Methods

Patients and study protocol

The review board at our institution approved this single-center and prospective clinical study and informed consent was obtained for all patients. From March through October 2012, all consecutive patients 18 years or older, with suspected chronic viral hepatitis or nonalcoholic fatty liver disease, scheduled for liver biopsy were enrolled for this study. A total of 50 patients were included in the study protocol that consisted of real-time SWE studies using the Aixplorer US system (SuperSonic Imagine, Aix-en-Provence, France) with a convex broadband probe (SC6-1). Two patients were excluded because they missed the scheduled appointment. The final study population consisted of 48 patients, 21 women and 27 men, with a mean age of 40 years for women (range: 29 - 66 years) and 44 years for men (range: 24 - 71 years) and mean body mass index of 26.1 kg/m^2 (range: 20 – 40 kg/m^2). Seventeen patients had viral hepatitis B, 22 viral hepatitis C and 9 nonalcoholic fatty liver disease. A board certified hepatobiliary pathologist who was unaware of the imaging results performed the histopathologic analysis of all liver specimens. Fibrosis and inflammation were documented according to the METAVIR or NAS scoring systems (27, 150, 151) and steatosis was graded according to the Brunt classification (4), as previously explained in Chapter II, sections 2.2.1. and 2.2.2.. The mean interval between biopsy and SWE was 14 days (range: 0 - 60 days).

Supersonic Shear Imaging

All measurements were performed in the right lobe of the liver with the patient lying in a dorsal decubitus position. The right arm was always maintained in abduction to enlarge the intercostal space as much as possible and to increase access to the right hypochondrium. The patient was asked to be fasting, as before conventional ultrasound imaging, and to maintain either a shallow breathing or apnea when asked. All measurements were performed between 2 and 7 cm of the surface of the liver to prevent reverberation artifacts beneath the Glisson's capsule and ensure good wave penetration. Observer 1 (10-year experience in abdominal ultrasonography) obtained liver stiffness measurements from a circular region of interest, 20 - 22 mm in diameter, avoiding large vessels or focal liver lesions. The mean value of three consecutive measurements in segments V, VII and VIII was used for statistical analysis. Observer 2 (3-year experience in abdominal ultrasonography) blinded to the results of observer 1 repeated three measurements only in segment V. The resulting liver stiffness was displayed in the circular region of interest as a color map and at the right side of the image as maximum, minimum and mean values and respective standard deviations (Fig. 25). Measurements were defined as failures when no or little signal was obtained in the SWE box. Total time required for the measurements was assessed for each patient and observer.

Statistical Analysis

The performance of SWE to distinguish patients with a fibrosis stage ≥ F2 was determined by calculating the area under the receiver operating characteristic curve (AUROC). Univariate correlations between stiffness measurements and fibrosis, inflammation and steatosis were calculated with Spearman rank correlation coefficients (r) (158). In addition,

fibrosis, inflammation and steatosis were introduced as independent variables in a multivariate regression model to assess their independent effect on the measured parameter (159). With this model multivariate regression correlations (RC) were calculated. Groups of patients with different inflammation grades among the same fibrosis stage were compared with the Kruskal-Wallis test. Interobserver reproducibility was calculated using intraclass correlation coefficients. A P value ≤ 0.05 was considered statistically significant. Statistical analysis was performed with the MedCalc software (MedCalc, Mariakerke, Belgium).

Results

In the 48 patients the histopathologic analysis revealed the following distribution. Fibrosis stage: F0 (n = 7), F1 (n = 18), F2 (n = 7), F3 (n = 8), F4 (n = 8); inflammation grade: A0 (n = 9), A1 (n = 23), A2 (n = 11), A3 (n = 5); steatosis grade: S0 (n = 23), S1 (n = 9), S2 (n = 11), S3 (n = 5). The univariate correlations between stiffness on one hand and fibrosis, inflammation and steatosis on the other were always significant but only fibrosis had a correlation coefficient above 0.5 (Fibrosis: r = 0.63, $P < 0.0001$; Inflammation: r = 0.40, $P = 0.005$; Steatosis: r = 0.35, $P = 0.02$). Although measured stiffness values within the same fibrosis stage showed an increasing trend with severe inflammation grade, no significant statistical difference was found between groups (Table 18). Only liver fibrosis was found to have an independent effect on the liver stiffness (RC = 0.69, $P < 0.0001$). Using liver biopsy as the reference examination we found that a SWE cut-off value of 10.3 kPa provided the diagnosis of $\geq$ F2 with 80% sensitivity and 95% specificity. The AUROC was 0.92, $P < 0.0001$ (Fig. 59). The real-time SWE examination lasted approximately 7 minutes per patient for observer 1 (three segments measured) and 3 minutes for observer 2

(one segment measured). No measurement was classified as failure (Figs. 60, 61). The intraclass correlation coefficient for the interobserver agreement was 0.99 (95 % CI, 0.98 - 0.99).

Table 18. Mean SWE stiffness and standard deviation according to fibrosis stage and inflammation grade

	F0-1	F2	F3	F4
A0	7.1 ± 1.3		12 ± 0	24.7 ± 0
A1	8.5 ± 1.6	10.1 ± 2.7	9.4 ± 1.4	24.9 ± 1.6
A2	7 ± 0	10.5 ± 0	10.4 ± 1.4	31 ± 3.5
A3	10.9 ± 4.2	17.8 ± 0	16.5 ± 2.6	

Note: Stiffness values within the same fibrosis stage showed an increasing trend with severe inflammation grade but no statistically significant difference was observed.

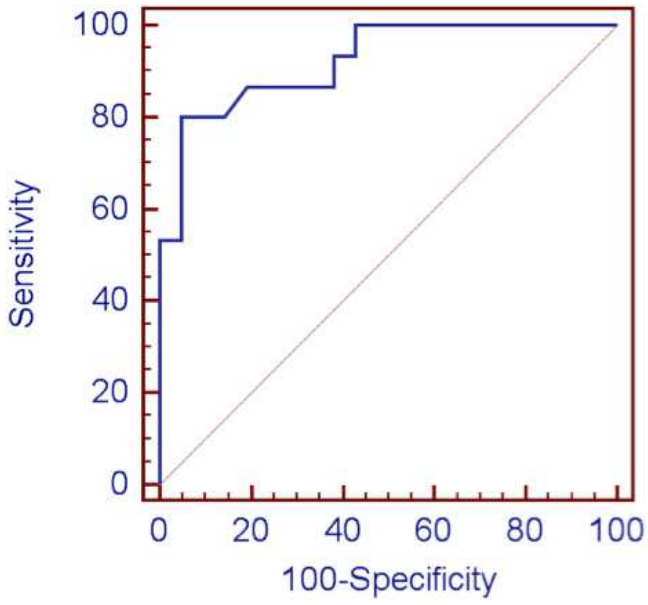

Figure 59. Real-time SWE AUROC (0.92, *P* < 0.0001) to differentiate between F0-1 *vs* F2-4 fibrosis stages.

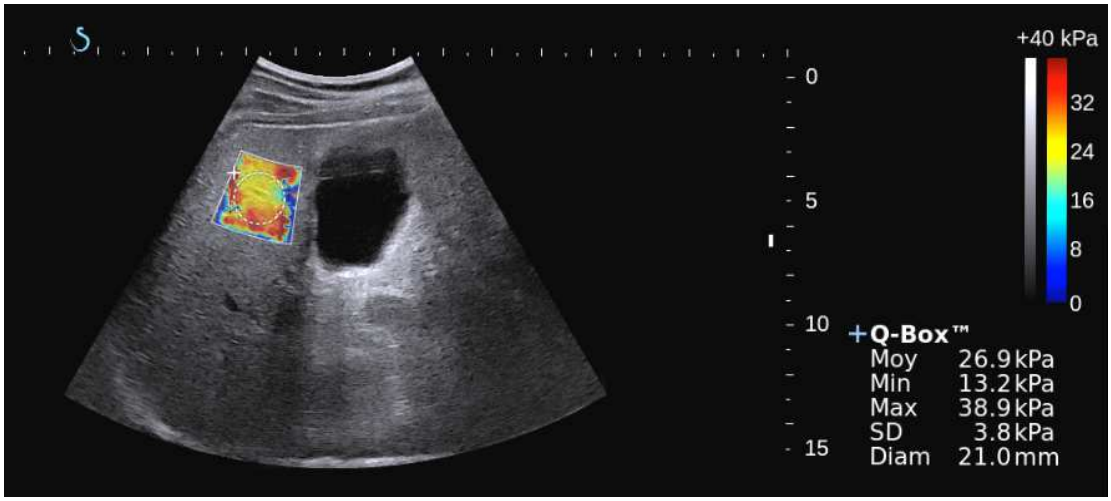

Figure 60. SWE stiffness (26.9 kPa) in a patient with chronic hepatitis B. METAVIR score was A2F4 and no steatosis was identified on the liver slice.

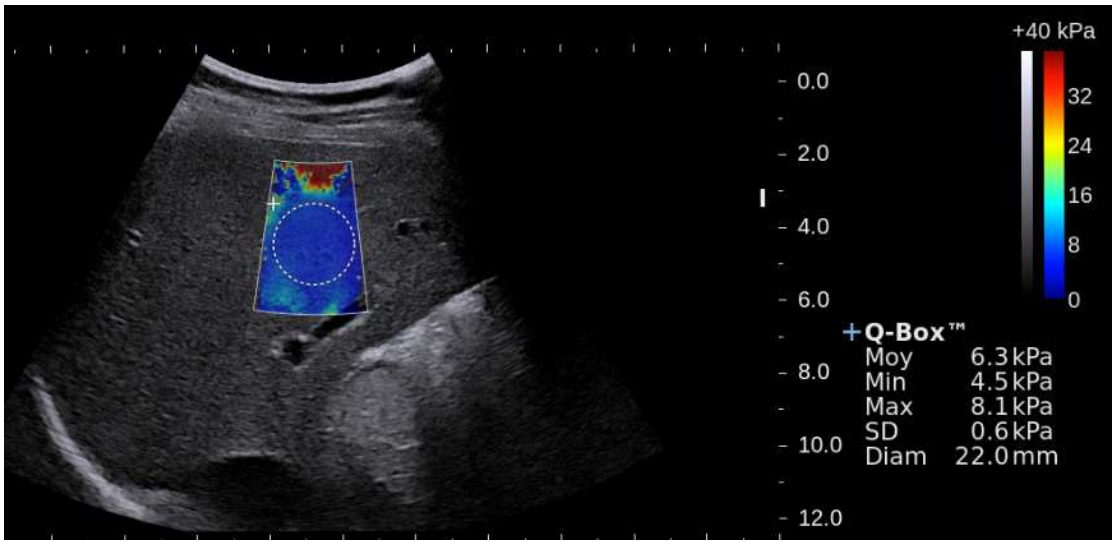

Figure 61. SWE stiffness (6.3 kPa) in a patient with chronic hepatitis C. METAVIR score was A2F0 and no steatosis was identified on the liver slice.

Discussion

In this preliminary prospective clinical study, which included patients with viral hepatitis and NAFLD, we have found that only fibrosis has an independent effect on the liver stiffness measured with SWE. Moreover, SWE had excellent interobserver reproducibility and could accurately differentiate patients with F0-1 vs F2-4 fibrosis stages with an AUROC of 0.92 ($P < 0.0001$).

Real-time SWE is a novel ultrasound-based elastography method under evaluation for the assessment of liver fibrosis in patients with chronic liver diseases. Few studies have assessed the performance of SWE (58, 60, 184) and apart from the recent study by Poynard et al (184) which did not use liver biopsy as reference examination, the evaluation was limited to patients with chronic hepatitis C. Ferraoili et al (60) recently reported results similar to ours in a population of patients with hepatitis C with AUROCs of 0.92 and 0.99 respectively for $F \geq 2$ and F4.

In our study, no measurement was classified as having failed, even in the 9 patients with a BMI higher than 30 kg/m^2. We do acknowledge that a learning curve is needed for SWE as for all imaging methods but we do not think that 100 examinations should be performed to be an experienced operator, as reported by Poynard et al (184). Indeed, in contrast to Fibroscan, SWE offers the advantage of being incorporated in a common ultrasound device allowing direct comparisons between SWE and B-mode images. Since both operators in our study were experienced in abdominal ultrasound examinations, the learning curve for SWE was rapid and both operators felt confortable performing SWE examinations after 15 patients, which comes in agreement with the findings by Ferraioli et al (185).

Although this is an ongoing study and at the time of this thesis limited to 48 patients, two of our patients, both diagnosed with NASH, were puzzling. Patient 1 had a mean liver

stiffness of 13.9 kPa while patient 2 had 7.9 kPa stiffness (Figs 62, 63). However, the histopathologic score classified both patients as having mild fibrosis (F1) and severe inflammation (A3). Steatosis was also classified as grade 2 for both patients (34 - 66 %).

Figure 62. SWE stiffness (13 kPa) in a patient with NASH.

The reason for the discrepancy in liver stiffness is not completely understood because the SWE studies were considered valid by the two observers each time, which also obtained very similar liver stiffness values. Moreover, apart from the different gender, no significant clinical differences (e.g. BMI, age, transaminases, comorbidities) were found between them. Additionally, the pathologist reviewed the histological slices and made no changes in the previously attributed score. Although these results are still preliminary, we might hypothesize that in patient 1 fibrosis was more heterogeneously distributed and in this case the limited parenchymal evaluation of liver biopsy underscored the patient. Moreover, these two patients also participated in the study described in chapter VI and the measured monofrequency (50 Hz) MRE storage modulus (≈ elasticity) was also higher for patient 1.

Figure 63. SWE stiffness (7.9 kPa) in a patient with NASH.

Our study has limitations that need to be acknowledged. First, the number of included patients is small. However, this is an ongoing study and we plan to include more than 100 patients. Second, since none of our patients had ascites we were not able to assess the potential influence of this factor on the SWE measurements.

In conclusion, this is the first study to assess the performance and reproducibility of SWE in patients with chronic viral hepatitis B, C and NAFLD, using liver biopsy as gold standard. We found that SWE can accurately detect patients with a fibrosis stage ≥ F2, has excellent interobserver reproducibility and it can easily be incorporated in the routine abdominal ultrasound examinations. Moreover, only fibrosis was found to have an independent effect on liver stiffness.

7.2.2. Evaluation of Multifrequency MRE Wavelength Exponent in Patients with Liver Fibrosis and Inflammation: a Feasibility study

Introduction

Magnetic Resonance Elastography (MRE) is sensitive to changes induced by fibrosis in the mechanical properties of the liver and is now acquiring a more relevant place in the clinical setting (95 – 97, 186). Liver inflammation is frequently associated with fibrosis but so far a noninvasive imaging biomarker to detect and differentiate inflammation grades has not been found. Standardization for MRE studies has been difficult because the behavior of compressional and shear waves is influenced by the frequency of excitation applied in the first place, thus the obtained viscoelastic values are difficult to compare (98, 186 - 188). This frequency-dependent wave attenuation and dispersion at the tissue and cellular level can nevertheless be explained by a common wave equation modeled by a power law, therefore excluding frequency dependence (187). Asbach et al (98) used a frequency-independent shear modulus to evaluate patients with liver fibrosis and found that this parameter did not have a superior performance compared to the monofrequency evaluation. However, the authors did not assess the influence of inflammation on their measured parameters neither did they study the behavior of the wavelength. Therefore, the purpose of this still ongoing study was to evaluate the performance of the frequency-independent wavelength exponent in patients with liver fibrosis and inflammation.

Materials and Methods

The review board at our institution approved this single-center and prospective clinical study and written informed consent was obtained for all patients. From March through October 2012, all consecutive patients 18 years or older with untreated chronic viral hepatitis scheduled for liver biopsy were enrolled for this study. A total of 35 patients were included in the study protocol, which consisted of multifrequency MRE on a 1.5-T MR unit (Philips Healthcare, Best, The Nederlands) using a gradient-echo sequence with the following parameters: TR/TE=112 ms/9.6 ms, 320-mm field of view, 9 transverse slices, 4 mm^3 isotropic resolution, 3-directional encoding, 8 points per vibration period. The total acquisition time was 1m 20s. The simultaneous 28, 56 and 84 Hz mechanical waves were induced with an electromechanical transducer placed closed to the liver on the right flank of the patient in supine position (Fig. 43). The complex-valued shear modulus was calculated by demodulation and local inversion of the linear viscoelastic 3D wave equation and converted into wavelength (λ, mm). The frequency dependence modeled by a power law was assessed as the wavelength exponent parameter (Υ_λ). Ten patients were excluded because of technical problems. The final study population consisted of 25 patients, 7 women and 18 men, with a mean age of 48 years (range: 31 - 68 years). Eight patients had chronic hepatitis B and 17 had chronic hepatitis C. An expert hepatobiliary pathologist who was unaware of imaging results performed the histopathologic analysis of all liver specimens. Fibrosis and inflammation were documented according to the METAVIR scoring system, as described in chapter II, section 2.2.1. (150). The mean interval between biopsy and MRE was 24 days (range: 4 - 60 days).

Statistical Analysis

Patients with different inflammation grades and fibrosis stages were compared with the Kruskal-Wallis test. The performance of Υ_λ to distinguish between A0-1 *vs* A2-3 was determined by calculating the area under the receiver operating characteristic curve (AUROC). A P value ≤ 0.05 was considered statistically significant. Statistical analysis was performed with the MedCalc software (MedCalc, Mariakerke, Belgium).

Results

Values are presented as mean ± standard deviation. In the 25 patients the histopathologic analysis revealed the following distribution. Fibrosis stage: F0 (n = 2), F1 (n = 13), F2 (n = 3), F3 (n = 7); Inflammation grade: A0 (n = 5), A1 (n = 15), A2 (n = 4), A3 (n = 1). The wavelength exponent decreased with increasing inflammation grades and the difference was statistically significant between A0 and A2 ($P < 0.01$) (Fig. 64). Using liver biopsy as the reference standard we found that a cut-off value of -0.43 for Υ_λ provided an accurate separation of inflammation grades A0-1 from A2-3 with a sensitivity and specificity of 100% and 85%, respectively. The AUROC was 0.95 (Fig. 65). Although wavelength exponent could also differentiate patients with fibrosis stages F0-1 *vs* F2-3 (AUROC 0.93), when examining the subgroups of patients within the same fibrosis stage, the decrease in Υ_λ as a function of the inflammation grade was still systematically observed, although no statistical significance was observed in this feasibility pool of 25 patients (Fig. 66, Table 19)

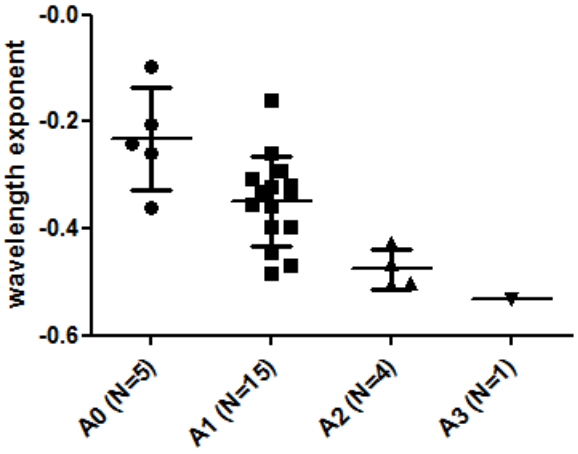

Figure 64. Wavelength exponent values among different inflammation grades.

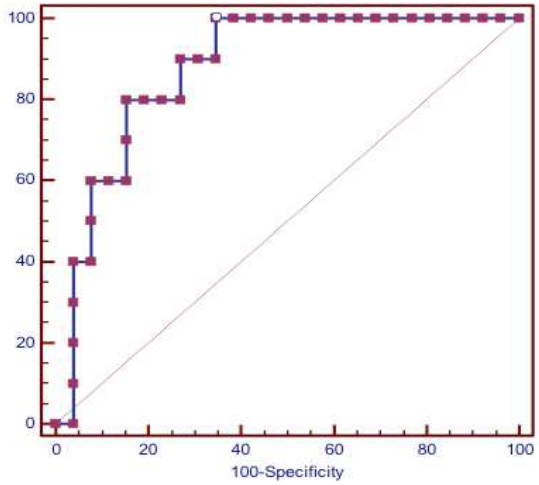

Figure 65. MRE wavelength exponent AUROC (0.95, *P* < 0.0001) between inflammation grades A0-1 vs A2-3.

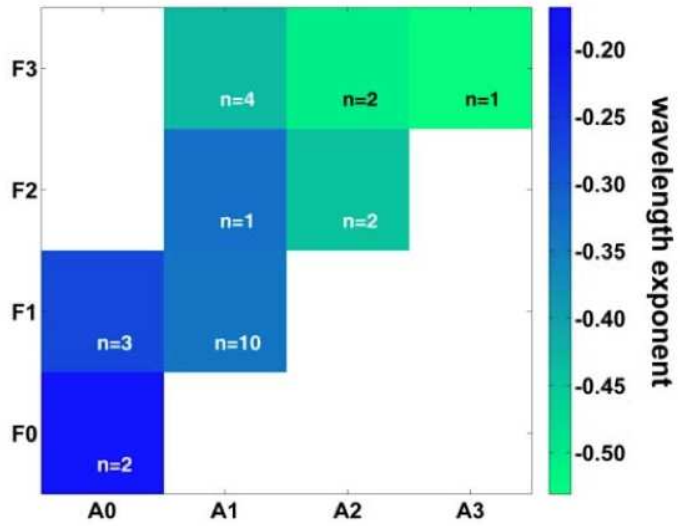

Figure 66. Wavelength exponent color scale according to the fibrosis stages and inflammation grades. n = number of patients per corresponding fibrosis stage and inflammation grade.

Table 19. Mean wavelength exponent values and standard deviations according to the fibrosis stages and inflammation grades

	F0	F1	F2	F3
A0	- 0.22 ± 0.03	- 0.27 ± 0.08		
A1		- 0.33 ± 0.05	- 0.33 ± 0.01	- 0.43 ± 0.07
A2			- 0.45 ± 0.03	- 0.51 ± 0.01
A3				- 0.53 ± 0.01

Note: wavelength exponent values within the same fibrosis stage showed a decreasing trend with increasing inflammation grades but no statistically significant difference was observed.

Discussion

In this preliminary prospective clinical study, which included patients with chronic viral hepatitis, we have found that the wavelength exponent can accurately differentiate A0-1 from A2-3 inflammation grades. Moreover, this frequency-independent parameter seems to decrease according to the inflammation grade independently of the fibrosis stage.

Elastography-based methods characterize the mechanical properties of the liver through the measurement of viscoelastic parameters. MR elastography measures the whole spatial displacement vector, which allows assessment of the wave number and propagation and separation of elasticity and viscosity parameters. In fact, assuming that elasticity is the only parameter that defines the mechanical behavior of biological tissues will result in evaluation errors since their viscous property is being ignored (92, 98). Even though MRE is progressively acquiring a new place in the assessment of liver fibrosis, comparisons among obtained results are difficult and MRE is still far from standardization. Several studies have shown that both healthy and diseased liver display a frequency-dependent elastodynamic behavior, which also depends upon the postprocessing model used (98, 188 - 191). Therefore, any specific viscoelastic parameters have to be given in the context of the underlying model and detailed by the frequency of excitation applied. One way to overcome this drawback is to use frequency-independent viscoelastic parameters.

Although in the work by Asbach et al (98) the multifrequency MRE (50 - 62.5 Hz) did not surpass the previously reported performance of monofrequency for fibrosis staging, this was the first and crucial step to MRE standardization. Moreover, MRE has the potential for additional increases in technical innovation that will undoubtelly further improved the diagnostic accuracy.

It was already demonstrated in chapter VI that the complex shear modulus and the storage

and loss moduli are not able to assess liver inflammation, since the necroinflammatory activivity was not found to have any independent effect on these parameters. In this preliminary work we used the multifrequency-derived and frequency-independent parameter, wavelength exponent, to assess liver inflammation. The spectrum of frequencies used in our work from 28 - 84 Hz matches the range of frequencies already used in several studies (95 - 98, 102, 186). The results of this study demonstrate that the wavelength exponent can accurately differentiate patients with mild inflammation from those with moderate and severe inflammation. Moreover, within the same fibrosis stage we found that there was a decreasing trend in the measured wavelength exponent with increasing inflammation grades. This could have overall important clinical implications, namely in patients with NAFLD since the detection of increased parenchymal activity could prevent patients from progressing to severe fibrosis and cirrhosis.

Our study has limitations. First, the number of included patients is small. However, this is still an ongoing study. Second, we did not assess the repeatability of our measurements in the same cohort of patients.

In conclusion, our results show that the wavelength exponent parameter might be an important biomarker to assess inflammation in patients with chronic liver disease. Moreover, the frequency-independence of this parameter will allow a higher standardization and comparison among liver MR elastography studies.

Chapter VIII

Summary, Final Considerations and Perspectives

8.1. Summary

The results of the present research project have led to the final conclusions:

Chapter IV

In patients without clinical or imaging evidence of iron overload the quantification of the mean liver fat content can be easily performed in routine clinical practice. The use of a simple and fast gradient echo sequence, with only three echo times, allows accurate mapping of diffuse liver fat with excellent intra- and interobserver reproducibility. This mapping technique has the potential for early detection of NAFLD, thus reducing the risk of progression to severe stages of this disease.

Chapter V

Magnetic resonance diffusion-weighted imaging is increasingly used to quantify hepatic fibrosis. This IVIM DWI prospective study was the first one to demonstrate, in patients with liver biopsy, as the reference examination, that steatosis has a higher impact than fibrosis in the measured diffusion parameters. Precaution is therefore warranted when using the pure diffusion coefficient in the assessment of liver fibrosis.

Chapter VI

In this prospective clinical study, two sets of noninvasive MR imaging parameters (diffusion and viscoelastic) used to quantify liver fibrosis were put side-by-side and the influence of inflammation and steatosis in their final measurements was assessed. The results of our study suggest that magnetic resonance viscoelastic parameters are best for the evaluation of liver fibrosis since they are less sensitive to the concomitant presence of parenchymal inflammation and steatosis.

Chapter VII

Experimental study

The development of liver fibrosis has been closely related to the activation of the coagulation system with increased perisinusoidal fibrin accumulation. This pilot MR molecular imaging study in rats with liver fibrosis suggests that the fibrin-binding contrast agent EP-2104R has the potential to detect moderate and severe fibrosis. Since this compound was already assessed in patients without any serious adverse effects it may be a complementary approach to the already existing noninvasive MR-based diffusion and viscoelastic biomarkers.

Clinical study 1

The changes that occur in the extracellular matrix during liver fibrosis have been shown to directly influence the mechanical properties of the liver. In this prospective clinical study ultrasound-based shearwave elastography was used to evaluate patients with chronic viral hepatitis and NAFLD. This imaging technique was found to be accurate in distinguishing patients with mild fibrosis from those with moderate and severe fibrosis, exhibiting excellent interobserver reproducibility. Inflammation and steatosis were not found to influence the measurements of liver stiffness. Moreover, shear wave elastography is easy to perform and already implemented in the commonly available ultrasound devices, enabling its use as an epidemiologic screening tool in clinical practice.

Clinical study 2

The recognition of liver inflammation is important for detecting active and evolving chronic liver diseases. Until now no imaging biomarker was found for liver inflammation. In this pilot study, multifrequency MR elastography was used to assess patients with

fibrosis and liver inflammation. Our results suggest that the frequency-independent wavelength exponent has the potential to identify and grade liver inflammation.

8.2. Final Considerations and Perspectives

The statement “more discoveries have arisen from intense observations of a very limited material than from statistics applied to large groups…”, is especially true in imaging findings, as the radiologist struggles even more than all other medical specialties to include patients in their research studies (192).

The goal of this thesis was to uncover noninvasive imaging biomarkers to characterize chronic liver diseases; i.e., liver fibrosis, inflammation and steatosis. But what does the concept of biomarker mean? Biomarkers are by definition measurable parameters that allow us to assess normal biological or pathological processes or the response of tissues to therapeutic interventions (193, 194). According to the ESR (European Society of Radiology) statement on the development of biomarkers, “the clinical value of new biomarkers is of the highest priority in terms of patient management, assessing risk factors and disease prognosis” (194). New biomarkers should also overcome the important limitations of our current gold standard in chronic liver disease; i.e., liver biopsy.

Quantifying liver steatosis in routine clinical examinations answers many questions and has important medical implications. Undoubtedly, it will allow early detection and follow-up of NAFLD patients. But we can go even further and widespread this assessment to the follow-up of patients under treatment with tamoxifen, antidiabetic drugs, amiodarone, antiretrovirals, etc (25, 53). Moreover, accurate and diffuse quantification of liver steatosis will help selecting patients that best fit the requirements for liver donors as the presence of steatosis in transplanted livers carries an important risk of hepatocellular insufficiency. Furthermore, the detection of preoperative liver steatosis is associated with increased perioperative risks and even death after major hepatic resection (two or more segments) (53, 195 - 199).

The noninvasive assessment of liver inflammation and fibrosis/cirrhosis in at-risk groups (viral hepatitis, alcoholic and nonalcoholic liver disease, patients under methotrexate treatment, etc.) and in the general population is an obvious clinical need. Interestingly, I was able to experience in first hand that sympathy and the word “noninvasive” have generally a very good acceptance by patients with chronic liver disease. In this project two elastography methods, ultrasound-based shear wave elastography and MR elastography, were used. They should never be perceived as competitors as they are indeed at two different healthcare levels (21) (Fig. 67). Shearwave elastography can and should be employed as a screening tool at a secondary level after physical examination and liver function tests (simple or composite scores). One of the many advantages over the frequently used transient elastography is that this method is already incorporated in commonly available ultrasound devices, which are routinely used in the evaluation of patients with chronic liver diseases. However, MR elastography is not as widely available, is more expensive and belongs to the tertiary level of healthcare. As such, MR elastography should further assess the screened and positive patients, as this complex method allows more detailed assessment the viscoelastic properties, which can potentially characterize liver fibrosis and inflammation (Fig. 68).

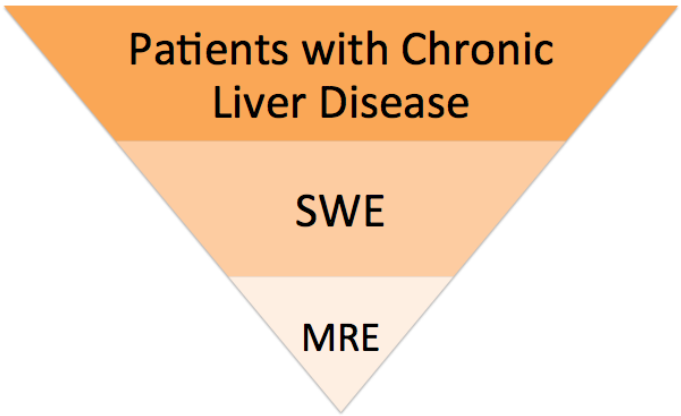

Figure 67. Levels of care for elastography-based methods in chronic liver diseases.

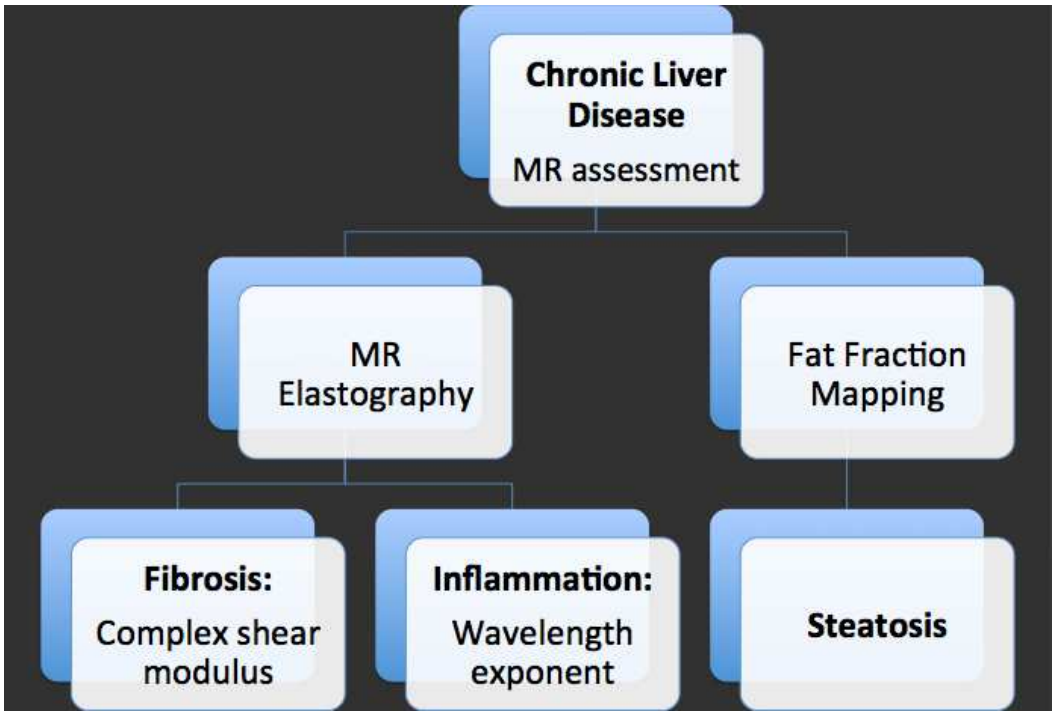

Figure 68. MR biomarkers for the assessment of chronic liver disease as proposed by this project.

Molecular imaging is at the moment relegated to the basic experimental assessment of chronic liver diseases, for safety and economical reasons. Even though the MR contrast agent studied in this project, as opposed to other vectorized probes, has already entered phase II proof-of-concept clinical trials in patients with thombo-embolic disease, the FDA (Food and Drug Administration) has asked for additional patient safety monitoring. The long pipeline development time, the lack of financial support and the critical concern about safety issues, place these probes far away from the clinical setting.

In conclusion, the need for noninvasive biomarkers in liver fibrosis, inflammation and steatosis to detect, stage and follow-up chronic liver disease is clear. Additional areas of research are nonetheless still lacking such as head-to-head comparisons of several noninvasive methods, defining cut-offs values for specific diseases, standardisation and repeatability and reproducibility assessments. Moreover, longitudinal studies to look at disease progression, regression under treatment and final outcomes are needed.

Truthfully, I think that the ideal biomarker will probably be a composite biomarker. The road ahead seems long, very long… as the "… man in the dark room, looking for the black cat…" that could be hiding!

References

1. Younossi ZM, Stepanova M, Afendy M et al. Changes in the prevalence of the most common causes of chronic liver diseases in the United States from 1988 to 2008. Clin Gastroenterol Hepatol 2011;9(6):524-530

2. Blachier M, Leleu H, Peck-Radosavljevic M, Valla D-C, Roudot-Thoraval F. The burden of liver disease in Europe: A review of available epidemiological data. J Hepatology 2013;58(3):593–608

3. Chalasani N, Younossi Z, Lavine JE et al. The diagnosis and management of non-alcoholic fatty liver disease: practice guideline by the american association for the study of liver diseases, american college of gastroenterology, and the american gastroenterological association. Hepatology 2012;55(6):2005-2023

4. Brunt EM, Tiniakos DG. Histopathology of nonalcoholic fatty liver disease. World J Gastroenterol 2010;16(42):5286-5296

5. Kuntz E, Kuntz E-D, History of hepatology, Kuntz E, Kuntz E-D, In: Hepatology textebook and atlas, 3rd edn, Heidelberg, Springer, 2008, 1-33.

6. Collins D. Mapping the Entrails: The Practice of Greek Hepatoscopy. Am J Philol 2008;129(3):319-345

7. Rutkauskas S, Gedrimas V, Pundzius J, Barauskas G, Basevičius A. Clinical and anatomical basis for the classification of the structural parts of liver. Medicina 2006; 42(2):98-106

8. Skandalakis JE, Skandalakis LJ, Skandalakis PN, Mirilas P. Hepatic surgical anatomy. Surg Clin N Am 2004;84(2)413–435

9. Catalano OA, Singh AH, Uppot, RN, Hahn PF, Cristina R. Ferrone CR, Sahani DV. Vascular and Biliary Variants in the Liver: Implications for Liver Surgery. Radiographics

2008;28(2):359-358.

10. Sauvanet A, Belghiti J, Anatomie du foie, Vilgrain V, Régent D, In: Imagerie de l'abdomen, 2nd edn, Paris, Lavoisier, 2010, 3-11

11. Meyers MA, Patterns of spread of disease from the liver, Mayers MA, Charnsangavej C, Oliphant M, In: Meyers' Dynamic Radiology of the Abdomen, 6th edn, New York, Springer, 2005, 223-241

12. Harisinghani MG, Abdominal lymph nodes anatomy, Harisinghani MG, In: Atlas of lymph node anatomy, 1st edn, New York, springer, 2013, 59-88

13. Zappa M, Sibert A, Vilgrain V, Liver and biliary system: postoperative findings, Reiser MF, Hricak H, Knauth M, In: Multislice-CT of the Abdomen, 1st edn, Heidelberg, Springer, 2012, 101-114

14. Soyer P. Segmental anatomy of the liver: utility of a nomenclature accepted worldwide. AJR 1993;161(3):572-573

15.Dodd GD. An American´s guide to Couinaud´s numbering system. AJR 1993;161 (3):574-575.

16. Wheater PR, Burkitt HG, Daniels VG, Liver and pancreas, Wheater PR, Burkitt HG, Daniels VG, In: Wheater's functional histology, 4th edn, Hong Kong, Churchill Livinstone, 1993, 271-281

17. Coppell JA, Brown SA, Perry DJ. Veno-occlusive disease: cytokines, genetics, and haemostasis. Blood Reviews 2003;17(2):63-70

18. Lok ASF, McMahon BJ. Chronic Hepatitis B: Update 2009. Hepatology 2009; 50(3):1-36

19. Ghany MG, Strader DB, Thomas DL, Seeff LB. Diagnosis, management, and treatment of hepatitis C: an update. Hepatology 2009;49(4):1335-1374

20. Kalb B and Martin DR. Magnetic resonance imaging of the liver part IIIB: diffuse liver

diseases. CDR 2008;31(13):1-6

21. Castera L, Pinzani M. Biopsy and non-invasive methods for the diagnosis of liver fibrosis: does it take two to tango? Gut 2010;59(7):861-866

22. Kim MJ, Cho MY, Baik SK et al. Histological subclassification of cirrhosis using the Laennec fibrosis scoring system correlates with clinical stage and grade of portal hypertension. J Hepatol 2011;55(5):1004-1009

23. Castera L. Noninvasive methods to assess liver disease in patients with hepatitis B or C. Gastroenterology 2012;142(6):1293-1302

24. Cohen JC. Human fatty liver disease: old questions and new insights. Science 2011;332(6037):1519-1523

25. Guiu B, Loffroy R, Ben Salem D et al. Liver steatosis and in-phase/opposed-phase MR imaging: theory and clinical applications at 3 T. J Radiol 2007;88(12):1845-1853

26. Tandra S, Yeh MM, Brunt EM. Presence and significance of microvesicular steatosis in nonalcoholic fatty liver disease. J Hepatol 2011;55(3):654-659

27.Tiniakos DG. Nonalcoholic fatty liver disease/nonalcoholic steatohepatitis: histological diagnostic criteria and scoring systems. Eur J Gastroenterol Hepatol 2010;22(6):643-650

28. Brunt EM. Nonalcoholic fatty liver disease: what the pathologist can tell the clinician. Dig Dis 2012;30(suppl 1):61-68

29. Angulo P. Nonalcoholic fatty liver disease. N Engl J Med 2002;346(16):1221-1231

30. Lewis JR, Mohanty SR. Nonalcoholic fatty liver disease: A review and update. Dig Dis Sci 2010;55:560-578

31. Fiuza M, Cortez-Dias N, Martins S, Belo A. Síndrome metabólica em Portugal: prevalência e implicações no risco cardiovascular - resultados do estudo VALSIM. Rev Port Cardiol 2008; 27(12):1495-1529

32. Williams CD, Stengel J, Asike MI. Prevalence of nonalcoholic fatty liver disease and

nonalcoholic steatohepatitis among a largely middle-aged population utilizing ultrasound and liver biopsy: a prospective study. Gastroenterology 2011;140(1):124–131

33. Dowman JK, Tomlinsonà JW, Newsome PN. Systematic review: the diagnosis and staging of non-alcoholic fatty liver disease and non-alcoholic steatohepatitis. Aliment Pharmacol Ther 2011;33(5): 525-540

34. David K, Kowdley KV, Unalp A, Kanwal F, Brunt EM, Schwimmer JB et al. Quality of life in adults with nonalcoholic fatty liver disease: baseline data from the nonalcoholic steatohepatitis clinical research network. Hepatology 2009;49(6):1904-1911

35. Castera L. Non-invasive diagnosis of steatosis and fibrosis. Diabetes & Metabolism 2008;34(6 Pt 2):674-679

36. Kleiner DE, Brunt EM, Van Natta M et al. Design and validation of a histological scoring system for nonalcoholic fatty liver disease. Hepatology 2005;41(6):1313-1321

37. Sebastiani G, Alberti A. How far is noninvasive assessment of liver fibrosis from replacing liver biopsy in hepatitis C? Journal of Viral Hepatitis 2012;19(Suppl. 1):18-36.

38. Baršić N, Lerotić I, Smirčić-Duvnjak L, Tomašić V, Duvnjak M. Overview and developments in noninvasive diagnosis of nonalcoholic fatty liver disease. World J Gastroenterol 2012;18(30):3945-3954

39. Middleton WD, Kurtz AB, Hertzberg BS, Practical physics, Middleton WD, Kurtz AB, Hertzberg BS, In: Ultrasound, 2nd edn, Saint Louis, Mosby, 2004, 3-27

40. Hamer OW, Aguirre DA, Casola G, Lavine JE, Woenckhaus M, Sirlin CB. Fatty liver: imaging patterns and pitfalls. Radiographics 2006;26(6):1637-1653

41. Iijima H, Moriyasu F, Tsuchiya K et al. Decrease in accumulation of ultrasound contrast microbubbles in non-alcoholic steatohepatitis. Hepatology Research 2007; 37(9):722-730

42. Orlacchio A, Bolacchi F, Petrella MC. Liver contrast enhanced ultrasound perfusion

imaging in the evaluation of chronic hepatitis c fibrosis: preliminary results.Ultrasoun in Med and Biol 2011;37(1):1-6

43. Sandrin L, Oudry J, Bastard C, Fournier C, Miette V, Mueller S, Non-invasive assessment of liver fibrosis by vibration-controlled transient elastography (FibroScan®), Takahashi H, In: Liver biopsy, 1st edn, InTech, 2011, 293-314

44. Schmeltzer PA, Talwalkar JA. Noninvasive tools to assess hepatic fibrosis: ready for prime time? Gastroenterol Clin N Am 2011;40(3):507-521

45. de Lédinghen V, Vergniol J. Transient elastography (FibroScan). Gastrœntérol Clin Bio 2008;32(Suppl 1):58-67

46. Clark PJ, Patel K. Noninvasive tools to assess liver disease. Curr Opin Gastroenterol 2011;27(3):210-216

47. Sagir A, Erhardt A, Schmitt M, Häussinger D. Transient elastography is unreliable for detection of cirrhosis in patients with acute liver damage. Hepatology 2008;47(2):592-595

48.Cobbolt JFL, Taylor-Robinson SD. Transient elastography in acute hepatitis: all that´s stiff is not fibrosis. Hepatology 2008;47(2):370-372

49. Cournane S, Browne JE, Fagan AJ. The effects of fatty deposits on the accuracy of the Fibroscan® liver transient elastography ultrasound system. Phys Med Biol 2012;57(12):3901-3914

50. Cobbold JFL, Patel D, Taylor-Robinson SD. Assessment of inflammation and fibrosis in non-alcoholic fatty liver disease by imaging-based techniques. Journal of Gastroenterology and Hepatology 2012;27(8):1281–1292

51. Friedrich-Rust M, Wunder K, Kriener S et al. Liver fibrosis in viral hepatitis: noninvasive assessment with acoustic radiation force impulse imaging versus transient elastography. Radiology 2009;252(2):595-604

52. Rizzo L, Calvaruso V, Cacopardo B et al. Comparison of transient elastography and

acoustic radiation force impulse for non-invasive staging of liver fibrosis in patients with chronic hepatitis C. Am J Gastroenterol 2011;106(12):2112-2120

53. Sirlin CB. Non invasive imaging biomarkers for steatosis assessment. Liver Transpl 2009;15(11):1389-1391

54. Ma X, Holalkere SN, Kambadakone RA, Mino-Kenudson M, Hahn PF, Sahani DV. Imaging-based quantification of hepatic fat: methods and clinical applications. Radiographics 2009;29(5):1253-1280

55. Shigefuku R, Takahashi H, Kobayashi M et al. Pathophysiological analysis of nonalcoholic fatty liver disease by evaluation of fatty liver changes and blood flow using xenon computed tomography: can early-stage nonalcoholic steatohepatitis be distinguished from simple steatosis? J Gastroenterol 2012;47(11):1238-47

56. Ronot M, Asselah T, Paradis V et al. Liver fibrosis in chronic hepatitis c virus infection: differentiating minimal from intermediate fibrosis with perfusion CT. Radiology 2010;256(1):135-142

57. Varenika V, Fu Y, Maher JJ et al. Hepatic fibrosis: evaluation with semiquantitative contrast-enhanced CT. Radiology 2013;266(1):151-158

58. Bavu E, Gennisson J-L, Couade M et al. Noninvasive in vivo liver fibrosis evaluation using supersonic shear imaging: a clinical study on 113 hepatitis C virus patients. Ultrasound Med Biol, 2011;37(9):1361–1373

59. Bercoff J, Tanter M, Fink M. Supersonic shear imaging: a new technique for soft tissue elasticity mapping. IEEE transactions on ultrasonics, ferroelectrics, and frequency control 2004;51(4):396-409

60. Ferraioli G, Tinelli C, Dal Bello B, Zicchetti M, Filice G, Filice C. Accuracy of real-time shear wave elastography for assessing liver fibrosis in chronic hepatitis C: a pilot study. Hepatology 2012; 56(6):2125-2133

61. Weishaupt D, Kochli VD, Marincek B. Factors affecting signal-to-noise ratio and basic pulse sequences. Weishaupt D, Kochli VD, Marincek B, In: How does MRI work?, 2nd edn, Heidelberg, Springer, 2006, 1-56

62. Wetbrook C, Image contrast and image production, Westbrook C, In: MRI at a glance, 1st edn, Malden, Blackwell Science, 2002, 20-61

63. Bitar R, Leung G, Perng R et al.MR Pulse sequences: what every radiologist wants to know but is afraid to ask. Radiographics 2006; 26(2):513–537

64. Goh V, Gourtsoyianni, Koh D-M. Functional imaging of the liver. Seminar Ultrasound CT MRI 2013;34(1):54-55

65. Reeder S, Sirlin CB. Quantification of Liver Fat with Magnetic Resonance Imaging. Magn Reson Imaging Clin N Am 2010;18(3):337–357

66. Qayyum A. MR spectroscopy of the liver: principles and clinical applications. Radiographics 2009;29(6):1653-1664

67. Szczepaniak LS, Nurenberg P, Leonard D et al. Magnetic resonance spectroscopy to measure hepatic triglyceride content: prevalence of hepatic steatosis in the general population. Am J Physiol Endocrinol Metab 2005;288(2):E462-E468

68. Hamilton G, Yokoo T, Bydder M et al. In vivo characterization of the liver fat ^{1}H MR spectrum. NMR Biomed. 2011; 24(7):784–790

69.Salibi N, Brown MA, Techniques for localized spectroscopy, Salibi N, Brown MA, In: Clinical MR spectroscopy first principles, 1st edn, New York, Wiley-Liss, 1998, 62-105

70. Hamilton G, Middleton MS, Bydder M. Effect of PRESS and STEAM sequences on magnetic resonance spectroscopic liver fat quantification. J Magn Reson Imaging 2009;30(1):145-152

71. Sirlin C. Invited commentary. Radiographics 2009;29(5):1277-1280

72. de Graaf RA, Spectroscopic imaging and multivolume localization, de Graaf RA, In: In

vivo NMR spectroscopy, 2nd edn, Chichester, Wiley, 2007, 349-384

73. Bittencourt LK, Matos C, Coutinho Jr AC. Diffusion-weighted magnetic resonance imaging in the upper abdomen: technical issues and clinical applications. Magn Reson Imaging Clin N Am 2011;19(1):111–131

74. de Figueiredo EHMSG, Borgonovi AFNG, Doring TM. Basic concepts of MR imaging, diffusion MR imaging, and diffusion tensor imaging. Magn Reson Imaging Clin N Am 2011;19(1)1-22

75. Padhani AR, Liu G, Mu-Koh D et al. Diffusion-weighted magnetic resonance imaging as a cancer biomarker: consensus and recommendations. Neoplasia 2009;11(2):102-125

76. Van Beers BE, Doblas S, Sinkus R. New acquisition techniques: fields of application. Abdom Imaging 2012; 37(2):155–163

77. Koh D-M, Collins DJ, Orton MR. Intravoxel incoherent motion in body diffusion-weighted MRI: reality and challenges. AJR 2011;196(6):1351–1361

78. Guiu B, Cercueil J-P. Liver diffusion-weighted MR imaging: the tower of Babel? Eur Radiol 2011;21(3):463-467

79. Koinuma M, Ohashi I, Hanafusa K, Shibuya H. Apparent diffusion coefficient measurements with diffusion-weighted magnetic resonance imaging for evaluation of hepatic fibrosis. JMRI 2005;22(1):80-85

80. Taouli B, □ Tolia AJ, Losada M et al. Diffusion-weighted MRI for quantification of liver fibrosis: preliminary experience. AJR 2007;189(4):799–806

81. Taouli B, Chouli M, Martin AJ, Qayyum A, Coakley FV, Vilgrain V. Chronic hepatitis: role of diffusion-weighted imaging and diffusion tensor imaging for the diagnosis of liver fibrosis and inflammation. J Magn Reson Imaging 2008;28(1):89-95

82. Luciani A, Vignaud A, Cavet M et al. Liver cirrhosis: intravoxel incoherent motion MR imaging-pilot study. Radiology 2008;249(3):891-899

83. Patel J, Sigmund EE, Rusinek H, Oei M, Babb JS, Taouli B. Diagnosis of cirrhosis with intravoxel incoherent motion diffusion MRI and dynamic contrast-enhanced MRI alone and in combination: preliminary experience. J Magn Reson Imaging 2010;31(3):589-600

84. Do RKG, Chandanara H, Felke E et al. Diagnosis of liver fibrosis and cirrhosis with diffusion- weighted imaging: value of normalized apparent diffusion coefficient using the spleen as reference organ. AJR 2010;195(3):671–676

85. Bonekamp S, Torbenson MS, Kamel IR. Diffusion-weighted magnetic resonance imaging for the staging of liver fibrosis. J Clin Gastroenterol 2011;45(10):885-892

86. Bakan AA, Inci EE, Bakan S , Gokturk S, Cimilli T. Utility of diffusion-weighted imaging in the evaluation of liver fibrosis. Eur Radiol 2012; 22(3):682-687

87. Annet L, Peeters F, Abarca-Quinones J, Leclercq I, Moulin P, Van Beers BE. Assessment of diffusion-weighted MR imaging in liver fibrosis. J Magn Reson Imaging 2007;25(1):122-128

88. Godfrey EM, Mannelli L, Griffin N, Lomas DJ. Magnetic resonance elastography in the diagnosis of hepatic fibrosis. Semin Ultrasound CT MRI 2013;34(1):81-88

89. Huwart L, Van Beers BE. MR elastography. Gastroenterol Clin Biol 2008;32(6 Suppl 1):68-72

90. Garteiser P, Doblas S, Daire J-L. MR elastography of liver tumours: value of viscoelastic properties for tumour characterization. Eur Radiol 2012;22(10):2169-2177

91. Nguyen D, Talwalkar JA. Noninvasive assessment of liver fibrosis. Hepatology 2011;53(6):2107-2110

92. Wells RJ. Tissue mechanics and fibrosis. Biochim Biophys Acta 2013. DOI: 10.1016/j.bbadis

93. Motosugi U, Ichikawa T, Amemiya F. Cross-validation of MR elastography and

ultrasound transient elastography in liver stiffness measurement: discrepancy in the results of cirrhotic liver. J Magn Reson Imaging 2012;35(3):607-610

94. Sinkus R, Siegmann K, Xydeas T, Tanter M, Claussen C, Fink M. MR elastography of breast lesions: understanding the solid/liquid duality can improve the specificity of contrast-enhanced MR mammography. Magn Reson Med 2007;58(6):1135-1144

95. Huwart L, Sempoux C, Vicaut E et al. Magnetic resonance elastography for the noninvasive staging of fibrosis. Gastroenterology 2008;135(1):32-40

96. Yin M, Talwalker JA, Glaser KJ et al. A preliminary assessment of hepatic fibrosis with magnetic resonance elastography. Clin Gastroenetrol Hepatol 2007;5(10):1207-1213.e.2

97. Wang Y, Ganger DR, Levitsky LA et al. Assessment of chronic hepatitis and fibrosis: comparison of MR elastography and diffusion-weighted imaging. AJR 2011;196(3):553-561

98. Asbach P, Klatt D, Schlosser B et al. Viscoelasticity-based staging of hepatic fibrosis with multifrequency MR elastography. Radiology 2010;257(1):80-86

99.Taouli B, Ehman RL, Reeder SB. Advanced MRI methods for assessment of chronic liver disease. AJR 2009;193(1):14–27

100. Motosugi U, Ichikawa T, Sano K et al. Effects of gadoxeticacid on liver elasticity measurement by using magnetic resonance elastography. Magn Reson Imaging 2012;30(1):128–132

101. Garteiser P, Sahebjavaher RS, Ter Beek L et al. Rapid acquisition of multifrequency, multislice and multidirectional magnetic resonance elastography data with a fractionally encoded gradient echo sequence. NMR in Biomedicine 2013. DOI: 10.1002/nmb.2958

102. Chen J, Talwalkar JA, Yin M, Glaser KJ, Sanderson SO, Ehman RL. Early detection of nonalcoholic steatohepatitis in patients with nonalcoholic fatty liver disease by using

MR elastography. Radiology 2011;259(3):749-756

103. Salameh N, Larrat B, Abarca-Quinones J et al. Early detection of steatohepatitis in fatty rat liver by using MR elastography. Radiology 2009;253(1):90-97

104. Van Beers BE, Pastor CM, Hussain HK. Primovist, Eovist: what to expect? J Hepatol 2012;57(2):421-429

105. Motosugia U, Ichikawaa T, Oguri M et al. Staging liver fibrosis by using liver-enhancement ratio of gadoxetic acid-enhanced MR imaging: comparison with aspartate aminotransferase-to-platelet ratio index. Magn Reson Imaging 2011;29(8):1047-1052

106. Katsube T, Okada M, Kumano S. Estimation of liver function using T1 mapping on Gd-EOB-DTPA- enhanced magnetic resonance imaging. Invest Radiol 2011;46(4):277-283

107. Chen B-B, Hsu C-Y, Yu C-W et al Dynamic contrast-enhanced magnetic resonance imaging with Gd-EOB-DTPA for the evaluation of liver□fibrosis in chronic hepatitis patients. Eur Radiol 2012;22(1):171-80

108. Pais R, Pascale A, Fedchuck L, Charlotte F, Poynard T, Ratziu V. Progression from isolated steatosis to steatohepatitis and fibrosis in nonalcoholic fatty liver disease. Clin Res Hepatol Gastroenterol 2011;35(1):23-28

109. Won V, Wong G, Choi P et al. Disease progression of non-alcoholic fatty liver disease: a prospective study with paired liver biopsies at 3 years. Gut 2010;59(7):969-974.

110. Kim SR, NakajimaT, Ando K, Mita K, Fukuda K. Two cases of nonalcoholic liver steato-hepatitis developing from simple fatty liver. J Gstrointestin Liver Dis 2009;18(4):491-495.

111. Harrisson SA, Togerson S, Hayashi PH. The natural history of non alcoholic fatty liver disease: a clinical histopathological study. Am J Gastroenteol 2003;98(9):2042-2047.

112. Yokoo T, Bydder M, Hamilton G et al. Nonalcoholic fatty liver disease: diagnostic

and fat-grading accuracy of low-flip-angle multiecho gradient-recalled-echo MR imaging at 1.5 T. Radiology 2009;251(1):67-76.

113. Yokoo T, Shiehmorteza M, Hamilton G et al. Estimation of hepatic proton-density fat fraction by using MR imaging at 3.0 T. Radiology 2011;258(3):749-759.

114. Guiu B, Petit JM, Loffroy R et al. Quantification of liver fat content: comparison of triple-echo chemical shift gradient-echo imaging and in vivo proton MR spectroscopy. Radiology 2009;250(1):95-102

115. d'Assignies G, Ruel M, Khiat A et al. Noninvasive quantification of human liver steatosis using magnetic resonance methods. Eur Radiol 2009;19(8):2033-2040.

116. Reeder SB, Cruite I, Hamilton G, Sirlin CB. Quantitative assessment of liver fat with magnetic resonance imaging and spectroscopy. J Magn Reson Imaging 2011;34(4):729-749.

117. Guiu B, Loffroy R, Petit JM et al. Mapping of liver fat with triple-echo gradient echo imaging: validation against 3.0-T proton MR spectroscopy. Eur Radiol 2009;19(7):1786-1793.

118. Guiu B, Peti J-M, Capitan V et al. Intravoxel incoherent motion diffusion-weighted imaging in nonalcoholic fatty liver disease: a 3.0-T MR study. Radiology 2012;265(1):96-103.

119. Bland JM, Altman DG. Statistical methods for assessing agreement between two methods of clinical measurement. Lancet 1986;1(8476):307-310.

120. Décarie P-O, Lepanto L, Billiard J-S et al. Fatty liver deposition and sparing: a pictorial review. Insights Imaging 2011;2(5):533-538

121. Forbes GB. Splenic lipidosis after administration of intravenous fat emulsions. J Clin Pathol 1978;31(8):765-771

122. Stefan N, Kantartzis K, Häring H-U. Causes and metabolic consequences of fatty

liver. Endocr Rev 2008;29(7):939-960.

123. Roulot D, Costes JL, Buyck JF et al (2011) Transient elastography as a screening tool for liver fibrosis and cirrhosis in a community-based population aged over 45 years. Gut 60(7):977-984

124. Lewin M, Poujol-Robert A, Boelle P-Y et al. Diffusion-weighted magnetic resonance imaging for the assessment of fibrosis in chronic hepatitis C. Hepatology 2007;46(3):658-665

125. Lee JT, Liau J, Murphy P, Schroeder ME, Sirlin CB, Bydder M. Cross-sectional investigation of correlation between hepatic steatosis and IVIM perfusion on MR imaging. Magn Reson Imaging 2012;30(4):572-578

126. Anderson SW, Soto JA, Milch HN et al. Effect of diffusion progression on liver apparent diffusion coefficient values in a murine model of NASH at 11.7 Tesla MRI. J Magn Reson Imaging 2011;33(4):882-888

127. Poyraz AK, Onur MR, Kocakoç E, Ogur E. Diffusion-weighted MRI of fatty liver. J Magn Reson Imaging 2012;35(5):1108-1111

128. Gimsberg HN, Goldberg IJ. Disorders of the lipoprotein metabolism. In: Braunvald E, Fauci AS, Kasper DL, Hauser SL, Longo DL, Jameson JL (eds) Disorders of the intermediary metabolism. (Harrison's principals of internal medicine), 15th edn. Mc Graw-Hill, USA, 2001, p 2246

129. Crawford JM, Basic mechanisms in hepatopathology. In: Burt AD, Portmann BC, Ferrell LD (eds) MacSween's pathology of the liver, 5th edn, Churchill Livingstone Elsevier, Philadelphia, Philadelphia, 2007, p 85

130. Le Bihan D, Breton E, Lallemand D, Aubin M-L, Vignaud J, Laval-Jeantet M. Separation of diffusion and perfusion in intravoxel incoherent motion MR imaging. Radiology 1988;168(2):497-505

131. Kim SY, Lee SS, Byun JH et al. Malignant hepatic tumors: short-term reproducibility of apparent diffusion coefficients with breath-hold and respiratory-triggered diffusion-weighted MR imaging. Radiology 2010;255(3):815-23

132. Ababneh ZQ, Beloeil H, Berde CB, Ababneh AM, Maier SE, Mulkern RV. In vivo lipid diffusion coefficient measurements in rat bone marrow. Magn Reson Imaging 2009;27(6):859-864

133. Qiao Y, Ronen I, Viereck J, Ruberg FL, Hamilton JA. Identification of atherosclerotic lipid deposits by diffusion-weighted imaging. Arterioscler Thromb Vasc Biol 2007;27(6):1440–1446

134. Wenkel E, Geppert C, Schulz-Wendtland R et al. Diffusion weighted imaging in breast MRI: comparison of two different pulse sequences. Acad Radiol 2007;14(9):1077-1083

135. Baron P, Dorrius MD, Kappert P, Oudkerk M, Sijens PE. Diffusion-weighted imaging of normal fibroglandular breast tissue: influence of microperfusion and fat suppression technique on the apparent diffusion coefficient. NMR Biomed 2010;23(4):399-405

136. DP, Callaghan MF, Wylezinska-Arridge M, Fitzpatrick J, Naoumova RP, Hajnal JV et al. Liver fat content and T2*: simultaneous measurements by using breath-hold multiecho MR imaging at 3.0 T – feasibility. Radiology 2008;247(2):550-557

137. Hussain HK, Chenevert TL, Londy FJ, Gulani V, Swanson SD, McKenna BJ et al. Hepatic fat fraction: MR imaging for quantitative measurement and display – early experience. Radiology 2005;237(3):1048-1055

138. Marsman H, Matsushita T, Dierkhising R, Kremers W, Rosen C, Burgart L. Assessment of donor liver steatosis: pathologist or automated software. Hum Pathol 2004;35(4):430-435

139. Farrell GC, Teoh NC, McCuskey RS. Hepatic microcirculation in fatty liver disease.

Anat Rec 2008;291(6):684-692

140. King MD, van Bruggen N, Busza AL, Houseman J, Williams SR, Gadian DG. Perfusion and diffusion MR imaging. Magn Reson Med 1992;24(2):288-301

141. McCuskey RS, Ito Y, Robertson GR, McCuskey MK, Perry M, Farrell GC. Hepatic microvascular dysfunction during evolution of dietary steatohepatitis in mice. Hepatology 2004;40(2):386-393

142. Annet L, Materne R, Danse E, Jamart J, Horsmans Y, Van Beers BE. Hepatic flow parameters measured with MR imaging and Doppler US: correlations with degree of cirrhosis and portal hypertension. Radiology 2003;229(2):409-414

143. Paradis V, Bedossa P. Definition and natural history of metabolic steatosis: histology and cellular aspects. Diabetes Metab 2008;34(6):638-642

144. Ratziu V, Cadranel J-F, Serfaty L et al. A survey of patterns of practice and perception of NAFLD in a large sample of practicing gastroenterologists in France. J Hepatol 2012;57(2);376-383

145. Poynard T, Lenaour G, Vaillant JC et al. Liver biopsy analysis has a low level of performance for diagnosis of intermediate stages of fibrosis. Clin Gastroenterol Hepatol 2012;10(6):657-663

146. Leitão HS, Doblas S, d'Assignies G et al. Fat deposition decreases diffusion parameters at MRI: a study in phantoms and patients with liver steatosis. Eur Radiol 2013;23(2):461-467

147. Guiu B, Petit J-M, Capitan V et al. Intravoxel incoherent motion diffusion-weighted imaging in nonalcoholic fatty liver disease: a 3.0-T MR study. Radiology 2012;265(1):96-103

148. Bülow R, Mensel B, Meffert P, Hernando D, Evert M, Kühn J-P. Diffusion-weighted magnetic resonance imaging for staging liver fibrosis is less reliable in the presence of fat

and iron. Eur Radiol 2013 ; 23(5) :1281-1287

149. Wang J, Liu J-J, Liang Y-Y et al. Could diffusion-weighted imaging detect injured bile ducts of ischemic-type biliary lesions after orthotopic liver transplantation? AJR 2012;199(4):901-906

150. Bedossa P, Poynard T. An algorithm for the grading of activity in chronic hepatitis C. The METAVIR Cooperative Study Group. Hepatology 1996;24(2):289–293

151. Brunt EM. Pathology of fatty liver disease. Modern Pathology 2007;20(1s):S40-S48

152. Wagner M, Doblas S, Daire J-L et al. Diffusion-weighted imaging for the regional characterization of liver tumors. Radiology 2012;264(2):464-472

153. Sinkus R, Tanter M, Xydeas T, Catheline S, Bercoff J, Fink M. Viscoelastic shear properties of in vivo breast lesions measured by MR elastography. Magn Reson Imaging 2005;23(2):159-165

154. Sinkus R, Lorenzen J, Schrader D, Lorenzen M, Dargatz M, Holz D. High-resolution tensor MR elastography for breast tumour detection. Phys Med Biol 2000;45(6):1649-1664

155. Huwart L, Peeters F, Sinkus R et al. Liver fibrosis: non-invasive assessment with MR elastography. NMR Biomed 2006;19(2):173-179

156. Sinkus R, Tanter M, Catheline S et al. Imaging anisotropic and viscous properties of breast tissue by magnetic resonance-elastography. Magn Reson Med 2005;53(2):372-387

157. Garteiser P, Doblas S, Van Beers BE, Vilgrain V, Sinkus R. Physical boundary conditions reconstruction: a novel method to determine viscoelastic parameters from magnetic resonance elastography data. Proceedings of the International Society for Magnetic Resonance in Medicine 2011; Communication 2825

158. Zou KH, Tuncali K, Silverman SG. Correlation and simple linear regression. Radiology 2003;227(3):617-628

159. Gareen IF, Gatsonis C. Primer on multiple regression models for diagnostic imaging

research. Radiology 2003;229(2):305-310

160. Ziol M, Kettaneh A, Christidis C et al. Noninvasive assessment of liver fibrosis by measurement of stiffness in patients with chronic hepatitis C. Hepatology 2005;41(1):48-54

161. Castera L, Vergniol J, Foucher J et al. Prospective comparison of transient elastography, fibrotest, APRI, and liver biopsy for the assessment of fibrosis in chronic hepatitis C. Gastroenterol 2005;128(2):343-350

162. Arena U, Vizzutti F, Corti G et al. Acute viral hepatitis increases liver stifness values measured by transient elastography. Hepatology 2008;47(2):380-384

163. Coco B, Oliveri F, Maina AM et al. Transient elastography: a new surrogate marker of liver fibrosis influenced by major changes of transaminases. J Viral Hepat 2007;14(5):360-369

164. Fraquelli M, Rigamonti C, Casazza G et al. Etiology-related determinants of liver stiffness values in chronic viral hepatitis B or C. J Hepatol 2011;54(4):621-628

165. Kim D, Kim R, Talwalkar JA, Kim HJ, Ehman RL. Advanced fibrosis in nonalcoholic fatty liver disease: noninvasive assessment with MR elastography. Radiology 2013. DOI: 10.1148/radiol.13121193

166. Yoshioka K, Kawabe N, Hashimoto S. Transient elastography: applications and limitations. Hepatol Res 208;38(11):1063-1068

167. Wong VWS, Vergniol J, Wong GLH et al. Diagnosis of fibrosis and cirrhosis using liver stiffness measurement in nonalcoholic fatty liver disease. Hepatology 2010; 51(2):454-462

168. Gaia S, Carenzi S, Barilli AL et al. Reliability of transient elastography for the detection of fibrosis in non-alcoholic fatty liver disease and chronic viral hepatitis. J Hepatol 2011;54(1):64-71

169. Neubauer K, Knittel T, Armbrust T, Ramadori G. Accumulation and Cellular Localization of Fibrinogen/Fibrin During Short-term and Long-term Rat Liver Injury. Gastroenterology1995;108(4):1124-1135

170. Lisman T, Caldwell SH, Burroughs AK et al. Hemostasis and thrombosis in patients with liver disease: The ups and downs. J Hepatol 2010;53(2):362–371

171. Tripodi A. The long-awaited whole-blood thrombin generation test. Clin Chem 2012;58(8):1173-1175.

172. Tripodi A, Salerno F, Chantarangkul V, Clerici M, Cazzaniga M, Primignani M et al. Evidence of normal thrombin generation in cirrhosis despite abnormal conventional coagulation tests. Hepatology 2005;41(3):553-558.

173. MacPhee PJ, Dindzans VJ, Fung LS, Levy GA. Acute and chronic changes in the microcirculation of the liver in inbred strains of mice following infection with mouse hepatitis virus type 3. Hepatology 1985;5(4):649-660.

174. Ansteea QM, Dharb A, Thurszb MR. The role of hypercoagulability in liver fibrogenesis. Clin Res Hepatol Gastroenterol 2011;35(8-9):526-533

175. Overoye-Chan K, Koerner S, Looby RJ et al. EP-2104R: A fibrin-specific gadolinium-based mri contrast agent for detection of thrombus. J Am Chem Soc 2008;130(18):6025–6039

176. Uppal R, Ay I, Dai G, Kim YR, Sorensen AG, Caravan P. Molecular MRI of intracranial thrombus in a rat ischemic stroke model. Stroke 2010;41(6):1271-1277

177. Spuentrup E, Fausten B, Kinzel S et al. Molecular magnetic resonance imaging of atrial clots in a swine model. Circulation 2005;112(3):396-399

178. Spuentrup E, Katoh M, Wiethoff AJ et al. Molecular magnetic resonance imaging of pulmonary emboli with a fibrin-specific contrast agent. Am J Respir Crit Care Med 2005;172(4):494–500

179. Spuentrup E, Buecker A, Katoh M et al. Molecular magnetic resonance imaging of coronary thrombosis and pulmonary emboli with a novel fibrin-targeted contrast agent. Circulation 2005;111(11):1377-1382

180. Vymazal J, Spuentrup E, Cardenas-Molina G et al. Thrombus imaging with fibrin-specific gadolinium-based mr contrast agent EP-2104R. Invest Radiol 2009;44(11):697-704

181. Imokawa S, Sato A, Hayakawa H, Kotani M, Urano T, Takada A. Tissue factor expression and fibrin deposition in the lungs of patients with idiopathic pulmonary fibrosis and systemic sclerosis. Am J Respir Crit Care Med 1997;156(2 Pt 1):631–636.

182. Mercer PF, Chambers RC. Coagulation and coagulation signalling in fibrosis. Biochem Biophys Acta 2013;1832(7):1018-1027

183. Huntrakoon M, Menon CD, Hung K-S. Diethylnitrosamine-induced pulmonary endocrine cell hyperplasia and its association with adenomatosis and adenocarcinoma in rabbits. Am J Pathol 1989;135(6):1119-28

184. Poynard T, Munteanu M, Luckina E et al. Liver fibrosis evaluation using real-time shear wave elastography: Applicability and diagnostic performance using methods without a gold standard. J Hepatol 2013;58(5):928-935

185. Ferraioli G, Tinellib C, Zicchetti M et al. Reproducibility of real-time shear wave elastography in the evaluation of liver elasticity. Eur J Radiol 2012;81(11):3102-3106

186. Wang Q-B, Zhu H, Liu H-L, Zhang B. Performance of magnetic resonance elastography and diffusion-weighted imaging for the staging of hepatic fibrosis: a meta-analysis. Hepatology 2012;56(1):239-247

187. Holm S, Sinkus R. A unifying fractional wave equation for compressional and shear waves. J Acoust Soc Am. 2010;127(1):542-559

188. Asbach P, Klatt D, Hamhaber U et al. Assessment of liver viscoelasticity using

multifrequency MR elastography. Magn Reson Med 2008;60(2):373–379

189. Shire NJ, Yin M, Chen J et al. Test–Retest Repeatability of MR elastography for noninvasive liver fibrosis assessment in hepatitis C. J Magn Reson Imaging 2011;34(4):947–955

190. Lee DH, Lee JM, Han JK, Choi BI. MR Elastography of healthy liver parenchyma: normal value and reliability of the liver stiffness value measurement. J Magn Reson Imaging 2012. DOI: 10.1002/jmri.23958

191. Leclerc GE, Charleux F, Robert L. Analysis of liver viscosity behavior as a function of multifrequency magnetic resonance elastography (MMRE) postprocessing. J Magn Reson Imaging 2013. DOI: 10.1002/jmri.23986

192. Beveridge WIB. The Art of Scientific Investigation. W. Heinemann, London, 1957, p 105.

193. Van Beers BE, Vilgrain V. Biomarkers in abdominal imaging. Abdom Imaging 2009;34(6):663-667

194. European Society of Radiology. ESR statement on the stepwise development of imaging biomarkers. Insights Imaging 2013;4(2):147-152

195. Behrns KE, Tsiotos GG, DeSouza NF, Krishna MK, Ludwig J, Nagorney DM. Hepatic steatosis as a potential risk factor for major hepatic resection. J Gastrointest Surg 1998; 2(3):292-298.

196. de Meijer VE, Kalish BT, Puder M, Ijzermans JN. Systematic review and meta-analysis of steatosis as a risk factor in major hepatic resection. Br J Surg 2010; 97(9):1331-1339.

197. Farges O, Malassagne B, Flejou JF, Balzan S, Sauvanet A, Belghiti J. Risk of major liver resection in patients with underlying chronic liver disease: a reappraisal. Ann Surg 1999; 229(2):210-215.

198. Gomez D, Malik HZ, Bonney GK et al. Steatosis predicts postoperative morbidity following hepatic resection for colorectal metastasis. Br J Surg 2007; 94(11):1395-1402.

199. Raptis DA, Fischer MA, Graf R, et al. MRI: the new reference standard in quantifying hepatic steatosis? Gut 2011;61(1):117-127.

ORIGINAL PUBLICATIONS

Six Honest Serving-Men *for Medical Writers*

I keep six honest serving men
They taught me all I knew
Their names are WHAT and WHY and WHEN
And HOW and WHERE and WHO

Rudyard Kipling